NTNU
Norwegian University of
Science and Technology

Resynthesis of Cathode Active Material from Electric Vehicle Battery Waste and Metal Quantification along the Route

Jose Paulino Peris Sastre

Master thesis.	Chemical Engineering
Submission date:	February 2021
Supervisor:	Dr. Sulalit Bandyopadhyay
Co-supervisor:	Dr. Seniz Ucar

Norwegian University of Science and Technology

Department of Chemical Engineering

Abstract

In recent years, the amount of spent lithium-ion batteries (LIBs) from electric vehicles (EVs) has grown dramatically due to the increase of production of EVs as an alternative to the traditional internal combustion engine vehicles. For this reason, it is necessary to develop a proper recycling process for spent LIBs. Recycling will contribute to the circular economy in EVs battery production and alleviate depletion of critical metals such as Ni and Li present in the battery cathodes.

The co-precipitation of the cathode active metals (CAM) Li, Ni, Co, and Mn after a leaching process of the electrodes, following a novel hydrometallurgical approach for recycling of spent LIBs from EVs was performed in this master thesis. A final calcination step was also conducted to convert the precipitated metal hydroxide into the metal oxide $LiNi_xCo_yMn_{(1-x-y)}O_2$ that forms the CAM. This is a well-studied technique in regenerating LIB cathode material due to the very similar properties of Ni, Co, and Mn. The challenge in recycling LIBs cathode material is the constant evolution and variety of the cathode composition and chemistry. Normally LIBs have a lifetime of 10 years and the CAM might be outdated according to the chemistry and composition by the time it is recycled. In most of the previous studies reported about this hydrometallurgical recycling route of the CAM, the cathode precursor is resynthesized with a Ni: Co: Mn molar ratio of 1: 1: 1. However, following the current and future development of the new cathode materials based on rich Ni stoichiometric ratios, recovering the highest Ni: Co: Mn molar ratio was aimed when co-precipitating the active metals in this project. The recycling of CAM according to future chemistry demands represents the novelty of the work with respect to the current state-of-the-art.

In the first stage of the hydrometallurgical recycling route, the leaching kinetics study showed that Ni, Co and Cu follow the diffusion controlled model at 80ºC. To achieve the goal of high Ni content in the resynthesized CAM, a multi-step precipitation to selectively separate Ni over Co and Mn using NaOH, and furthermore Li using Na_2CO_3, was studied. The selective precipitation of Ni is based on the solubility difference between the Ni, Co, and Mn hydroxides formed, which lead to different pH values of precipitation. The results demonstrated that 96% of Ni, 86% Co, and 28% of Mn could be precipitated from the leaching liquor. In the final calcination step, Ni-rich metal hydroxide was converted into the metal oxide, of which the CAM is composed. As a result, a $LiNi_{0.47}Co_{0.42}Mn_{0.11}O_2$ was resynthesized, achieving effective resource recycling from cathode scrap of spent LIBs.

Preface

This master thesis was performed on behalf of the Reactor Technology and Environmental Engineering group at the Department of Chemical Engineering, NTNU. The work has been carried out between September 1, 2020 and February 5, 2021.

First of all, I would like to thank my supervisor Dr. Sulalit Bandyopadhyay for his wise advice and support all throughout the project, which has been very long due to the Covid-19 situation. He always took time whenever it was necessary despite his very busy schedule. Furthermore, thanks a lot to my co-supervisor Seniz Ucar for her unconditional help.

Thanks to Stina, Neshat, and Tryanti for proofreading the report (Andreas as well, my Australian lad) and make the study room a much more enjoyable and funnier place. Finally, thanks to my buddy Zeeshan, we started working together almost two years ago, and although he changed the group, he has been always a great support (also a great source of filters and tobacco in times of emergency).

I hereby declare that this is an independent work according to the exam regulations of the Norwegian University of Science and Technology.

Trondheim, 05.02.2021

Jose Paulino Peris Sastre

Contents

Abstract i

Preface iii

Contents v

List of Figures viii

List of Tables xi

Overview of the Report xiii

1 Introduction 1

1.1 Lithium-Ion Batteries (LIBs) 1

1.1.1 Introduction into LIBs Recycling Processes 3

1.2 Motivation and Goals 5

2 Theory and Background 8

2.1 Leaching 8

2.1.1 Kinetic Models 11

2.2 Precipitation 13

2.2.1 Thermodynamic Properties 14

3 Literature Review 18

3.1 LIBs Recycling Process 18

3.1.1 Leaching of Cathode Active Metals from Spent LIBs 22

3.1.2 Co-precipitation of Cathode Active Metals from Leachate 24

3.1.3 Resynthesis of Cathode Active Metal Oxides 27

4 Experimental Procedure 28

4.1 Materials 28

4.1.1 Chemical Reagents 28

4.1.2 Experimental Set-up 29

4.1.3 Characterization Techniques 31

4.2 Methodology 37

4.2.1 Leaching Kinetic Studies 37
4.2.2 MP-AES Validation Method 39
4.2.3 Selective Multi-Step Precipitation and Co-precipitation 43
4.2.4 Microwave Digestion of Solid Samples 46
4.2.5 Calcination of Precipitates 48
5 Results and Discussion 50
5.1 Initial Electrode Material Composition 50
5.2 Leaching Kinetic Studies 51
5.3 MP-AES Validation Method 57
5.4 Selective Multi-Step Precipitation of Leachates 61
5.4.1 Al and Cu Removal 62
5.4.2 Precipitation of Hydroxides with High Ni Content 67
5.4.3 Precipitation of Lithium Carbonate 72
5.4.4 Overall Precipitation Recycling Route 75
5.5 Calcination of Metal Precipitates 77
6 Conclusions 81
7 Future Work 83
8 Bibliography 84
Appendix I

List of Figures

Figure 1.1: Battery (BEV), Plug-in Hybrid (PHEV), Hybrid (HEV), Mild-Hybrid (48V), Micro-Hybrid (12V) Electric Vehicles and ICE vehicles sales (No electrification) by 2030 [5]. 2

Figure 1.2: Charge and discharge process of a Lithium-ion battery [8]. 3

Figure 1.3: EV battery life-cycle [10]. 4

Figure 2.1: E-pH diagram for Co-H_2O system at 298 K [soluble species (except H^+) = 0.5 M at 298 K] [19]. 10

Figure 2.2: E-pH diagram for Mn-H2O system at 298 K [soluble species (except H^+) = 0.5 M at 298 K] [19]. 10

Figure 2.3: Mechanisms of leaching in the shrinking core model [23]. 12

Figure 2.4: Stable, metastable, and labile zones of a specific element in a concentration vs. temperature plot [26]. 14

Figure 3.1: LithoRec process of battery recycling [12]. 19

Figure 3.2: Arrhenius plots for leaching of Co, Mn, Ni, and Li from the cathode scrap under the surface chemical controlled model [37]. 24

Figure 3.3: Metal precipitation using NaOH at 40ºC from H_2SO_4 leaching solution [40]. 25

Figure 3.4: Metal precipitation using Na_2S at 40ºC from H_2SO_4 leaching solution [40]. 26

Figure 4.1: Leaching set-up. 29

Figure 4.2: Beaker precipitation set-up. 30

Figure 4.3: Closed jacked reactor precipitation set-up. 30

Figure 4.4: Vacuum precipitation set-up. 31

Figure 4.5: UV-VIS Shimadzu UV 2401PC Spectrophotometer. 32

Figure 4.6: Three main interactions of X-rays with matter [52]. 33

Figure 4.7: XRF Rigaku Supermini200. 34

Figure 4.8: Agilent MP-AES 4210. 35

Figure 4.9: X-ray source and diffracted from sample in XRD analysis. 36

Figure 4.10: XRD Bruker D8 A25 DaVinci. 36

Figure 4.11: High temperature furnace Nabertherm HTC 03/14 used for calcination of precipitates [53]. 37

Figure 4.12: Schematic preparation of a synthetic solution of 5 mg/L Ni, 5 mg/L Co, 20 mg/L Cu, and 30 mg/L Mn. 42

Figure 4.13: Multi-step precipitation process flow diagram. 44

Figure 4.14: Microwave digestor Speedwave. 47

Figure 4.15: Precipitate 3 (pH = 7.7) a) before digestion, and b) dissolved after digestion. .. 48

Figure 5.1: Composition of the different initial electrode powder used for leaching kinetic studies analysed with XRF. 50

Figure 5.2: Filtered leachate samples at 1.5, 2.5, 5, 7.5, 10, 15, 20, 30, 50, and 60 minutes of reaction time from kinetic experiment. 51

Figure 5.3: UV-Vis absorbances as a function of reaction time for the wavelengths 392 nm (Ni), 512 nm (Co), and 755 nm (Cu) for all six leaching experiments with prismatic pyrolyzed (Pyro), non-pyrolyzed (Non-Pyro), and leaf cells. 52

Figure 5.4: Plot of $1-(1-X)^{1/3}$ and $1-3(1-X)^{2/3}+2(1-X)$ versus time at 80ºC for Ni, Co, and Cu. 54

Figure 5.5: Ni and Co measured concentrations with MP-AES vs. actual concentration in the synthetic solution..... 60

Figure 5.6: Al removal (Precipitation 1). 62

Figure 5.7: Al precipitation (%) for NP1, NP2, P1, and P2 in 1st step precipitation. 62

Figure 5.8: Cu, Ni, Co, Mn, and Li precipitation (%) for NP1, NP2, P1, and P2 in the 1st step precipitation. 64

Figure 5.9: Cu removal (precipitation 2). 64

Figure 5.10: Cu precipitation (%) for NP1, NP2, P1, and P2 in 2nd step precipitation. 65

Figure 5.11: Ni, Co, Mn, and Li precipitation (%) for NP1, NP2, P1, and P2 in 2nd step precipitation. 66

Figure 5.12: High Ni precipitation (Precipitation 3). 67

Figure 5.13: Ni, Co, and Mn precipitation (%) in 3rd step precipitation calculated from supernatant composition. 68

Figure 5.14: Ni, Co, and Mn precipitation (%) in 3rd step precipitation calculated from precipitate composition. 69

Figure 5.15: XRD pattern of the NP1 precipitate 3 along with the identified phases. 71

Figure 5.16: Li_2CO_3 precipitation (Precipitation 4 and 5). 73

Figure 5.17: Multi-step precipitation route for P1 leachate. 76

Figure 5.18: Precipitation (%) of Li, Al, Mn, Co, Ni, and Cu versus pH for the multi-step precipitation route of P1. 77

Figure 5.19: Precipitate 3 a) before calcination (metal hydroxide), and b) after calcination (metal oxide). 77

Figure 5.20: Ni, Co, and Mn mass ratios (%) of the precipitate 3 before and after calcination. 78

Figure 5.21: XRD pattern for NP1 and P1 precipitate 3 after calcination. 79

Figure 7.1: Recirculation of 1st precipitate. 83

List of Tables

Table 1.1: Electrochemical parameters depending on cell chemistry [14]. 6

Table 2.1: K_{sp} and pH values for start and end of precipitating various metal hydroxides [28]. 17

Table 2.2: K_{sp} of various metal sulphides [29]. 17

Table 3.1: Solubility of all possible crystallisation products with Na_2CO_3 at 20, 90, and 100ºC [25]. 27

Table 4.1: Set of 9 different synthetic solutions with varying Ni and Co concentration of 50, 100 and 200 mg/L. 41

Table 4.2: Temperature and pressure program for precipitates digestion. 47

Table 5.1: Kinetic parameters during the leaching process calculated using the chemical reaction controlled model. 55

Table 5.2: Kinetic parameters during the leaching process calculated using the diffusion controlled model. 56

Table 5.3: Ni, Co, Cu, and Mn concentrations measured with MP-AES and actual concentrations in 9 prepared synthetic solutions. 58

Table 5.4: Ni and Co concentrations measured with MP-AES and from prepared synthetic solutions. 59

Table 5.5: Initial composition of the leachate solutions analysed with MP-AES. 61

Table 5.6: Metal composition (mass%) of precipitate 3 from NP1, NP2, P1, and P2 leachates. 70

Table 5.7: Precipitate 3 composition (mass%) for NP1 before and after washing step with MΩ water. 72

Table 5.8: Li precipitation (%) and mass (mg) in the P1 precipitate 5 calculated from supernatant and digested precipitate. 74

Table 5.9: Calcined precipitates 3 composition analysed after digestion with MP-AES..... 78

Table 5.10: Ni, Co, Mn molar ratio (%) for NP1, NP2, P1, and P2 metal oxides. 80

Overview of the Report

1. Introduction

A concise introduction of the project including the basics of the lithium-ion battery chemistries, motivation, goals, and state-of-the-art in battery recycling.

2. Theory and Background

Theoretical explanation about the physical, chemical, and thermodynamical properties comprising the two main processes carried out throughout the project (leaching and chemical precipitation).

3. Literature Review

Research work about the most important lithium-ion battery recycling processes carried out in literature and industry up to date. A review on the methodology performed in literature regarding the leaching kinetics and co-precipitation of valuable metals is also presented to stablish the basis of the experimental work developed during this project.

4. Experimental Procedure

Chemicals, equipment, experimental conditions, and procedures carried out throughout the project.

5. Results and Discussion

Results obtained from the experimental procedures explained in the chapter before, and the analysis of data. In addition, a detailed discussion about these results can be found in this chapter.

6. Conclusions

Conclusions which can be stated from the experimental results.

7. Future Work

Closing chapter including recommendations for future work on the selective recovery of valuable metals from spent lithium-ion batteries through the hydrometallurgical route performed.

1 Introduction

In this chapter, an overview about the increasing trend in the use of lithium-ion batteries (LIBs) in electric vehicles (EVs), the need to recycle the valuable metals present in the batteries, as well as the current state-of-the-art of LIBs recycling, are explained. Additionally, the extent and goals of the project, and the structure of the report can be found here.

1.1 Lithium-Ion Batteries (LIBs)

LIBs are the favourable choice over other rechargeable batteries for many applications in portable electronic devices and new low carbon technologies such as solar power, wind power and next-generation vehicles such as per battery (BEV), plug-in hybrid (PHEV) and hybrid (HEV) electric vehicles. Because of their excellent electrochemical properties and reduction of carbon dioxide (CO_2) emissions, the electric transport represents a great market for LIBs as an alternative energy source of mobility to the traditional internal combustion engine (ICE) vehicles. Some of the attractive electrochemical properties of the LIBs compared to other batteries such as lead (Pb)-acid, nickel-metal hydride (Ni-MH), or nickel-cadmium (Ni-Cd), are the high energy and power density, high battery voltage, long charging-discharging cycles and high operating temperatures [1]. With the booming industry of electric and hybrid vehicles, the consumption and scrap of LIBs will considerably increase. According to Figure 1.1, BEV sales will increase a 32% per year from 2015 to 2030, and will reach 21 million of sales. The Covid-19 pandemic will affect global electric vehicle markets, although to a lesser degree than the non-electric passenger car market. Estimates from the International Energy Agency (IEA) show that electric car sales worldwide accounted for about 3% of global car sales in 2020 while in Norway, according to [2], 48% of automobiles sold were fully electric in the first half of the year. This difference in automobile electrification in Norway compared to the rest of the world motivates even more to find an economic and sustainable recycling route for LIBs in the country.

Due to the high content of hazardous heavy metals present in the LIBs, the disposal of the spent batteries without reuse of these components will involve not just environmental problems but also a misuse of metal resources which could become critical in a near future. Ni and Li are classified as critical metals due to their importance for decarbonization and risk of supply depletion by 2060 [3]. Likewise, the high prices for metals found in LIBs (34 USD/kg of Co, 15 USD/kg of Ni and 9 USD/kg of Li (Li does not occur in elemental form, but as Li_2CO_3) [4]) make them very attractive for recycling.

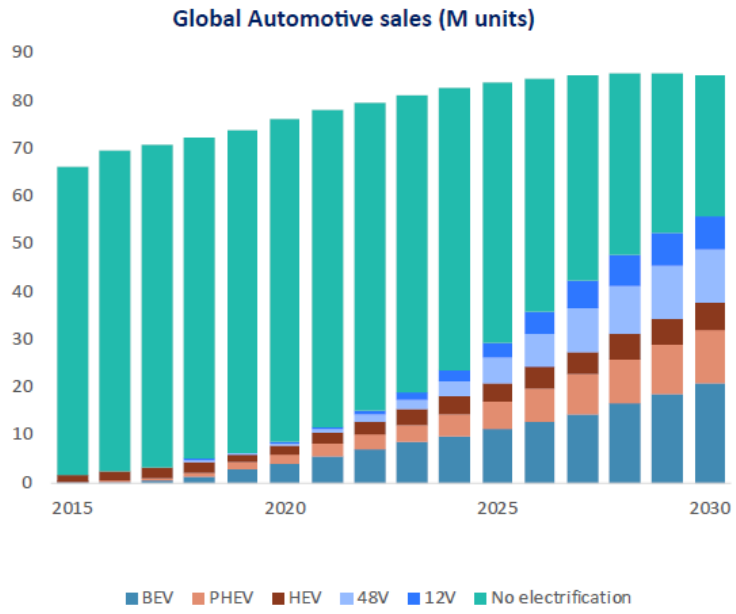

Figure 1.1: Battery (BEV), Plug-in Hybrid (PHEV), Hybrid (HEV), Mild-Hybrid (48V), Micro-Hybrid (12V) Electric Vehicles and ICE vehicles sales (No electrification) by 2030 [5].

This increase in global EV sales of all types in the near future will be due to more economic longer term running costs. Specially, the full powered battery EVs (BEV) sales will steadily increase because of their more competitive battery cost. The battery cost reduction with time will come together with continuous development of battery materials and technologies, as well as the recyclability of spent batteries, which will face also new challenges due to the continuous development of the battery material [6]. Development by means of changes in the composition of electrode materials. Intercalated compounds are used as electrode material in LIBs, generally lithium metal oxides, such as $LiCoO_2$ (LCO), $LiNi_xCo_yMn_{(1-x-y)}O_2$ (NCM), $LiNi_xCo_yAl_{(1-x-y)}O_2$ (NCA), $LiMn_2O_4$ (LMO), or $LiFePO_4$ (LFP) are used as cathode active material (CAM) and graphite carbon material as anodes. Between the two electrodes, there is a permeable membrane soaked with the electrolyte, which is a mixture of organic carbonate solvents such as dimethyl carbonate (DMC), ethyl methyl carbonate (EMC) or diethyl carbonate (DEC), and the conductive salt $LiPF_6$, LiTFSI or $LiBF_4$ which transports the Li ions. The negative and positive electrodes are often referred to as anode and cathode in literature. There are two processes that occur in a battery: charging and discharging. Contrary to the traditional batteries based on redox reactions, LIBs work according to the process called “intercalation” or “insertion”. During the charging process, the Li ions are stripped off from the cathode, transported by the electrolyte to the anode and inserted therein. During discharge, Li ions are extracted from the anode and

migrate across the electrolyte into the crystal lattice of the cathode material, without changing its crystal structure [7]. These two processes are depicted in Figure 1.2.

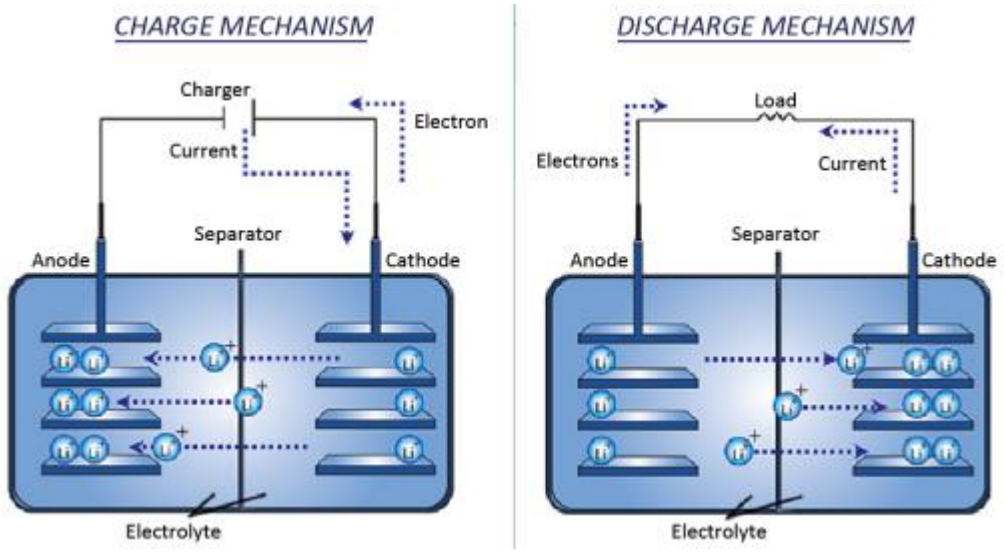

Figure 1.2: Charge and discharge process of a Lithium-ion battery [8].

In conclusion, recycling the LIBs used is EVs becomes a critical process in the automotive sector electrification. It contributes to reduce the EVs cost, which implies an increase in the sales compared to ICE vehicles, alleviates critical metals extraction whose natural resources could become scarce in the future, and contributes to a correct disposal of hazardous heavy metals to the environment and human health.

1.1.1 Introduction into LIBs Recycling Processes

Next generation vehicles have an average LIBs life-time of 10 years [9]. Then, when an EV battery reaches the end of its useful first life, manufacturers have three options: they can dispose it off, recycle the valuable metals, or reuse it. Even though in most regions the regulation prevents disposal, it is the most common practice when cells are damaged. Efficient recycling of valuable metals from spent LIBs has become a very important matter in recent years since they contain a great portion of toxic metals, such as nickel, cobalt, manganese, and lithium, which represent a threat to the environment and human health. These valuable metals have higher value in their pure state than as ores, and therefore they are also important secondary resources for many different metallurgy applications. Having an additional source of battery metals through recycling can be convenient to battery manufacturers that aim for a secure

supply. Recycling can provide the most valuable product in the battery market. By means of resynthesizing the cathode active metals through different pyrometallurgical and hydrometallurgical processes and reintroduce the metal oxide into the electrode production chain, enhancing circular economy. An EV battery life cycle is illustrated in Figure 1.3.

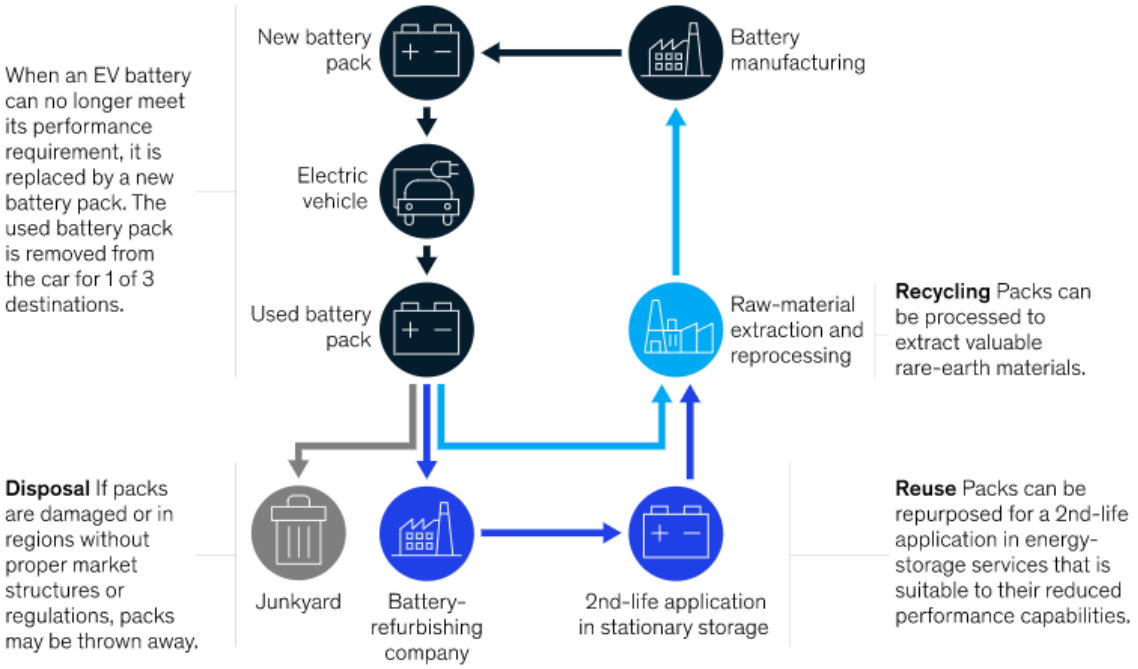

Figure 1.3: EV battery life-cycle [10].

The goal of recycling processes is to separate the components of used batteries into different fractions that can be reintroduced into the manufacture of new batteries for EVs or other electrical devices. The most valuable materials for the metallurgical industry are present in the electrodes. Most LIBs used in EVs have as CAM, lithium (Li) with a mixture of transition metal oxides like nickel (Ni), manganese (Mn) and cobalt (Co) (NMC or NCM). But also, there are other mixtures of metal oxides such as Ni, Co, and Al (NCA) or Ni and Mn (LNMO). The proportion of mixed transition metal oxides like Ni, Mn and Co has been constantly increasing over the years. This metal oxides are coated over an aluminium (Al) foil. Anode material is graphite coated over a copper (Cu) foil, although silicon (Si) is expected to enter as anode material in the future. The result of this scientific progress and constant new cell design and new chemistries, increase the complexity of LIB recycling [7]. Recycling processes for LIBs are a combination of different processes such as deactivation, disassembly, pyrometallurgical, mechanical and hydrometallurgical treatment. Handling of the regained battery modules, cells

or electrodes coating material can be carried out with a first step, pyrometallurgically or mechanically. With pyrometallurgical treatment, Ni, Co and Cu are recovered in the molten mass [11]. Mechanical treatment combines crushing, classification and sorting of the electrode's current collector foils (Cu and Al foils). This simple process facilitates the concentration of the different metals composites in fractions and is easily scalable. Essentially, it separates the Al and Cu electrode foils from the metal oxides present in the CAM. Al and Cu have larger particle sizes after crushing than the Li, Ni, Co, and Mn oxide powder. Hydrometallurgical treatment is applied for the direct recovery of metals, such as Ni, Co, Mn and Li, from the mechanical separated coating materials as well as for extracting Al and Li from slag of pyrometallurgical process [12]. The hydrometallurgical route consists of inorganic or organic leaching of the metal oxides, followed by chemical precipitation or organic solvent extraction of the metals in the leaching liquor and a final calcination step to recover the valuable metals in the oxide form. Further discussion about the state-of-the-art of LIBs recycling is explained in section 2.1.

1.2 Motivation and Goals

There are three main motivations in this project, which are:

- According to estimates from the World Economic Forum, there is a need to scale up global battery production by a factor of 19 to accelerate the transition to a low-carbon economy. Therefore, the EU's commission has stablished the objective of LIBs material recovery rates for Co, Ni, and Li of 90, 90, and 35%, respectively, by 2025 [13].
- As reported in literature [14], EV's batteries make up a significant portion of the total EV cost, varying roughly from the 33% to the 40%. Besides, approximately 60% ~ 80% of the full cost of the CAM is based exclusively on raw material prices, therefore recycling them would considerably decrease battery cell cost.
- According to the International Energy Agency (IEA), Li and Ni are identified as critical metals that require specific measures. Alleviation of the main metal ores for future supply-demand balance could be achieved by recycling, which could lead to a decrease in the primary demand by 20% ~ 70% for next-generation vehicles [3].

To fulfil the criteria specified above, specific goals are set for this project:

- Resynthesize the CAM ($LiNi_XMn_YCo_{(1-X-Y)}O_2$) with high Ni content in the oxide so as to meet future cathode chemistries with higher Ni: Mn: Co molar ratios. Nowadays,

most of the cathodes manufactured are of the NMC-111 ($LiNi_{1/3}Mn_{1/3}Co_{1/3}O_2$) type. However, according to Table 1.1, CAM with higher Ni molar ratios give better electrochemical properties. Thus, future CAMs are evolving towards NMC-442 ($LiNi_{0.4}Mn_{0.4}Co_{0.2}O_2$), NMC-532 ($LiNi_{0.5}Mn_{0.3}Co_{0.2}O_2$), NMC-622 ($LiNi_{0.6}Mn_{0.2}Co_{0.2}O_2$) and NMC-811 ($LiNi_{0.8}Mn_{0.1}Co_{0.1}O_2$) [14]. CAM chemistry of LNMO type of battery cell is formed by $LiNi_{0.5}Mn_{1.5}O_4$.

Table 1.1: Electrochemical parameters depending on cell chemistry [14].

Cell Chemistry	Cell Energy (Wh)	Cell capacity (Ah)
NMC-111	85.5	23.10
NMC-442	86.9	23.47
NMC-532	88.2	23.83
NMC-622	92.1	24.88
NMC-811	94.2	25.45
LNMO	87.6	19.05

- Co-precipitation of Ni, Mn, and Co in order to decrease the precipitation steps and thus, the process operational cost.
- Most CAM recycling processes reported in literature have been done with just the cathode electrode, since in a lab scale and with small loads of battery to recycle, it is relatively easy to separate both electrodes manually. However, separation of electrodes would be much more difficult to perform in an industrial scale, where a high level of automation would be needed. In the pre-treatment, the spent LIBs are manually disassembled to separate anode and cathode materials. The complicated process makes it incompatible for large-scale industrial application [15]. Therefore, in this project both anode and cathode were treated together during the recycling process.
- According to X. Zhang et al. [6], impurities concentration in the LIB CAM should be less than 100 ppm. Cu and Al from the electrode collector foils are considered as

impurities for the CAM resynthesis. Therefore, after first leaching step, precipitation of Cu and Al, with minimal loss of Ni, Mn, and Co, is aimed.

2 Theory and Background

In this chapter a theoretical insight in the physical, chemical, and thermodynamic principles behind the two main chemical processes carried out during the project (leaching and precipitation) is included.

2.1 Leaching

When solid materials come into contact with a liquid, some constituents will dissolve to a greater or lesser extent. The overall leaching mechanism consists of breaking down the crystal lattice of the metal material by using a suitable leaching media. There are a lot of factors that can influence the rate of the elements dissolution from the material matrix into the liquid. These can be divided into physical and chemical factors.

Typical physical factors influencing leaching comprise [16]:

- Homogeneity or heterogeneity of the solid matrix in terms of mineral phases.
- Particle size as leaching is related to the surface exposed to the liquid.
- The reaction time.
- The temperature.
- The porosity of the solid matrix.
- The particle size and shape of the material when leaching is controlled predominantly by diffusion processes.

Typical chemical factors influencing leaching include:

- pH of the material or that imposed by the surroundings (e.g., CO_2 effects)
- Complexation with organics or inorganic compounds.
- Redox conditions of the material or that imposed by the surroundings.
- Sorption processes or reprecipitation processes whereby initially dissolved constituents return to the solid phase.

The physical factors influencing leaching relate clearly to the manner of contact between the liquid and the solid material. Examples of different leaching conditions include a natural soil exposed to rainwater infiltration, a concrete exposed to sea water or a waste exposed to percolating rainwater. In batch experiments, acceleration of leaching is achieved by the

agitation chosen which promotes mass transfer from the solid to the liquid. The particle surface area to volume ratio, the average particle size and internal pore structures in the material all control the surface area where dissolution from the solid to the liquid occurs. Larger surface areas per mass or volume provide faster dissolution at the surface. The chemical and physical or mineralogical properties of a soil, a waste or a sediment subjected to leaching may vary considerably. In a bulk sample consisting of a wide range of heterogeneous particles, as the battery waste electrodes, the leachability reflects the sum of all interactions. The conditions that are needed for leaching to happen are determined by the thermodynamics. Therefore, phase diagrams are often used to determine the solution environment that will be necessary for leaching. The diagrams of the areas of stability show the conditions in which the components of the system in the solid, liquid and gaseous state take part and dissolved species are stable in aqueous solutions. These diagrams may theoretically describe reactions of hydrolysis, oxidation and reduction. The systems are simple, of the type Me-H_2O or more complex such as Me-S-H_2O, Me_1-Me_2-S-H_2O, Me-Cl_2-H_2O, Me-S-Cl_2- Me-S-H_2O, etc. where Me is the examined metal in the solution and are normally plotted in the co-ordinates pH and the oxide-reduction potential E (V). In literature these diagrams are referred either as E-pH or Eh-pH. These diagrams are the same as the so-called Pourbaix diagram used in corrosion studies. In many cases it is important to know the concentration or activity of the individual species in the solution and the proportion of the individual species present. The usual types of diagrams show the individual fractions of the total amount of the metal present in the form of individual species change with a change of the conditions in the system, for example, change of pH, log E, log $\{Cl^-\}$, etc [17]. The E-pH diagrams state the equilibrium conditions of existence of the stable phases of the individual elements in water under equilibrium conditions.

Figure 2.1 and 2.2 show the cobalt and manganese phase diagram that includes several respective compounds. The low pH and high potential regions of the diagram favour dissolved cobalt and manganese species. Since leaching implies solubilization, this diagram shows the conditions needed for extraction and explains the reason why stronger acids such as sulphuric acid (H_2SO_4), nitric acid (HNO_3) or hydrochloric acid (HCl) are the most used for leaching of metals in the LIB cathode waste. It is also important to note that if the potential is above the water stability line, water will break down to form oxygen gas and if it is below the lower water stability line, water will decompose into hydrogen gas and hydroxide ions. According to these diagrams, the cobalt and manganese oxides are stable at high pH and potential values. Analysing the E-pH diagram of Co-H_2O and Mn-H_2O, it is justified the need for a reductant to

improve recovery of cobalt and manganese. According to the E-pH diagram of Co-H_2O, Co^{3+} phase cannot be dissolved even in a strong acid until the redox potential reaches ~1.84 V, being above the water stability line. This makes it difficult to achieve high leaching efficiency under the normal leaching conditions. However, Co^{2+} can be solubilized in acid as its stability region goes up to pH 6.3. In the E-pH diagram of Mn-H_2O, the domain of stable Mn phases is between the stability lines of water and Mn^{2+} can be dissolved in the entire acid region. In order to dissolve Mn^{4+} (MnO_2) phase that is also part of some spent battery cathodes ($Li_2CoMn_3O_8$), a strong reducing condition and strong acid solution is required to form soluble Mn^{2+} phase [18].

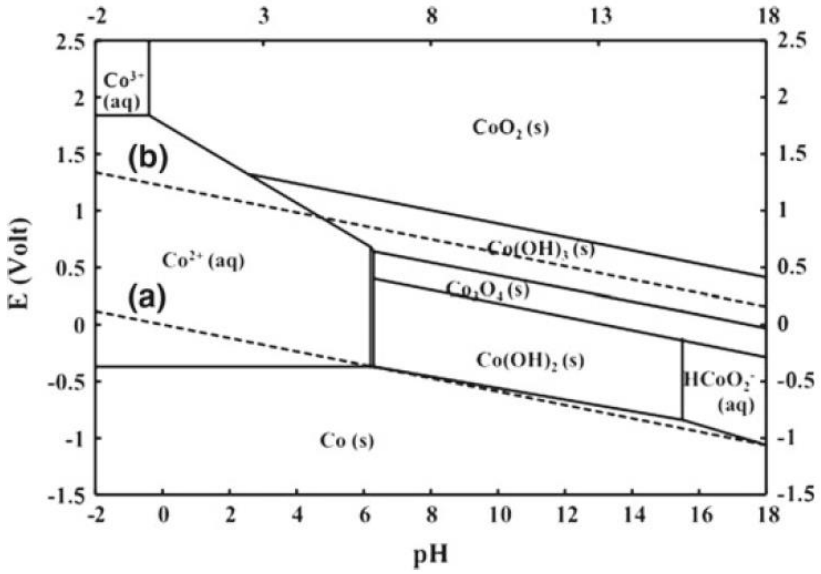

Figure 2.1: E-pH diagram for Co-H_2O system at 298 K [soluble species (except H^+) = 0.5 M at 298 K] [19].

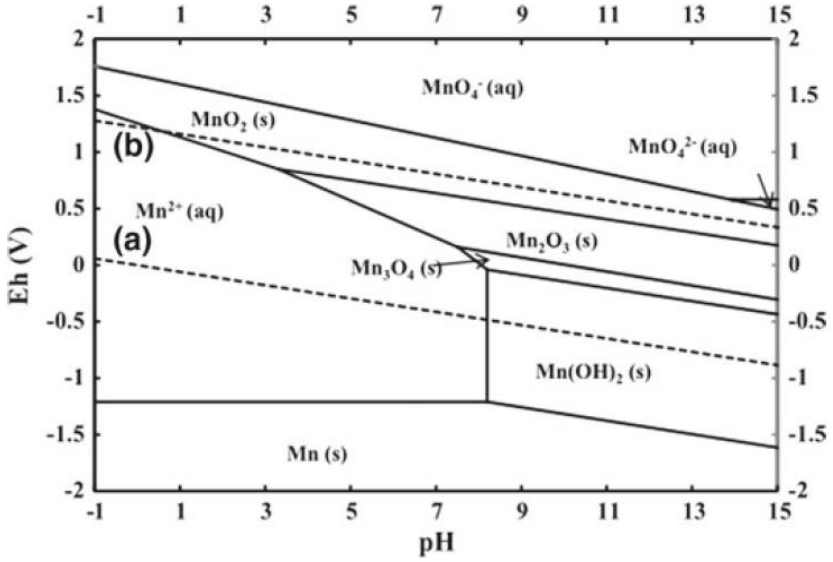

Figure 2.2: E-pH diagram for Mn-H2O system at 298 K [soluble species (except H^+) = 0.5 M at 298 K] [19].

In order to successfully leach cathode materials, specially Co and Mn, adding reductant H_2O_2 to the acid leaching media (H_2SO_4 is the most commonly used) has been reported [20].

2.1.1 Kinetic Models

Thermodynamics provides information on the given system in the equilibrium state and makes it possible to forecast the behaviour of the equilibrium with the change of various external conditions, such as temperature, pressure, concentration of reagents, etc. In the leaching of soluble materials located inside a particle by means of a solvent, the following general steps can occur in the overall process. The solvent must be transferred from the bulk solvent solution to the surface of the solid. Next, the solvent must penetrate or diffuse into the solid. The solute dissolves then into the solvent. The solute diffuses through the solid solvent mixture to the surface of the particle. Finally, the solute in transferred to the bulk solution.

In general, the rate of transfer of the solvent from the bulk solution to the particle surface is quite fast, while the rate of transfer of the solvent into the solid may be either fast or slow. These are not though, in many cases, the rate-limiting steps in the overall leaching kinetic. The solvent transfer occurs initially when the particle is first put in contact with the solvent. The dissolving of the solute into the solvent inside the solid can be either a simple physical dissolution process or an actual chemical reaction that frees the solute for dissolution. The rate of diffusion of the solute through the solid and solvent to the surface of the solid is often the controlling resistance in the overall leaching process and may depend on many different factors. The diffusion through the porous solid can be described by an effective diffusivity. The void fraction and tortuosity are needed to be considered in this case.

When a material is dissolved directly from the solid surface to the solvent solution, however, the rate of mass transfer from the solid surface to the liquid is the controlling factor. There is basically no resistance inside the solid phase if it is a pure material. This case can also be used when diffusion in the solid is very rapid compared to diffusion from the particle surface [21].

In the research of kinetics process, four leaching models, such as shrinking core, empirical, Avrami equation, and revised cubic rate law models, have been proposed to analyse the leaching kinetics of different metals. However, the most wide-spread model used for leaching of spent LIB cathode material is the shrinking core. The leaching process can be explained as a solid-liquid heterogeneous process including mass transfer, ion diffusion and surface chemical reactions as mentioned above. Therefore, based on the shrinking core model, the leaching rate

can be assumed to be controlled by the solution film mass transfer (Eq. (1)), the surface chemical reaction (Eq. (2)), or product layer diffusion (Eq. (3)) [22].

$$X = k_m \cdot t \tag{1}$$

$$1-(1-X)^{1/3} = k_r \cdot t \tag{2}$$

$$1-3(1-X)^{2/3}+2(1-X) = k_d \cdot t \tag{3}$$

Where X is the leaching efficiency of metals, t is leaching t time, and k_m, k_r, and k_d are the apparent reaction rate constants which can be obtained from the slopes of the fitted plots where t is on the x axis and the component at the left side of equations (1), (2) and (3) are in the y axis. As explained before, the rate of mass transfer of the solvent from the bulk solution to the particle surface (Eq. (1)) is quite fast, so this is not usually the rate determining step in leaching reactions of cathode material. Therefore, the equations normally used to determine the kinetics of the leaching are Eq. (2) and (3). Most of the reported data in literature for leaching of cathode metals in spent LIBs fit the surface chemical reaction controlled model.

- Shrinking Core Models (SCM)

The different ways that reaction occur at the particle surface are:

- Figure 2.3 (a): The soluble part of the solid shrinks until it disappears as the reaction progress.
- Figure 2.3 (b): The soluble part of the solid may also react to produce an insoluble product whereby the reacting core shrinks while the particle does not vary in size.
- Figure 2.3 (c): The soluble part of the solid react and a gelatinous layer is formed around the surface of the particle while the unreacted core shrinks.

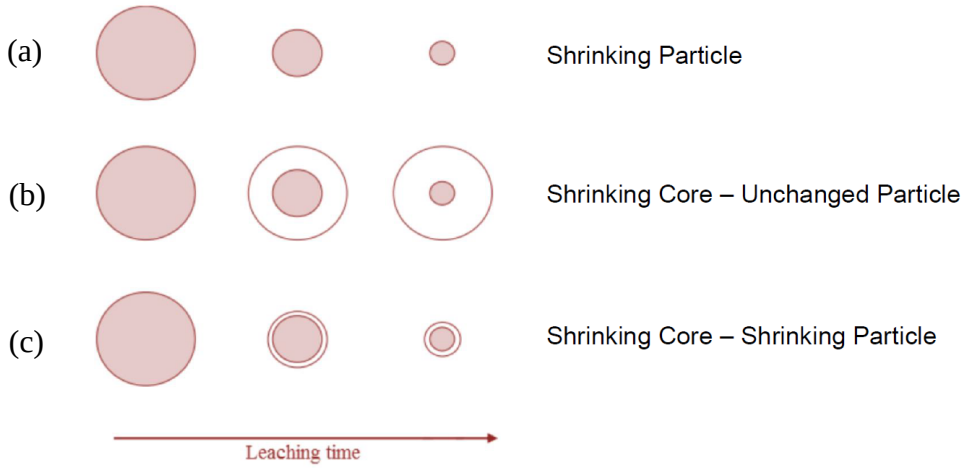

Figure 2.3: Mechanisms of leaching in the shrinking core model [23].

Figure 2.3 illustrates the most popular models in hydrometallurgy since many leaching processes adapt to kinetic models for heterogenous solid-liquid reactions which are best described by these models. Following the LIB hydrometallurgical route, the recovery of the cathode active metals step comes after the leaching step, and metal precipitation is the process most commonly used.

2.2 Precipitation

Precipitation usually refers to a relatively fast formation of a sparingly soluble solid phase from a liquid phase. The formation of precipitates occurs under relatively high supersaturation conditions. Because of the presence of high supersaturation, nucleation plays a key role in the precipitation process. Nucleation is the first step in the formation of the new phase. The nuclei form via the dynamic and stochastic association of monomeric units that overcome a free energy barrier at a crystal size and result in a phase separation in the system. As a result, a large number of crystals with relatively small sizes are produced during precipitation. Crystal size is typically between 0.1 and 10 μm. Nonetheless, because of the high particle concentration and small crystal size, some secondary processes may occur, such as agglomeration, aggregation, and ageing, affecting the properties and characteristics of the precipitates. Agglomeration processes result in permanent attachment via growth of particles together, commonly in systems with high supersaturation and high number of particles. This phenomenon increases the crystal size of the precipitate. Aggregation instead, is a reversible clustering of particles due to weak physical forces such as Van der Waals interactions, H-bonding, etc. Agglomeration rate can be significantly reduced by increasing the stirring rate, while aggregation is greatly affected by acoustic forces such as sonication. The supersaturation needed for triggering precipitation frequently results from a chemical reaction. Hence, precipitation is sometime referred to as reactive crystallization. Despite, there are two more techniques of precipitation apart from the chemical precipitation, which are cooling and salting our precipitation. Many important properties of the precipitates are physical in nature. The crystal size distribution and crystal habit or morphology can have a great impact on the post-precipitation processes, such as filtration, drying, etc [24]. In order to control these physical properties of the precipitates, apart than the secondary processes briefly explained above, the nucleation thermodynamic properties of the precipitates may be also controlled.

2.2.1 Thermodynamic Properties

For sparingly soluble precipitates, precipitation is generally achieved by mixing solutions of reacting components. The solubility of the precipitating component must be known in order to determine the driving force for the reaction. Solubility is defined as the concentration of the species in a solution that is in equilibrium with a solid phase at the specified temperature. All solubility values are expressed as mass percent of solute, $100 \cdot w_2$, as shown in Eq. (4).

$$w_2 = m_2 / (m_1 - m_2) \tag{4}$$

Where m_2 is the mass of solute and m_1 the mass of water [25]. When a precipitate coexists in equilibrium with the solution, the appropriate equilibrium constant is the solubility product, K_{sp}. A saturated solution of a specific element is in thermodynamic equilibrium with the solid phase at a specific temperature (concentration of element in solution is same as at equilibrium). Solutions where concentration is higher than at equilibrium are called supersaturated. A schematic plot of the different zones regarding saturation of an element are shown in Figure 2.4 with a concentration versus temperature graph. Normally for most salts, solubility increases with temperature (except for Li_2CO_3 which decreases with temperature, as explained in section 3.1.2).

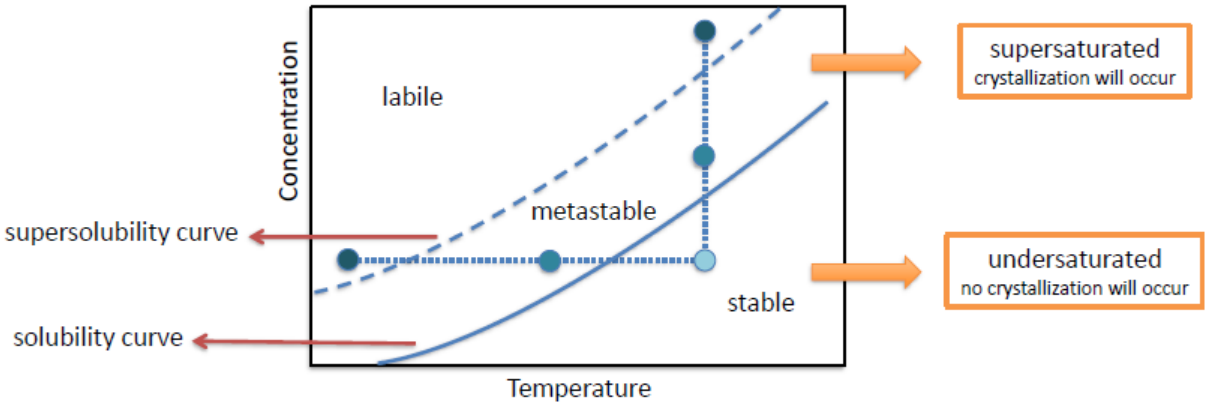

Figure 2.4: Stable, metastable, and labile zones of a specific element in a concentration vs. temperature plot [26].

In the stable zone, the solution is undersaturated with respect to the species studied, crystallization or precipitation is impossible to happen spontaneously. In the metastable zone, the solution is supersaturated and within the solubility and supersolubility curve, spontaneous precipitation is probable to occur. The labile zone corresponds to the supersaturated solution where the concentration of the species studied is above the supersolubility curve and therefore,

uncontrolled spontaneous precipitation occurs. For an electrolyte $A_{v+}B_{v-}$, the supersaturation ratio S can be defined as the ratio of the ionic activity product (IAP) to the activity-based solubility product (K_{sp}). Where a is the activity of the ionic species, or also called effective concentration, expressed in Eq. (7).

$$K_{sp} = (a_{A+})^{V+}{}_{eq} \cdot (a_{B-})^{V-}{}_{eq} \tag{5}$$

$$S = \left(\frac{(a_{A+})^{v+}(a_{B-})^{v-}}{K_{sp}} \right)^{1/(v_+ + v_-)} = \left(\frac{IAP}{K_{sp}} \right)^{1/v}, v = v^+ + v^- \tag{6}$$

$$a = c \cdot \gamma \tag{7}$$

Where γ is the activity coefficient, c the concentration of the species studied, and v the number of moles of ions formed from one mole of electrolyte. The activity coefficient (γ) depends on ionic strength of the solution, size, and charge of the component. High concentration of reactants does not necessarily mean that the free concentration of ions is equally high in solution. For very dilute solutions γ approaches to 1 and activity can be replaced with concentration (ideal solutions). In this case supersaturation is defined as shown in Eq. (8)

$$S = \left(\frac{C_{A+}^{v+} C_{B-}^{v-}}{(C_{A+})_{eq}^{v+} (C_{B-})_{eq}^{v-}} \right)^{1/v} \tag{8}$$

For a homogeneous nucleation reaction, the total Gibbs free energy change, ΔG, is the sum of the free energy change for phase transformation, ΔG_V, and the free energy change for the formation of the surface, ΔG_S. ΔG_V is the excess free energy of the metastable solution (negative value) over the solid deposition, and ΔG_S the energy cost of creating a solid-liquid interface (positive value).

$$\Delta G = \Delta G_V + \Delta G_S = \Delta G_v V + \gamma A \tag{9}$$

From Eq. (9) ΔG_v is the free energy change of phase transformation per unit volume (J/m^3), V is the volume of the particle formed (m^3), γ is the surface free energy of the interface (J/m^2), and A the surface area of the particle (m^2). In heterogeneous nucleation over a solid surface, the interfacial free energy (ΔG_S) is changed depending on favourable or unfavourable nucleus-surface interactions due to reduction of the nucleus interfacial area (A).

Generally, it is difficult to directly measure the activity or concentration of reactants independently one from another. Unless a very sensitive electrode is applied for each reactant, the direct measurements of the supersaturation is rarely possible. Accordingly, the ratio of

concentration of one reagent which can be monitored independently is used as a measure of the supersaturation [27].

Consequently, the chemical precipitation is a very important method to recover the metals of interest either as raw materials or together as co-precipitates depending on their solubility products, after the leaching step. The co-precipitation of the cathode active metals Ni, Co, and Mn becomes very important when the goal is to regenerate the CAM directly from spent LIBs leaching liquor. In order to separate the three main metals Ni, Co, and Mn from the two impurities present in the leachate Cu and Al, the solubility limits of the different salts (hydroxides and sulphide in case of Cu) are exceeded at different pH values, being the pH, the parameter controlled. The Al reaches the minimum concentration at pH of 4.49, if it is in the form of $Al(OH)_3$, and therefore it is not a major concern for loosing Ni, Co, or Mn. Cu on the other hand reaches the minimum concentration at pH of 6.65, if it is in the form of $Cu(OH)_2$ [28]. The solubility of a metal hydroxide, $M(OH)_n$, is related to the solubility equilibrium and the pH according to the following equations:

$$K_{sp} = [M^{n+}][OH^-]^n \tag{10}$$

$$K_w = [H^+][OH^-] = 10^{-14} \tag{11}$$

$$pH = -\log_{10}[H^+], \qquad [H^+] = 10^{-pH} \tag{12}$$

$$K_{sp} = [M^{n+}] \cdot (10^{pH-14})^n \tag{13}$$

Table 2.1 shows the K_{sp} and the pH number of the metal ions starting to precipitate and precipitated fully when the concentration of H_2SO_4 is 4M in the leachate.

Table 2.1: K_{sp} and pH values for start and end of precipitating various metal hydroxides [28].

Substance	**K_{sp}**	**pH_{start}**	**pH_{end}**
$Al(OH)_3$	$3.00 \cdot 10^{-30}$		4.49
$Cu(OH)_2$	$2.00 \cdot 10^{-20}$		6.65
$Ni(OH)_2$	$5.48 \cdot 10^{-15}$	5.16	8.87
$Co(OH)_2$	$5.92 \cdot 10^{-15}$	6.67	9.39
$Mn(OH)_2$	$2.00 \cdot 10^{-13}$	7.40	10.15

Due to the overlapped pH range of precipitation for the Cu and Ni hydroxides from pH 5.16 to 6.65, a more adequate precipitant agent to remove selectively Cu minimising the Ni loss is Na_2S instead of NaOH. The K_{sp} difference between the NiS and CuS is 10^{12} bigger than the difference between the hydroxides, as shown in Table 2.2.

Table 2.2: K_{sp} of various metal sulphides [29].

Substance	**K_{sp}**
CuS	$6.31 \cdot 10^{-36}$
NiS (α)	$3.16 \cdot 10^{-19}$
CoS (α)	$3.98 \cdot 10^{-21}$
MnS	$2.51 \cdot 10^{-10}$

This low solubility of CuS in acid solution is the reason why the Cu sulphide precipitation method is used more widely than hydroxide and carbonate precipitation. In order to precipitate the metals in different streams and in a specific order, several precipitation steps will be necessary, and the order of precipitation will depend on the solubility product of the metal salt aimed to precipitate, from lower to higher K_{sp}.

3 Literature Review

In this chapter, the most important LIB recycling processes carried out in literature and industry are presented. More focus is made regarding the hydrometallurgical route further performed during this project (leaching of electrode powder, co-precipitation, and calcination of active metals).

3.1 LIBs Recycling Process

During the last years, researchers have shown great interest in recovering valuable metals from the CAM in the EV battery, composed of $LiNi_xCo_yMn_{(1-x-y)}O_2$. These metals (such as Ni, Co and Mn) can be extracted by HNO_3, HCl, citric acid and H_2SO_4 with H_2O_2 or $NaHSO_3$ [30] in a leaching step after the mechanical pre-treatment (dismantling and classification, crushing, sieving and separation). Even though metals can be leached with high leaching rate, the similar properties of these metals make the metal separation from the leach liquor of the metal oxide cathode material more complicated [31]. To recover these metals from their mixed leachate, a stepwise process involving selective co-precipitation or solvent extraction is necessary. In this chapter more attention will be on the co-precipitation since it is the process studied during the project, instead of solvent extraction. To shorten metal separation, cathode materials from leach liquor is treated without separating Ni, Co, and Mn individually. After precipitation, to regenerate $LiNi_xCo_yMn_{(1-x-y)}O_2$ cathode material, the obtained precipitated precursor of Ni, Co and Mn is mixed together with Li source. The blend is sintered in a furnace to produce the oxidation reaction. The simplified LithoRec process is shown in Figure 3.1. It combines electrical, mechanical, mild thermal, and hydrometallurgical treatment with the aim of recovering nearly all valuable materials of the batteries [12].

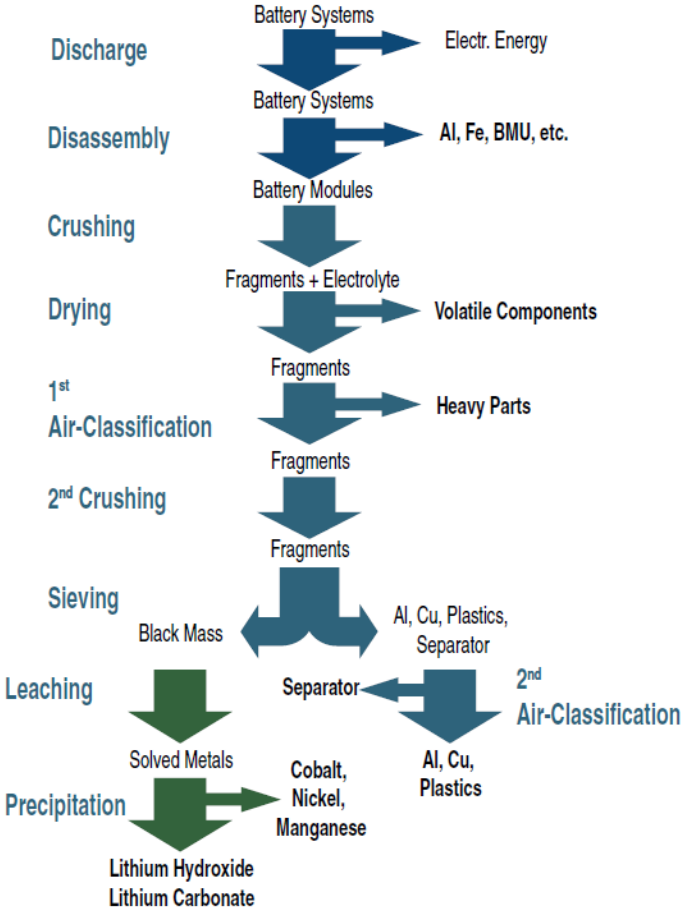

Figure 3.1: LithoRec process of battery recycling [12].

The simplified process shown above contains most of the important pre-treatment steps (blue arrows) carried out before the pyro or hydrometallurgical treatment. Following, this pre-treatment is explained.

1) Pre-treatment

The LIB structure is complex with a lot of different components, so pre-treatment processes are necessary to remove the case and to concentrate the valuable metal fraction, facilitating the next pyrometallurgical or hydrometallurgical recycling. Safety measures should be stressed during pre-treatment processes, especially in industrial applications. The hazard potential of LIBs can be divided into three areas [12]: electrical hazard, fire and explosion hazard, and chemical hazard. The electrical hazard is determined by the stored electric energy and high voltage which could provoke an electric shock. After crushing, “micro-short-circuits” between anode and cathode fragments could lead to elevated temperatures due to joule heating. The presence of flammable carbonates in the electrolyte (DMC, EMC, or DEC) as explained in section 1.1,

contribute to the fire explosion hazard due to the highly flammable reaction products, like methane, ethane, and propene. There is also a chemical hazard in the pre-treatment step concerning the decomposition of the conductive salt $LIPF_6$ at around 60ºC [12] and the corresponding release of HF and other toxic gases. Besides, the partly carcinogenic CAM (Ni and Co oxides) are considered as chemical hazard.

About the mitigation of these hazards, this project focuses on the chemical hazards concerning the carcinogenic metal oxides (Ni and Co) mitigation. This chemical hazard is abated downstream on the recycling path (hydrometallurgy or pyrometallurgy processes), while the electrical and explosion hazards are faced in the pre-treatment step, as well as the chemical hazard regarding the HF gaseous product. HF leads to the necessity of a gas scrubber installation during disassembly and crushing. Removal of the electrolyte also minimizes this chemical hazard and the fire hazard potential as the flammable products are eliminated. Following, the different steps in the pre-treatment of the recycling of spent batteries are explained.

a. Dismantling and classification

For industrial applications, where the volume of battery waste from EVs to be recycled is huge, preliminary dismantling to smaller modules or cells is recommended to avoid some potential hazards explained above. Currently, because of the large variation in cell design depending on the different manufacturers, most battery packs are dismantled manually by specialized operators. However, this can be a problematic method to deal with the big quantities of spent LIBs in the coming years and instead, high level of automation of the equipment responsible of dismantling the battery cells is necessary to improve pre-treatment efficiency [6].

b. Crushing and sieving

During the crushing step, cathode and anode components are put in contact and can cause micro-circuits. To minimize the hazards corresponding to this micro-circuits and heating explained before, deactivation or preventive steps are carried out before or during crushing. Discharge in salt solution of sodium chloride (NaCl) can be applied before to remove the remaining energy. Additionally, crushing can also be performed in salt solution, called wet crushing, to diminish the toxic emission and reactivity of the electrodes. The wet crushing is safer than dry crushing but can also introduce more impurities in the fine fraction because of the scouring action of the water flow [6]. Crushing step consists of reducing the particle size and distribution

of the metal oxides present in the CAM and separate them from the electrode foils (Cu and Al). Following the crushing there is a sieving operation, used to separate and concentrate the metallic fractions. Different fractions are obtained in this step, but the most relevant are the fine fraction (< 1 mm) and the coarse fraction (> 1 mm). Generally, the coarse fraction contains the separator, plastics, Al foil, and Cu foil, while the metal oxides present on the CAM are present within the fine fraction.

c. Mechanochemical treatment

Mechanochemistry is a branch of chemistry which is concerned with chemical and physical-chemical transformations of substances in all states of aggregation produced by the effect of mechanical energy. The mechanical activation is a term well known in this field that appeals to an increase in reaction ability of a substance which remains chemically unchanged due to stable changes on the solid structure. It increases the internal energy, surface energy and the specific surface area [32]. High energy milling is the most widely used method to provide the mechanical force to trigger chemical reaction. In recycling of spent batteries, mechanochemical reactions are commonly used as a pre-treatment to improve the recycling efficiency breaking the crystal structure of the cathode material to improve the following leaching process [6]. According to Zhang et al., crystalline $LiCo_{0.2}Ni_{0.8}O_2$ in battery scrap was pulverized by grinding for 60 and 240 minutes, and it became amorphous. They showed this mechanochemical treatment to be very effective, due to the high leaching efficiencies obtained with the subsequent leaching step at room temperature. Accordingly, Co, Ni and Li were extracted at a higher than 90% yield from the amorphous scrap sample [33].

2) Pyrometallurgical processes

The pyrometallurgical process is a thermal treatment that enables recovery of valuable metals from ores and concentrates through physical and chemical transformations. Because of their high energy consumption and emission of hazardous gases, other processes such as the hydrometallurgical are getting more attention for study in laboratory scale research [6]. On the other hand, many industrial-scale enterprises use the pyrometallurgical process because of simplicity and high productivity. It has been widely investigated in recovering Zn, Ni, Cd and other heavy metals from spent Zn-Mn dry batteries or Ni-Cd batteries [34]. Commonly, smelting of the metals scrap or ores was used in pyrometallurgical methods to separate metals in which some go to the slag and the target metals turn into alloy. In a typical pyrometallurgical

process, Li ends up in the slag residue and it is lost, unless is further extracted with hydrometallurgical processes (leaching out Li from the slag). This, as well as the high energy consumption and the rigorous requirements for the off gases produced, as previously mentioned, are the biggest challenges for the pyrometallurgical processes in LIBs recycling.

3) Hydrometallurgical process

Due to its low energy consumption, low toxic gas emissions and cost, higher metal selectivity and recycling efficiency compared with pyrometallurgical processes, hydrometallurgical methods are the most used approaches for recycling spent LIBs. This is embraced by the fact that more than half of the recycling processes reported are hydrometallurgical processes [18]. Although some challenges still exist in these methods, including the complex operation steps and wastewater produced, it is well known that hydrometallurgical strategies have greater potential than the pyrometallurgical methods to realize sustainable development of the LIBs recycling industry. Typically, hydrometallurgical processes consist of an initial leaching step, followed by purification procedures such as chemical precipitation, solvent extraction, electrochemical deposition, etc [7].

3.1.1 Leaching of Cathode Active Metals from Spent LIBs

Leaching is the key step for recovering valuable metals from spent LIBs in the whole hydrometallurgical process. It is used to dissolve metals in the spent material from the solid state to the solution for further processing. Therefore, the overall recycling rate of the metals is significantly influenced by the leaching efficiency. In early research, inorganic acid reagents such as H_2SO_4, HNO_3, and HCl were widely used as leaching agents and were demonstrated to be effective. Nonetheless, disadvantages like the emission of secondary pollutants or complexity of separation and purification in the following steps, also appear. The leaching efficiency of Co and Mn without reductants follows the order HCl > HNO_3 ≈ H_2SO_4. Therefore, the leaching efficiency of most reagents would be unsatisfying without a reductant like H_2O_2 as explained in section 2.1. The leaching agent most used in literature is the H_2SO_4 [7]. Based on previous studies on the influence of several parameters in H_2SO_4 leaching, the solid to liquid (S/L) ratio and acid concentration are the main parameters influencing the solubilization of Mn, Ni, and Co from spent batteries [7]. The leaching reaction for a cathode powder of $LiNi_{0.33}Co_{0.33}Mn_{0.33}O_2$ is as the chemical equation (1) [28]:

$$6LiNi_{0.33}Co_{0.33}Mn_{0.33}O_2 + 9H_2SO_4 + H_2O_2 \rightarrow 2MnSO_4 + 2NiSO_4 + 2CoSO_4 + 3Li_2SO_4 + 2O_2 + 10H_2O \quad (1)$$

According to Swian et al.'s work [35], 93% of Co and 94% of Li can be leached under optimized conditions of 2 M H_2SO_4, 100 g/L of S/L ratio, 5 vol.% of H_2O_2, 75ºC, and 30 minutes leaching time for a $LiCoO_2$ CAM. Other reductants agents such as $NaHSO_3$ have also been used instead of H_2O_2. This is the case of Pratima et al.' work [36], where they used 1 M H_2SO_4, 20 g/L of S/L ratio, 0.075 M $NaHSO_3$, 95ºC, 500 rpm, and 4 h reaction time. The achieved recovery in their case was 96.7% Li, 91.6% Co, 96.4% Ni, and 87.9% Mn for a CAM consisting of $LiNi_{0.33}Co_{0.33}Mn_{0.33}O_2$. The leaching efficiency depend on the type of CAM to be leached [7].

Generally, a kinetic model is matched with the leaching experiments, and taking data from the model, activation energy for each metal can be determined. Besides, determine the leaching mechanism and rate of leaching for each metal in the acid used, is also the aim of the kinetic study, as it has been for this project.

- Leaching kinetics

The shrinking core model explained in section 2.1.1, which includes surface chemical reaction control (Eq. (2)) and the internal diffusion control model (Eq. (3)), are widely applied to describe the leaching kinetics of the metals from LIBs. Another kinetic equation that is also used to describe the metals leaching for some heterogeneous processes is the Avrami equation [15] shown in Eq. (14).

$$-\ln(1-X) = k_c \cdot t^n \tag{14}$$

Which is a mixed control model, including diffusion and surface chemical control. This model, as well as the shrinking core, were investigated in Fei M. et al.'s work [15] to verify their suitability for the data from the LIB leaching experiments with citric acid ($C_6H_8O_7$) at different temperatures. The experiments indicated that the Avrami equation was more suitable than the shrinking core model to describe the leaching of Li, Co, Ni, and Mn with linear correlation coefficients (R^2) > 0.98. It was also reported that when *n* in the Avrami equation is above 0.5, the process is controlled by the surface chemical reaction. In their job, all *n* values for Li, Co, Ni, and Mn were higher than 0.55 indicating that the leaching process was controlled by the surface chemical reaction. Furthermore, this was confirmed by the influence of temperature on the leaching efficiencies of all metals studied.

According to another previous study on leaching kinetics of LIBs electrode material with formic acid (HCOOH) and H_2O_2, it was found that two characteristic stages exist for the leaching rate against temperature in the range of 30 to 80ºC. From 60 to 80ºC, the values for k_r (reaction rate

constant) are nearly identical regardless of the increase in temperature and henceforth no longer reaction controlled.

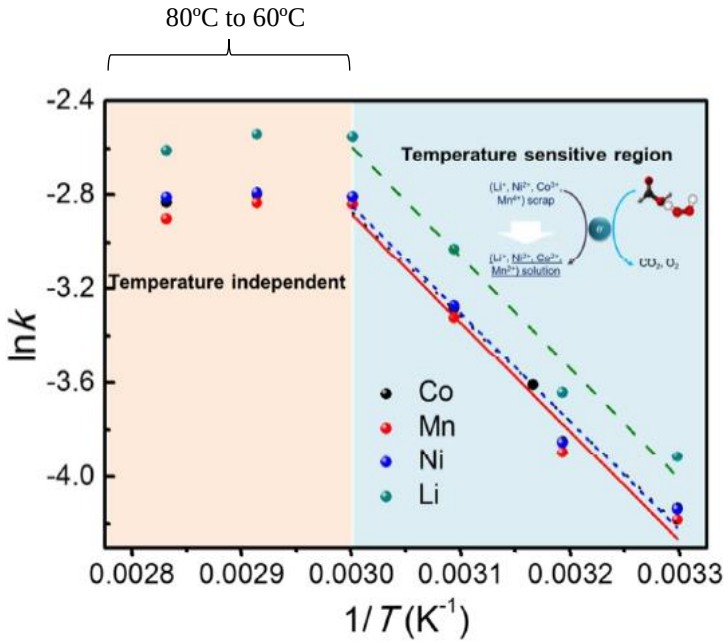

Figure 3.2: Arrhenius plots for leaching of Co, Mn, Ni, and Li from the cathode scrap under the surface chemical controlled model [37].

In the figure shown above from literature, *ln k* against *1/T* was plotted because the goal of their study was to obtain the activation energy from the linearized Arrhenius equation (Eq. (15)) in the leaching experiments at different temperatures.

$$\ln k = \ln A - \frac{Ea}{RT} \tag{15}$$

They realized that data could be described by the empirical Arrhenius law in the range of 30-60ºC. Temperatures higher than 60ºC are not temperature sensitive. Therefore, reaction becomes diffusion controlled since the chemical reaction occurs faster than the time it takes for the species to move and come into contact. In the diffusion controlled model, kinetics depends on the concentration gradient between bulk and particle surface, stirring rate and geometry of the particles [38]. Once the metals of interest have been dissolved in the leaching media, the next step is their recovery in solid state through chemical precipitation.

3.1.2 Co-precipitation of Cathode Active Metals from Leachate

When some precipitants containing special anions such as OH^-, $C_2O_4^{2-}$, and CO_3^{2-} are added into a leaching solution, the valuable metals in solution may combine the anions to form

precipitates. In order to decrease the precipitation steps, co-precipitation has often been used to precipitate two or more metals together. In this process, the aim has been to precipitate together Ni, Co, and Mn as they are the metals present in the CAM, apart from Li. For this co-precipitation, in most of the experiments performed on literature, the concentrations of Ni, Co, and Mn in the leaching solution were adjusted first [39] to get the targeted molar ratio of Ni: Co: Mn in the precipitate. Then, these metals are usually co-precipitated in the form of $Ni_XCo_YMn_{1-X-Y}(OH)_2$, $Ni_XCo_YMn_{1-X-Y}CO_3$ or $Ni_XCo_YMn_{1-X-Y}C_2O_4$ by adding NaOH, Na_2CO_3 or $H_2C_2O_4$, respectively. Finally, the $LiNi_XCo_YMn_{1-X-Y}O_2$ CAM can be resynthesized by reacting in a calcination the precipitates with Li_2CO_3 at a certain stoichiometric ratio. Li_2CO_3 decreased solubility with increased temperature [25], unlike the other metals precipitated. Therefore, high temperature during this last precipitation step enhances the Li recovery.

It should be stressed that the performance of precipitation is highly dependent on the pH value of the solution. As explained in section 2.2.1, the Al and Cu content in the leaching solution due to the electrode collector foils must be removed before the co-precipitation of Ni, Co, and Mn. The Figure 3.3 shows the metal precipitation versus pH at 40ºC by titration with NaOH in H. Wang et al.'s work [40].

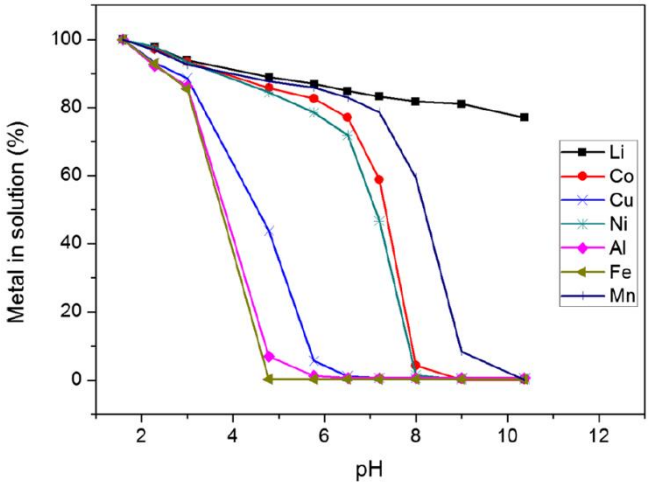

Figure 3.3: Metal precipitation using NaOH at 40ºC from H_2SO_4 leaching solution [40].

The content of Al and Cu in the solution decreases rapidly from pH 2.3 to 4.8. Clearly, Cu precipitates less than Al at the same pH value. When pH 4.8 is achieved, 6.9% of Al and 43.8% of Cu are still in solution. At the pH of 5.8, when all the Al and more than 90% of Cu have precipitated, the co-precipitation (loss) of Ni, Co, and Mn have reached values of 21.4, 17.3, and 14.1%, respectively. At this point, these losses have already reached relatively high values,

which cannot be ignored. Finally, Ni, Co, and Mn are completely precipitated from the solution at pH 10.37. In addition, Li in solution decreased by 20% at pH 10.37 because of absorption in the precipitate surface. This loss of Li by absorption has also been quantified during the multi-step precipitation performed in this project, as shown in section 5.4. In order to be able to selectively remove Cu without a significant loss of Ni, Co, and Mn, Na_2S is commonly used in literature before the co-precipitation with NaOH of these metals. In Figure 3.4 the metal precipitation using Na_2S is shown.

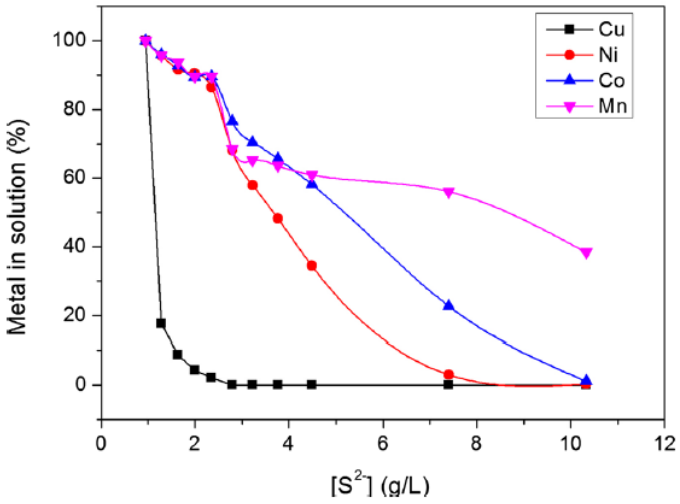

Figure 3.4: Metal precipitation using Na_2S at 40ºC from H_2SO_4 leaching solution [40].

Addition of Na_2S does not directly modify the pH of the solution as the NaOH does by adding OH^- ions to the solution. Therefore, the metal precipitation (%) is plotted against S^{2-} concentration added to the leaching solution (g/L) instead of pH like in Figure 3.3. Due to the low solubility of CuS, Cu concentration in solution decreases very fast and ~ 96% of Cu can be removed by adding 2 g/L of S^{2-}, while the loss of Ni, Co, and Mn is still < 10%.

After removing Ni, Co, and Mn, the precipitate of Li_2CO_3 is produced by adding an excess of sodium carbonate. Because of the lower concentration of Li^+ in the leachate, the filtrate after the Ni, Co, and Mn removal needs to be evaporated to concentrate Li to values close to 1.4 g/L at 100ºC [36]. The solubility of the possible salts forming when adding Na_2CO_3 to the leachate is shown in Table 3.1 at different temperatures.

Table 3.1: Solubility of all possible crystallisation products with Na_2CO_3 at 20, 90, and 100ºC [25].

Solubility (g/L)	Li_2CO_3 (Li)	Na_2CO_3	Li_2SO_4	Na_2SO_4
20ºC	13.3 (2.5)	215	348	195
90ºC	7.8 (1.5)	439	309	427
100ºC	7.2 (1.4)	-	-	425

In the table shown above, the values in parenthesis are the Li concentrations required in the solution to reach the specified solubility limits of Li_2CO_3. The purity of the crystallised Li_2CO_3 obtained in [40] reached 90.9%, which represented a 17.2 mass% of Li in the product. Regarding to the efficiency, 59.7% of Li was precipitated, while the rest remained in the raffinate. In the other hand, in P. Meshram et al.'s work [36], they recover a 98% purity Li_2CO_3 precipitate. Nonetheless, they did not specify the efficiency of this last step precipitation.

After the recovery of Ni, Co, and Mn free of Al and Cu, and Li in a different precipitation stream, the resynthesis of the CAM $LiNi_XCo_YMn_{1-X-Y}O_2$ is the next and final step performed through a calcination reaction.

3.1.3 Resynthesis of Cathode Active Metal Oxides

The final step for the resynthesis of the metal oxides present in the CAM consists in a calcination. Calcination is a thermal treatment process for solid materials that comprises thermal decomposition, phase transformation, or removal of the volatile substances in the absence or limited supply of oxygen. In metallurgical processes, calcination is a common method to process minerals that can be decomposed to generate a desirable compound [22].

The calcination conditions and procedures can vary slightly for different CAM compositions. According to [41], the optimal stoichiometric ratio of Li: Me is 1.05, being Me the sum of Ni, Co, and Mn moles in the hydroxide precipitate. For $Ni_{0.33}Co_{0.33}Mn_{0.33}(OH)_2$, it was preheated at 500ºC for 5 h then calcined in air at 900ºC for 20 h; for $Ni_{0.5}Co_{0.2}Mn_{0.3}(OH)_2$, it was preheated at 500ºC for 5 h then calcined in air at 850ºC for 15 h; finally, for $Ni_{0.8}Co_{0.1}Mn_{0.1}(OH)_2$, it was preheated at 480ºC for 5 h then calcined in pure oxygen at 750ºC for 20 h.

4 Experimental Procedure

4.1 Materials

In this section the chemical reagents and the different set-ups used for the porpoise of the project are presented. The processes described here, as well as the chemical reagents used during the master thesis project were thoroughly risk assessed. The detailed risk report ID is 33432 and can be found at https://avvik.ntnu.no/risk.

4.1.1 Chemical Reagents

The spent LIBs scraps used as a starting material for the recycling process (leaching, co-precipitation and calcination) were a mixture of spent cathode and anode obtained by removing the plastic and steel cases from completely discharged LIBs. They were cut into pieces, crushed, and milled to obtain a fine particle size of < 150 μm, to accelerate the leaching reaction rate. Three different types of powder have been used: powder crushed at the Crystallisation laboratory in the Chemical Engineering Department at NTNU (Norway) coming from leaf cell batteries (CAM composed by $LiNi_{0.5}Mn_{1.5}O_4$ (LNMO)) and from prismatic cell batteries (NMC), and on the other hand, prismatic cell batteries pyrolyzed at Aachen University (Germany) and then crushed. Leaching reagents used in this study include sulphuric acid (H_2SO_4, 95%, TECHNICAL, VWR) and hydrogen peroxide (H_2O_2, 35 wt. %, ACS reagent, Sigma-Aldrich). Sodium hydroxide (NaOH, Merck Millipore) and sodium sulphide hydrate ($Na_2S{\cdot}H_2O$, > 60%, Merck Millipore) were used for preparing the precipitation agent solutions. Different synthetic solutions were prepared for precipitation experiments and Microwave Plasma Atomic Emission Spectroscopy (MP-AES) validation method with manganese (II) sulphate monohydrate ($MnSO_4{\cdot}H_2O$, > 99%, ACS reagent, Sigma-Aldrich), cobalt (II) sulphate heptahydrate ($CoSO_4{\cdot}7H_2O$, > 99%, ReagentPlus®, Sigma-Aldrich), nickel (II) sulphate hexahydrate ($NiSO_4{\cdot}6H_2O$, > 98%, ACS reagent, Sigma-Aldrich) and cupper (II) sulphate ($CuSO_4$, > 99%, ReagentPlus®, Sigma-Aldrich). All solutions were prepared with deionized water. Concentrated hydrochloric acid (HCl, 37%, Acros Organics) was used for the complete dissolution of metal precipitates and calcined metal precipitates using a microwave digestor (Speedwave Xpert), and MP-AES was used to determine metal content in the digested material. Additionally, lithium carbonate (Li_2CO_3, > 99%, ACS reagent, Sigma-Aldrich) was mixed with the recovered CAM of high Ni content, Co, and Mn precipitate before calcination.

4.1.2 Experimental Set-up

The different set-ups for all the chemical processes carried out during the project are presented here.

- Leaching

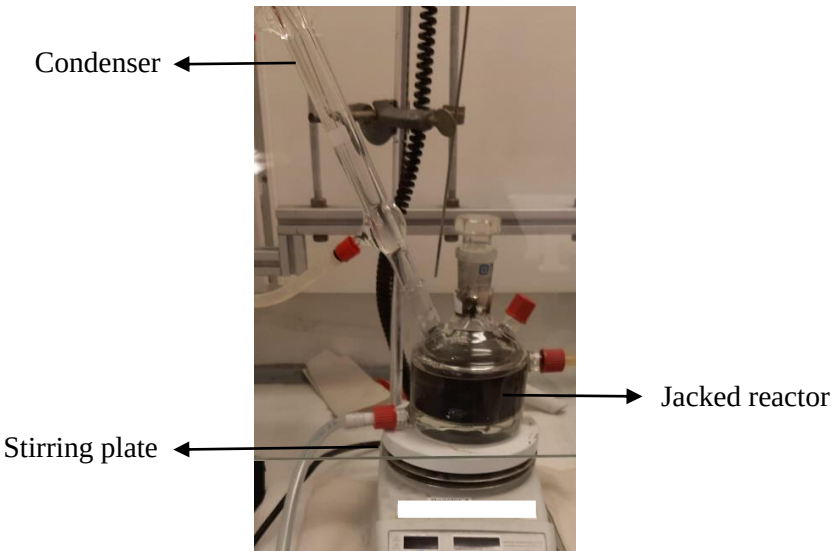

Figure 4.1: Leaching set-up.

Temperature of 80ºC for the leaching experiments was reached with a heating water circulator (HighTech HE Heating Circulator, Julabo) connected to the jacked reactor of 250 mL. Stirring speed was set to 360 rpm. Reagents (H_2SO_4 with H_2O_2 and the battery crushed powder) were poured in the reactor through the upper necked opening.

- Precipitation

Initial precipitation experiments (preliminary experiments with synthetic solution) were performed in batch using a beaker. A burette was used to add the precipitant agent (NaOH) dropwise. The precipitation experiments were performed at 60ºC and 300 rpm. Hence, some evaporation of the solution occurred. Initial and final volume of the solution were measured for metal precipitation calculations. Despite, precipitation experiments with the leachate obtained from leaching of crushed battery powder were carried out in a closed double jacketed reactor of 250 mL with condenser to minimize evaporation as shown in **Figure *4.3*:** Closed jacked reactor precipitation set-up.Figure 4.3. This was also a batch setup.

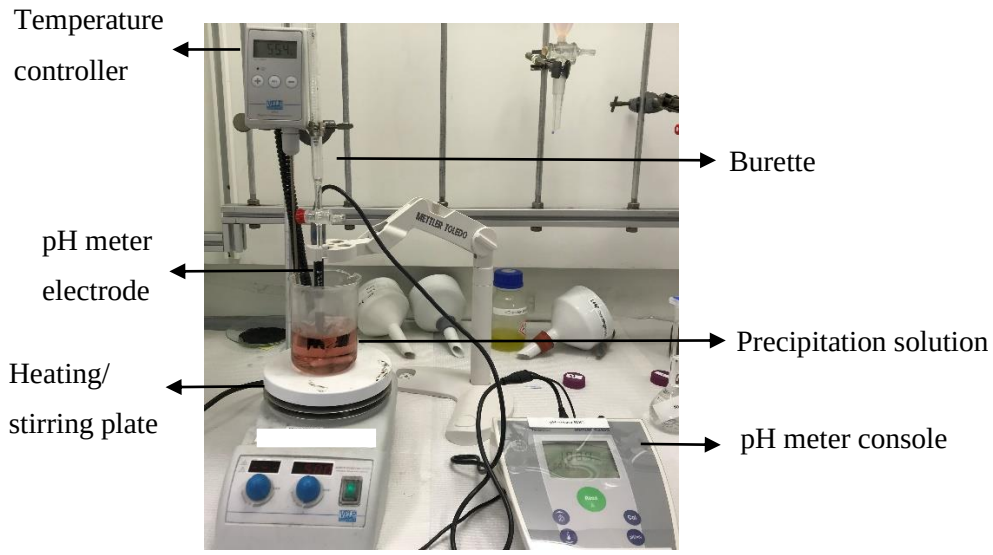

Figure 4.2: Beaker precipitation set-up.

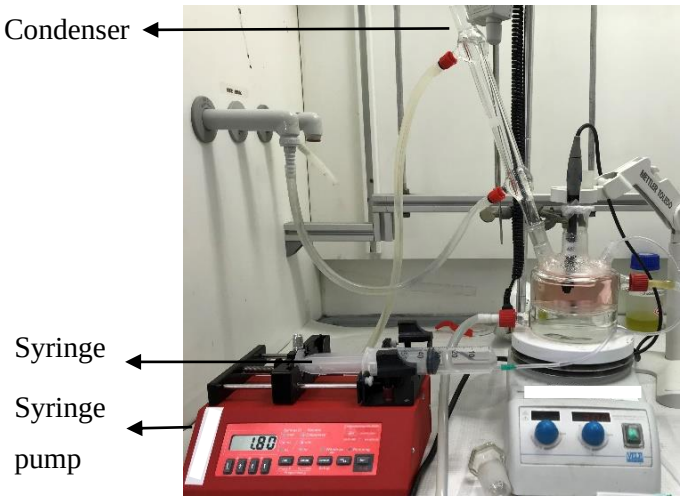

Figure 4.3: Closed jacked reactor precipitation set-up.

In the closed reactor precipitation set-up, temperature was increased using a heating water circulator (HighTech HE Heating Circulator, Julabo). Furthermore, the precipitant was added with a syringe pump at specific flowrate instead of with a burette. The pH electrode was introduced through the upper necked opening and covered with parafilm to avoid evaporation. The precipitant in the 60 mL syringe was pumped through a 2 mm diameter tube connected to the right necked opening of the reactor.

- Vacuum Filtration

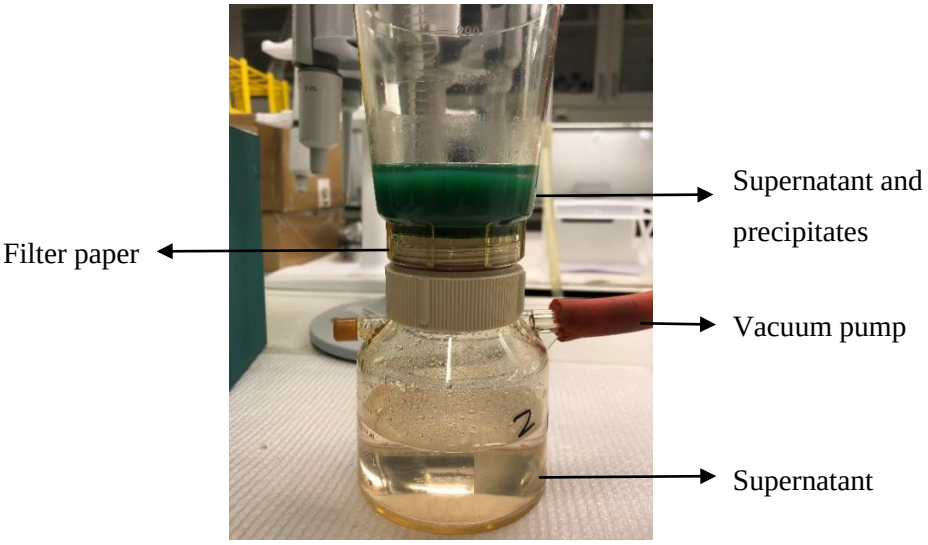

Figure 4.4: Vacuum precipitation set-up.

After each precipitation experiment, the solution containing the precipitates and supernatant was vacuum filtered to separate them. Leaching solution after the leaching kinetics experiments containing the non-leached material (mostly graphite) was also vacuum filtered. For the precipitation experiments, a filter paper with 0.22 μm of pore diameter was used (Durapore ® PVDF Membrane, Merck Millipore) while for the final leachate of the leaching kinetics experiments, a filter paper with a particle filtration size of 4 – 12 μm was used (Whatman ® Grade 589/2, Ashlesh Filter Paper, Merck Millipore).

4.1.3 Characterization Techniques

Brief descriptions of the physical principles behind all characterization techniques used during this project are presented in this chapter.

- Ultraviolet-visible Spectrophotometer (UV-VIS)

The equipment used was the "UV-2401PC (Shimadzu)", which has a single monochromator system with a spectral range between 190 - 1100 nm. A monochromator generally is composed of prisms and slits. The various wavelengths of the light source which are separated by the prism are then selected by the slits such the rotation of the prism results in a series of continuously increasing wavelength to pass through the slits. UV-Vis spectroscopy measures and interpretates the electromagnetic radiation absorbed in the region from ultra-violet light (200 - 400 nm) to visible light (400 - 750 nm). The equipment used during this project also

measures a small fraction of the infra-red region (750 – 1100 nm). Basically, spectroscopy is related to the interaction of light with matter. As light is absorbed by matter, the result is an increase in the energy content of the atoms or molecules. The more easily excited the electrons, the longer the wavelength of light it can absorb. The absorption of ultraviolet light by a chemical compound will produce a distinct spectra which facilitates the identification of the compound. As explained briefly in section 4.2.1, the Beer-Lambert Law states that the concentration of a substance in directly proportional to the 'absorbance', A, of a solution (Eq. (16)). This law is only true for monochromatic light, that is light of a single wavelength or narrow band of wavelengths and given that the physical or chemical state of the substance does not change with concentration [42].

The UV-Vis is a rapid and low-cost analysis technique. Therefore, it is attractive to analyse the kinetics of the leaching where there are many samples. A picture of the equipment is shown below.

Figure 4.5: UV-VIS Shimadzu UV 2401PC Spectrophotometer.

- X-Ray Fluorescence (XRF)

The XRF equipment used during this project was the "Rigaku Supermini 200". This technique determines the elemental composition of the sample, either solid or liquid, by measuring the fluorescent (secondary) X-ray emitted from the sample when it is excited by a primary X-ray source. Elemental analysis from oxygen to uranium can be analysed [43]. X-rays produced by a source (X-ray tube, synchrotron, or a radioactive material) irradiate the sample and the elements present in the sample emit fluorescent X-ray radiation with discrete energies (equivalent to colours in optical light) characteristic for these elements. By measuring the energies (determining the colours) of radiation emitted by the sample it is possible to determine the elements present. This is the qualitative analysis. By measuring the intensities of the emitted

energies (colours) it is possible to determine the quantity of each element in the sample. This is the quantitative analysis. There are three main interactions when the X-rays contact matter: Fluorescence, Compton scatter and Rayleigh scatter, as shown in Figure 4.6. If a beam of X-ray photons is directed towards a piece of material, a fraction is transmitted through, a fraction is absorbed (producing fluorescence radiation) and a fraction is scattered back. Scattering can take place with and without a loss of energy, known as Compton scatter and second Rayleigh scatter, respectively [44].

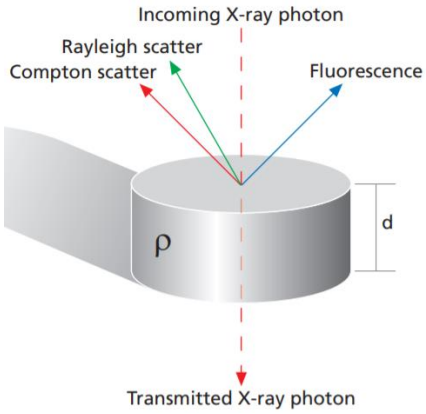

Figure 4.6: Three main interactions of X-rays with matter [52].

During this project, XRF as a quantitative characterization technique was used to measure the precipitates of some preliminary precipitation experiments performed with a synthetic solution. Despite, the goal of this preliminary precipitation experiments with the synthetic solution was to prove the optimal pH at which 100% of Ni precipitated, while keeping Co and Mn in the solution in certain amount. This optimal pH had already been studied in the previous specialization project [45]. Therefore, these results are included in the Appendix. XRF was used to quantitatively characterize the precipitates at the first stage of the project due to easy going functioning and cheap operational costs of this equipment. Nevertheless, there are some limitations with the use of this technique. The most important limitation is that Li is not detectable with XRF since it gives elemental analysis from oxygen (atomic number 8) to uranium (atomic number 92) [43]. Therefore, elements with lower atomic number than oxygen, such as nitrogen, carbon, boron, beryllium, or lithium are not detected. Another limitation of the technique is that elemental metal quantitative analysis are normalized values in mass%, regardless of whether the elements are in form of sulphates, hydroxides, or oxides. This limitation of the equipment does not permit to calculate absolute concentrations of the elements in the sample, but relative compositions or ratios, such as precipitation efficiencies (%).

Moreover, from the supernatant sample analysis with XRF, results showed more than 98 mass% of water [45], and in some cases the metal composition in the supernatant is close or below the lower detection limit of the equipment. A picture of the equipment is shown below. From the multi-step precipitation of the different leachates, initially the precipitates where analysed with XRF. Nevertheless, due to the disadvantages presented above, the characterization method for quantitative analysis of the precipitates was changed to the Microwave Plasma-Atomic Emission Spectrometer (MP-AES). A picture of the XRF equipment is shown below.

Figure 4.7: XRF Rigaku Supermini200.

- Microwave Plasma-Atomic Emission Spectrometer (MP-AES)

The MP-AES model used was the Agilent 4210. The atomic emission technique uses the fact that once an atom of a specific element is excited, it emits light in a characteristic pattern of wavelengths, emission spectrum, while it returns to the ground state. The source for atomic emission is the nitrogen microwave plasma (MP) at temperatures nearing 5,000 K. At these temperatures, atomic emission is strong, producing excellent detection limits and linear dynamic range between emission intensity and concentration for most elements. Inside the MP-AES instrument, microwave energy from an industrial magnetron is used to form the plasma from nitrogen that is extracted from compressed air by Agilent's Nitrogen Generator. The liquid sample is introduced as an aerosol using a nebulizer and a spraychamber. The aerosol is then introduced into the centre of the hot plasma. The aerosol is dried, decomposed, and atomized. The atoms continue to be excited and emit light at characteristic wavelengths. Emission from the plasma is directed into a fast scanning monochromator (same device that UV-Vis uses to emit light at specific wavelengths) [46]. The monochromator filters the emitted light at the

selected wavelength range, and it is then imaged onto a high efficiency CCD (charge-couple device) detector. A CCD detector is an integrated circuit that basically converts incoming photons into electron charges at the semiconductor-oxide circuit allowing light detection. MP-AES quantifies the concentration of an element in a sample by comparing its emission to that of known concentrations of the element, plotted on a calibration curve. As explained in section 4.2.2, MP-AES was used to analyse the leachates and supernatant after each precipitation step, as well as the digested precipitates.

Figure 4.8: Agilent MP-AES 4210.

- X-Ray Diffractometer (XRD)

The XRD used during this project to characterize the precipitates and metal oxides after calcination was the Bruker D8 A25 DaVinci X-ray Diffractometer. The instrument is used to measure crystallographic texture. It consists of three basic elements: X-ray tube, a sample holder, and an X-ray detector. X-rays are generated in a cathode ray tube by heating a filament to produce electrons and bombarding the target sample. When electrons have sufficient energy to dislocate inner shell electrons of the sample, characteristic X-ray spectra is produced. Filtering these spectra, by crystal monochromators, is required to produce monochromatic X-ray needed for diffraction. The interaction of the incident rays with the sample produces constructive interferences and a diffracted ray when conditions satisfy Bragg's Law ($n\lambda=2d\cdot sin\theta$). This law related the wavelength of electromagnetic radiation to the diffraction angle (λ) and the lattice spacing in a crystalline sample (d) as shown in Figure 4.9.

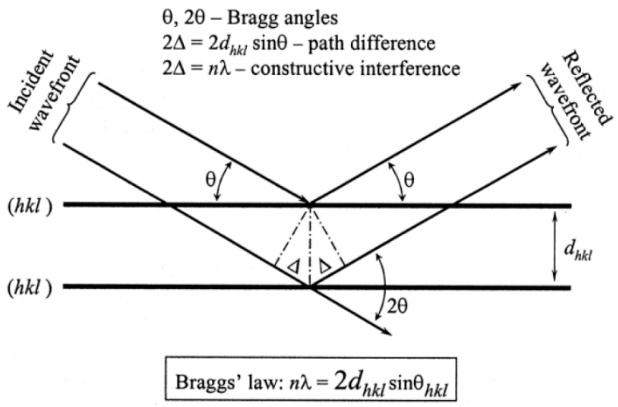

Figure 4.9: X-ray source and diffracted from sample in XRD analysis.

The XRD was used to characterize the precipitates from 3rd precipitation, shown in section 4.2.3, and the metal oxides from 3rd precipitate after calcination. It was used to analyse the grade of crystallinity and the chemical compounds in which the precipitates were, i.e., metal hydroxides, sulphates, sulphides, complexes, etc. Scans were made over a 2θ range of 15 – 75º with variable divergence slit, using a Cu-anode radiation source with X-ray wavelength of 1.54 Å. A picture of the equipment is shown below.

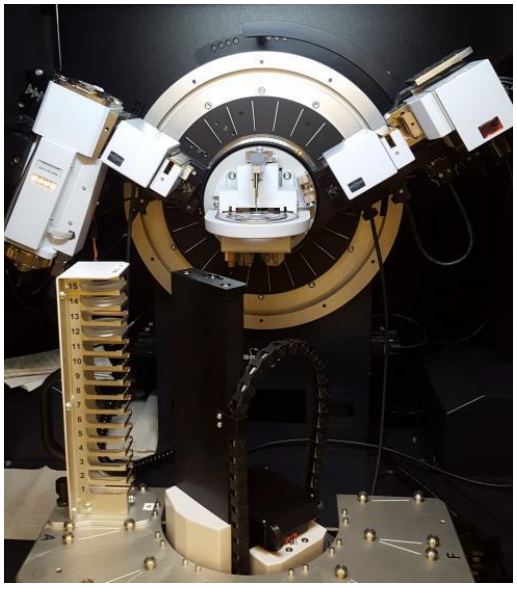

Figure 4.10: XRD Bruker D8 A25 DaVinci.

- <u>High Temperature Furnace</u>

The high temperature furnace HTC 03/14 from Nabertherm with SiC rod heating was used to perform a calcination step at 850ºC with the metal hydroxides precipitates with high Ni

content and Li_2CO_3. The Nabertherm calcination furnace is used to calcine powder samples on air from the environment at temperatures up to 1,200ºC. A picture of the furnace is shown below.

Figure 4.11: High temperature furnace Nabertherm HTC 03/14 used for calcination of precipitates [53].

4.2 Methodology

In this section the procedures carried out as part of all the recycling processes, characterization of the samples and equipment validation methods are explained.

4.2.1 Leaching Kinetic Studies

The leaching kinetics of three different types of pre-treated spent electrodes (leaf, prismatic non-pyrolyzed and prismatic pyrolyzed battery cells) were evaluated before the following valuable metals (Ni, Co, Mn, and Li) were recovered through multi-step precipitation and calcination. Several leaching experiments have already been studied before this project in the group (Hydrometallurgy Research Group of Reactor Technology and Environmental Engineering, Chemical Engineering department of NTNU) optimizing the important parameters affecting the leaching efficiency, such as S/L ratio, temperature, H_2O_2 concentration, stirring speed and type of battery powder used [47][48][49]. However, no leaching kinetic experiments had previously been studied in the research group. Therefore, since leaching is the first step in the hydrometallurgical recycling route of LIBs and highly determining on the final metal recovering yield, the leaching kinetics were studied to determine the controlling step of the reaction and time.

The conditions selected for leaching were adapted from previous studies [47]. Leaching was performed at 80ºC, with 2 M of H_2SO_4, at 360 rpm. The reactions were performed in a total volume of 250 mL and a S/L ratio of 30 The parameters varied were H_2O_2 vol.% (3.75 and 7.5%) and type of battery powder, which basically varies the powder composition (leaf LNMO or prismatic NMC) and possible impurities present such as remaining electrolyte for the non-pyrolyzed or Al and Cu from the collector foils. Finally, a set of 6 experiments was performed, two for each of the three types of electrode powder (with 3.75 and 7.5 vol.% of H_2O_2).

The total leaching time was 1 hour and samples of 2 mL from the leaching media were taken at 1.5, 2.5, 5, 7.5, 10, 15, 20, 30, 50 and 60 minutes to measure the metal composition leached out along with time. Subsequently, percentage conversion was calculated using UV-Vis spectroscopy. Every time a sample was taken, the 2 mL were poured into a vial, cooled down with tap water at room temperature to stop the reaction, and filtered with a syringe filter of 0.45 μm of particle filtration size (13 mm Syringe Filter PTFE, VWR).

Three specific peaks within the UV-VIS spectra were studied: 392 nm corresponding to Ni, 512 nm to Co, and 755 nm to Cu. These are the three main metals present in the leachate that show absorbance in the UV-VIS spectra. Mn and Li are also present but do not show any absorbance peak in this spectra as demonstrated in previous work with UV-VIS spectrometer with leached battery electrodes in the research group [50]. According to Beer Lambert's law, there is a linear relationship between the concentration and the absorbance of the metals in the solution as given by the Eq. (16) (where A is the absorbance, ε absorption coefficient, c concentration and l the optical path length).

$$A = \varepsilon c l \tag{16}$$

Accordingly, measuring the absorbance of the solution at the three wavelengths stated above is an indirect measure of the concentration of the respective metals.

To identify the apparent leaching mechanisms of the electrode scrap powder using H_2SO_4 and H_2O_2, kinetic analysis was carried out in accordance with the leaching behaviour of the three metals. Leaching of metals from the cathode scrap is a solid-liquid heterogeneous process, and is a combination of diffusion and chemical reaction, so the leaching rate can be assumed to be controlled by the surface chemical reaction (Eq. (2)) or the internal diffusion (Eq. (3)) within the liquid boundary layer as explained in section 2.1.1. The absorbance values for the three specific peaks of Ni, Co and Cu were plotted against time. From these absorbance values, the

conversion X_i for a metal i (Eq. (17)) was calculated at the different times assuming that they reach 100% conversion at 60 min.

$$X_i(t) = \frac{Abs_i(t)}{Abs_i(60\,\text{min})} \tag{17}$$

Then, $1-(1-X)^{1/3}$ and $1-3\cdot(1-X)^{2/3}+2\cdot(1-X)$ from Eq. (2) and (3) were plotted against time for the reaction controlled and diffusion controlled model respectively. Both models were plotted for the time where 90% conversion was reached. The regression coefficient (R^2) values from the linearized models (Eq. (2) and (3)) were then compared to check which of the two models fitted better a linear equation (R^2 closer to 1).

After this first step of the hydrometallurgical recycling route, the leaching solutions containing the active metals of the cathode are transferred to the multi-precipitation step. But before this, a validation method for the Microwave Plasma Atomic Emission Spectroscopy (MP-AES Agilent 4210) was performed in order to use it to characterize quantitatively the supernatant and digested precipitate samples.

Due to the limitations of the equipment XRF explained in section 4.1.3, the metal mass% results from a precipitate sample are normalized to 100% without showing the Li content, nor the hydroxide group in the form that they might be. This is a restriction if the aim is to calculate a specific metal absolute quantitative value from the sample, but it is still valid to calculate ratios of an element or relative values from different precipitates (except for Li), i.e., to calculate precipitation (%) from one stage precipitation to another one. Furthermore, from the supernatant sample analysis with XRF, results showed more than 98 mass% of water [45], and in some cases the metal composition in the supernatant is close or below the lower detection limit of the equipment. Due to all these limitations of the XRF as a characterization technique for the precipitates and the supernatant, a validation method for the Microwave Plasma Atomic Emission Spectroscopy (MP-AES Agilent 4210) was performed in order to use it to characterize supernatant and digested precipitate samples from the multi-step precipitation of the real leachates.

4.2.2 MP-AES Validation Method

The MP-AES gives a much more accurate and sensitive analysis than XRF. It also has a higher spectrum of elemental analysis, making possible to measure Li. Before start analysing samples from the recycling process, a validation matrix with synthetic solutions of known metal concentrations was made to validate the measured values from the process samples.

First of all, an external calibration curve was prepared with an ICP multi-element standard solution of 1,000 mg/L for 23 elements in diluted 1% nitric acid (HNO_3) (Ag, Al, B, Ba, Bi, Ca, Cd, Co, Cr, Cu, Fe, Ga, In, K, Li, Mg, Mn, Na, Ni, Pb, Sr, Tl, Zn, Centipur ®, Merck). This standard solution was selected because it contains all elements aimed to be analysed in the supernatant and precipitates from the process (Ni, Co, Mn, Cu, Al, Li and Na). Although it is a standard solution for ICP spectroscopy, it can be used for MP-AES analysis as well, the difference between them two is the concentration of total dissolved solids that both techniques can bear in the sample. While for an ICP the total dissolved solids can be up to 25 mass% (250,000 ppm), for an MP-AES they can be approximately up to 3 mass% (30,000 ppm) [46]. The multi-element stock solution was diluted for calibration of the MP-AES in the range 1-10 mg/L. All dilutions made throughout the project were prepared with 18.2 MΩ water. In MP-AES the elements are evaluated on the wavelength emitted of their atom lines (nm). Each element has several atom lines with different intensities that can be analysed. For example, Cu 324.754, Cu 327.395, Li 610.365, and Li 670.784 nm are the two atom lines with higher intensities for Cu and Li. Depending on the element atom line analysed, the concentration upper limit of the equipment can be very low. This is what happens in the case of Li, for which the intensity of its main atom line is so high that the equipment is saturated at very low concentrations (~ 5 mg/L of Li). For Li, the intensities the instrument can analyse are 6,658,009 c/s for 670.784 nm and 101,059.3 c/s for the 610.365. At concentrations higher than 5 mg/L of Li in the sample solution, the Li 670.784 becomes saturated, with intensities higher than 6,658,009 c/s while for the Li 610.365 the signal is below 101,059.3 c/s up to 10 mg/L of Li. Therefore, a linear relationship between concentration and intensity could be performed for Li 610.365 in the range 1-10 mg/L. This is the reason why the calibration standard was done in the range 1-10 mg/L for all elements, although Ni, Co and Mn for example could be calibrated with a good linear relationship up to concentration of 200 mg/L. This high sensitivity for Li is due to the lower first ionization energy for Li. Upon ionization, the element is not detected using its atom line. Additionally, Li and Na have similar ionization energies (520.2 kJ/mole and 498.8 kJ/mole respectively) and the large fraction of Na excited can increase the signal from Li line [51]. This two effects could lead to misinterpretations of the Li concentration analysed. Calibration curves for Li, Ni, Co, Mn, Cu, Al, and Na are plotted in the Appendix.

The atom lines analysed for Co and Ni were 340.512 and 352.454 nm, respectively. According to the MP-AES Agilent software there is a possible interference between these two atom lines. Therefore, the first thing to check with the prepared synthetic solutions of known concentration

was if this possible interference was affecting the measures for these two metals. A factorial design of two factors (Ni and Co) and three levels of concentrations for Ni and Co (50, 100, and 200 mg/L) was carried out, with a total of 9 synthetic solutions. In addition, Mn and Cu were present in the solutions simulating a real leachate sample but keeping their concentration constant throughout the 9 synthetic solutions (300 and 200 mg/L respectively). Solutions were prepared from the metal sulphates described in section 4.1.1. The concentrations of the 9 synthetic solutions prepared are shown below. The calibration curve from the standard solution in this case was done in the range 1-20 mg/L with five points and the blank (18.2 MΩ water), as shown in the Appendix. Therefore, the synthetic solutions prepared were 10 times diluted so that the concentration fitted inside the calibration curve.

Table 4.1: Set of 9 different synthetic solutions with varying Ni and Co concentration of 50, 100 and 200 mg/L.

N.º	Ni (mg/L)	Co (mg/L)	Cu (mg/L)	Mn (mg/L)
1	49.9	49.6	199.1	298.8
2	99.8	49.6	199.1	298.8
3	49.9	99.3	199.1	298.8
4	99.8	99.3	199.1	298.8
5	199.5	99.3	199.1	298.8
6	199.5	198.5	199.1	298.8
7	99.8	198.5	199.1	298.8
8	49.9	198.5	199.1	298.8
9	199.5	49.6	199.1	298.8

An example of the synthetic solutions nº1 preparation is depicted in Figure 4.12. Stock solutions of 200 mg/L for Ni, Co and Cu separately were prepared from the metal sulphate. In the case of Mn, the concentration prepared was 300 mg/L. From these stock solutions, different volumes were added together and diluted to get a final concentration of the metal between the calibration curve range (1-30 mg/L).

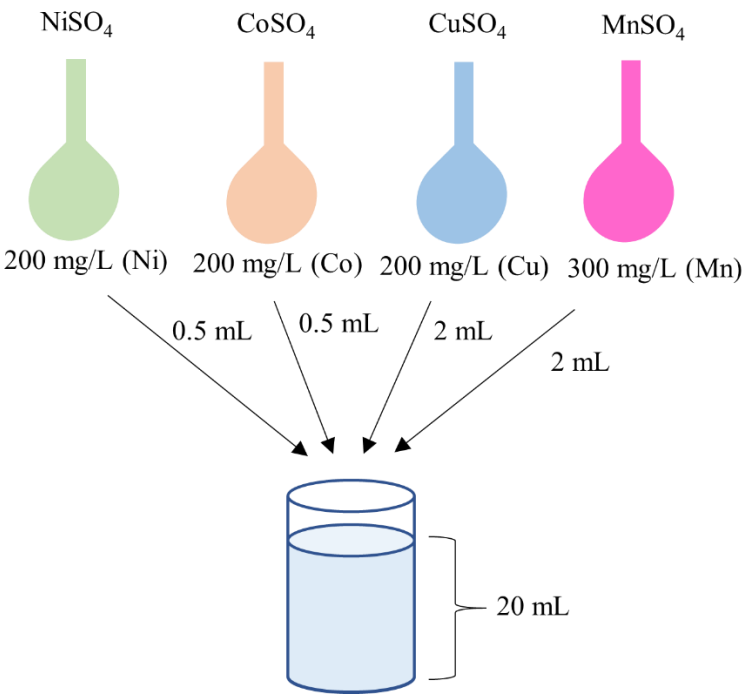

Figure 4.12: Schematic preparation of a synthetic solution of 5 mg/L Ni, 5 mg/L Co, 20 mg/L Cu, and 30 mg/L Mn.

For the remaining volume, MΩ water was added to reach 20 mL. In the case shown above, although the dilution factors of each metal were 1:40 for Ni and Co, and 1:10 for Cu and Mn, the concentrations obtained from MP-AES were calculated back with a dilution factor of 10 times for all of them. In this way, the concentrations calculated back were 50 mg/L of Ni and Co, 200 mg/L of Cu, and 300 mg/L of Mn.

As the goal was to analyse the deviation of Ni concentration measured from MP-AES with varying Co concentration, Ni (mg/L) measured from MP-AES was plotted against Ni (mg/L) from synthetic solutions prepared. A linear equation was obtained with a slope representing the factor between Ni concentration measured with MP-AES and the real Ni concentration. Ideally this factor should be equal to 1 if the measured Ni concentration was the same as the prepared in the synthetic solution. Although, experimental errors such as stock solution preparation, dilution errors, etc. could be also affecting to the correlation factor between measured MP-AES and synthetic solution prepared concentrations. Therefore, as long as the factor was smaller than 1.10 and higher than 0.80 [51] with a regression coefficient R^2 higher than 0.99, accurate MP-AES measure of Ni and Co with no interference between them was validated. For each of the three Ni concentration levels (50, 100 and 200 mg/L) there were three measured values at different Co concentrations (50, 100 and 200 mg/L). Therefore, the graph was represented with

error bars at each of the three points, which standard deviations were due to the varying Co concentration, as the other three metals were kept constant. The same procedure was done for Co, to study the deviation of measured concentration from MP-AES depending on Ni varying concentration. The error bars were calculated from the standard deviation of the three measured values for each Ni concentration level.

4.2.3 Selective Multi-Step Precipitation and Co-precipitation

The term precipitation refers to rapid crystal formation of a chemical compound, mostly under high supersaturation; while co-precipitation in this thesis refers to the parallel precipitation of multiple chemical compounds at the same time. For the precipitation of the valuable metals Ni, Co, Mn, and Li contained in the leachate, four different leachates were studied. Two of these leachates were prepared from prismatic cells non-pyrolyzed and two from prismatic cells pyrolyzed electrode powder. The four leachates studied were diluted in 1:5 ratio from initial solution to have enough sample volume for the experiments and repeats.

Due to a not complete separation of the CAM ($LiNi_XMn_YCo_{(1-X-Y)}O_2$) from the electrode foils of Al (cathode) and Cu (anode) during the pre-treatment step not studied during this project (water crushing or crushing with pyrolysis), a certain amount of these metals was present in the initial leachates. Therefore, these two metals were aimed to be removed before the CAM resynthesis. Consequently, two initial precipitation steps to remove them were necessary. As explained in section 3.1.2, Cu can be precipitated selectively with Na_2S as precipitant, while Al can be precipitated with NaOH at low pH values (pH ~ 4/5) before Ni, Co and Mn start precipitating. At first, an initial precipitation of Cu with Na_2S was performed followed by a precipitation with NaOH at pH 5. Removal of Cu after these two steps was around 80 mass%, so it was performed the other way around with a starting precipitation with NaOH to pH 5 followed by precipitation of Cu with Na_2S. In this case removal of Cu was increased to values around 98 mass% as shown in section 0. Addition of Na_2S for Cu removal slightly increased the pH of the supernatant (approximately from pH 5 to 5.5/6). After these preliminary Al and Cu precipitation experiments to stablish the order in which they should be removed, the precipitation route process flow diagram (PFD) of the different metals aimed to recover was set up for the four leachates studied as shown in Figure 4.13.

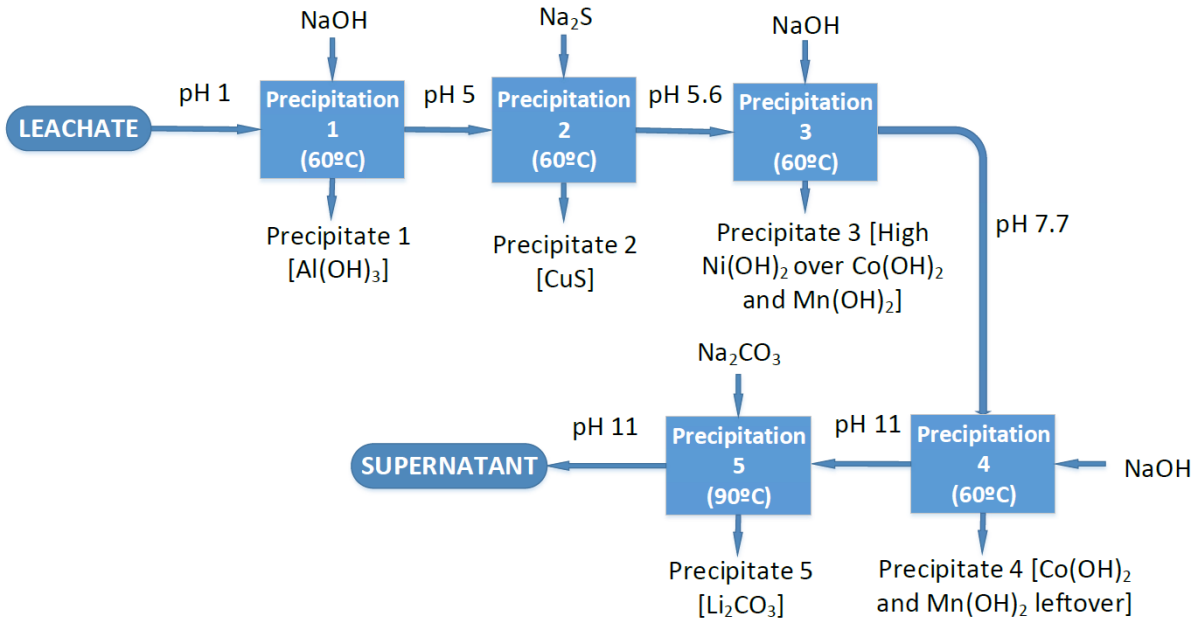

Figure 4.13: Multi-step precipitation process flow diagram.

After the two first precipitation steps for impurity removal, a 3rd precipitation with NaOH was conducted by increasing the pH of the solution from pH ~ 5.6 to pH ~ 7.7. At the pH values of leachate between 7 and 8, all Ni precipitates as $Ni(OH)_2$ as explained in section 3.1.2, while there is still Co and Mn leftover in the supernatant. This co-precipitation at pH ~ 7.7 was performed to fulfil the goal of recovering high Ni content in the resynthesized CAM. The precipitate 3 was the one further treated in the recycling process with a calcination step together with Li_2CO_3 to oxidize the metal hydroxides, expel the carbon dioxide from Li_2CO_3 and produce the $LiNi_XMn_YCo_{(1-X-Y)}O_2$. The 4th precipitation was done before the Li precipitation aiming to remove the leftover Mn and Co in the supernatant and avoid any precipitation along with Li in the last step. In addition, pH of 11 enhances the Li_2CO_3 precipitation [37]. Last precipitation step was done at 90ºC while the previous four precipitation steps were at 60ºC. This higher temperature selected was due to the decreasing solubility of Li_2CO_3 with increasing temperature as explained in section 3.1.2, which favours its precipitation. The Li concentration in the solution after the 4 precipitation steps was significantly lower than the saturation value necessary to form precipitation. Therefore, evaporation of approximately 2/3 of the volume was necessary to precipitate Li_2CO_3.

All the % values shown in this report represent mass%. They are referred as % for a matter of simplicity. The stream transferred from one precipitation step to the next is called supernatant,

and it was analysed with MP-AES to calculate metal precipitated (%) from the initial leachate (Eq. (18)) and from previous precipitation step supernatant (Eq. (19)).

$$\%Metal.Precipitated_i = \frac{C_{Me,i-1} \cdot V_{i-1} - C_{Me,i} \cdot V_i}{C_{Me,0} \cdot V_0} \% \quad (18)$$

$$\%Metal.Precipitated_{i,i-1} = \frac{C_{Me,i-1} \cdot V_{i-1} - C_{Me,i} \cdot V_i}{C_{Me,i-1} \cdot V_{i-1}} \% \quad (19)$$

This metal precipitation (%) from the supernatant before and after, as well as the initial leachate, was calculated for the three first precipitation steps. It was not calculated for the 4th step, since LiOH precipitation is not expected to happen as it has a very high solubility at 60ºC (640 g/L) [25]. The purpose of the 4th precipitation step was to remove the remaining Mn and Co present in the supernatant after the precipitation at pH 7.7. The metal precipitation (%) was also calculated from the precipitate 3 at pH 7.7 (high Ni content), after microwave digestion with concentrated HCl. Eq. (20) represents the metal precipitation from the initial leachate and Eq. (21) from supernatant after 2nd precipitation.

$$\%Metal.Precipitated_3 = \frac{m_{Me,3}}{C_{Me,0} \cdot V_0} \% \quad (20)$$

$$\%Metal.Precipitated_{3,2} = \frac{m_{Me,3}}{C_{Me,2} \cdot V_2} \% \quad (21)$$

From Eq. (21), $m_{Me,3}$ is calculated from Eq. (24) for the digested precipitate. After recovering Ni, Co, and Mn, the precipitation of Li_2CO_3 was carried out by adding an excess amount of Na_2CO_3 to the supernatant from 4th step precipitation. Precipitation 5 for the Li recovery was only performed for the P1 leachate. The precipitation process can be expressed as chemical equation (2):

$$2Li + Na_2CO_3 \rightarrow Li_2CO_3 \downarrow + 2Na^+ \quad (2)$$

The previous work in this field clearly states that the precipitation yield of Li_2CO_3 depends on the dissolved Li concentration and the pH solution (i.e., pH ~ 11 [36]). Hence, the supernatant solution was evaporated until it was 1/3 of the initial volume. In this way, Li concentration became 3 times higher. The Li concentration of the 4th precipitation supernatant was ~ 0.5 g/L, while Li_2CO_3 solubility at the corresponding temperature is 7.8 g/L [25], and Li concentration for the precipitation to start should be 1.5 g/L as shown in Table 3.1.

The Na_2CO_3:Li molar ratio selected was 1.2:1 [52]. The supernatant from 4th precipitation was kept at 90ºC for 2.5 h. Even though the volume was decreased from 240 mL to 32 mL, the Li% precipitated calculated from supernatant was 44% and calculated from the digested precipitate was 25%. The equations used to calculate these Li% precipitated were Eq. (20) and Eq. (22) respectively.

$$\%Li.Precipitated_{5,4} = \frac{m_{Me,5}}{C_{Me,4} \cdot V_4}\% \tag{22}$$

Due to the low Li concentration in the solution before the precipitation and the high solubility of Li_2CO_3, the evaporative precipitation requires a high energy consumption if Li is not spiked by adding Li_2CO_3 externally from the recycling loop. Therefore, for the last step of the recycling process, the calcination, additional Li_2CO_3 was added to the process and mixed and milled with the Ni, Co, and Mn hydroxides from 3rd precipitation. All supernatants and precipitates digested were diluted 1000 times in order to analyse them with MP-AES with a multi-element solution calibration curve reference in the range of 1-10 mg/L and blank of each metal analysed.

4.2.4 Microwave Digestion of Solid Samples

The microwave digestor (Speedwave Xpert, Berghof) was used to dissolve solid samples such as the metal precipitates and metal oxides after calcination. After the dissolution, the samples were analysed with the MP-AES. The samples were introduced in individual pressure vessels made of Polytetrafluoroethylene (PTFE) and digestion was carried out under high temperature and pressure depending on the method used. A gas collection tube is connected to all pressurized vessels in case the security rupture disc on the opening of each of them exceeds the pressure limit and explodes. This gas collection tube is connected to a ventilated fume hood so that no noxious gasses are released to the room. Therefore, it provides an effective emission control of harmful gasses. The equipment is shown below.

Figure 4.14: Microwave digestor Speedwave.

As previously mentioned, in order to analyse solid samples with MP-AES, such as the precipitates, it was necessary to dissolve them, inasmuch as it measures quantitative elemental composition from liquid samples. The samples were digested in DAP-60 vessels. During the digestion, the reaction temperature was controlled via contactless in-situ temperature sensor to ensure efficient digestion.

The sample amount varied depending on the amount of precipitate, it was between 500 and 1000 mg. The sample was weighted into a PVDF sample holder which was introduced into the vessel to avoid any loss during transferring. 10 ml HCl (37%) were added to the vessel. The mixture was carefully shaken, and the vessel was kept in the fume hood for 10 minutes for pre-reaction. The vessel was sealed with a PVDF lid and a security rupture disc. Afterwards, digestion started according to the following program.

Table 4.2: Temperature and pressure program for precipitates digestion.

Step	T (ºC)	P (bar)	Ramp (min)	Hold (min)	Power (%)
1	180	25	10	25	90
2	50	20	5	10	0

This application program is outlined for 12 samples (maximum loaded at the digestor). Minimum is 40% independent of the sample number. Power was increased by 10% per sample, when using more samples. Power was never increased to 100% to avoid rupture disc explosion [53]. When the program finished, vessels were cooled down to room temperature and open

carefully inside the fume hood. Samples were transferred into centrifuge tubes and diluted to 25 mL before the analysis. Solutions from precipitate 3 at pH 7.7 were bluish as shown in Figure 4.15, while solution from precipitate 5 after Na_2CO_3 addition was transparent.

a)  b) 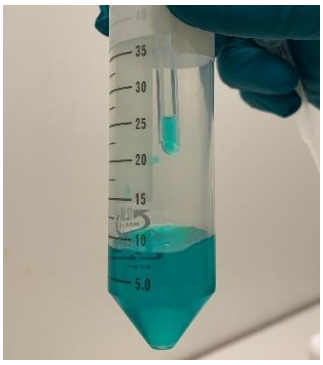

Figure 4.15: Precipitate 3 (pH = 7.7) a) before digestion, and b) dissolved after digestion.

After digestion and dilution of the sample in 25 mL, the samples were diluted 1:1000 to obtain the Ni, Co, Mn, Li, Cu, and Al concentrations into the calibration range explained in section 4.2.2 (1-10 mg/L). The way of calculating the mass% and mass of each element in the precipitate is shown in Eq. (23) and Eq. (24) respectively.

$$Me(mass\%) = \frac{C_{Me,MP-AES}\left(\frac{g}{L}\right)\cdot 0.025(L)}{m_{Precipitate}(g)} \tag{23}$$

$$m_{Me,precipitate}(g) = Me(mass\%)\cdot m_{Total}(g) \tag{24}$$

Where, in Eq. (23), $m_{Precipitate}$ is the mass of the precipitate introduced in the vessel (i.e., 0.1 g), and the $C_{Me,MP-AES}$ is the concentration of the specific element obtained from MP-AES. In Eq. (24), m_{Total} is the total mass of precipitates in the precipitation step.

4.2.5 Calcination of Precipitates

After the characterization of the precipitates 3 with high Ni content for all 4 leachates, they were mixed and milled with Li_2CO_3 at a stoichiometric ratio of Li: Me of 1.05: 1, being Me the sum of Ni, Co, and Mn. Afterwards, the calcination was carried out at the following conditions and procedure: preheating at 500ºC for 5 h, then calcined in air at 850ºC for 20 h [41]. The goal of this step was to decompose the precipitate $Ni_XCo_YMn_{(1-X-Y)}(OH)_2$ and the Li_2CO_3 into the $LiNi_XCo_YMn_{(1-X-Y)}O_2$. The chemical equation carried out is as follows.

$$Ni_X Co_Y Mn_{(1-X-Y)}(OH)_2 + \frac{1}{2} Li_2CO_3 \rightarrow LiNi_X Co_Y Mn_{(1-X-Y)}O_2 + H_2O + \frac{1}{2} CO_2 + \frac{1}{4} O_2 \quad (3)$$

After the calcination step, the oxide powder was characterized quantitatively with MP-AES and qualitatively with XRD for phase analysis.

5 Results and Discussion

In this chapter, the results from all processes carried out during this project are presented. In addition, the discussion of the obtained results is explained by relating the data obtained with the existing literature, as well as formulating the respective hypothesis.

5.1 Initial Electrode Material Composition

The initial compositions of the three types of battery electrode powder used for the leaching kinetic experiments are shown in Figure 5.1. The elemental compositions were analysed with XRF.

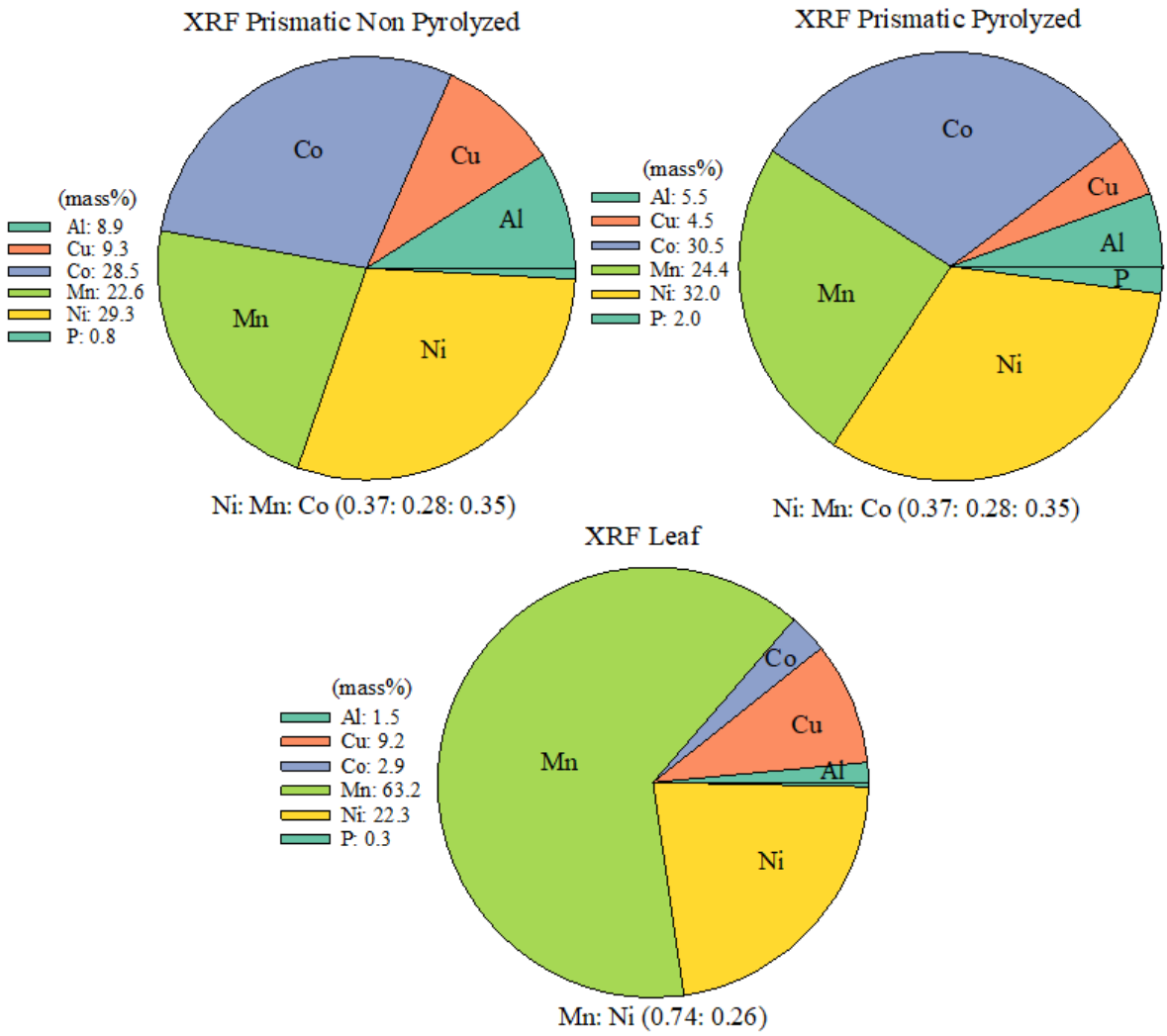

Figure 5.1: Composition of the different initial electrode powder used for leaching kinetic studies analysed with XRF.

The elemental mass% values shown above are normalized to 100%. Note that, as explained in sections 4.1.3 and 4.2.2, elements such as Li or C are not shown in the XRF spectra as explained in section. Below each pie chart it is shown the mass ratio of Ni: Mn: Co for the prismatic pyrolyzed and non-pyrolyzed powder and Mn: Ni for the leaf powder. The mass ratios of Ni, Co, and Mn for the prismatic pyrolyzed and non-pyrolyzed electrode powders are the same, but the main impurities Al and Cu are lower for the prismatic pyrolyzed than in the non-pyrolyzed. Roughly half the amount of Cu and 40% of Al was lost due to the pyrolysis in the pre-treatment step. During the pyrolysis pre-treatment the Al and Cu foils are loosen from the graphite and metal oxide which they are attached through an organic binder. Therefore, they are separated more easily [54]. For the leaf cell electrode powder, the amount of Co is very low (2.9 mass%) as it is from the type of CAM called LNMO. In addition, the mass ratio of Mn: Ni corresponds to the molar ratio of 0.75: 0.25, which matches with the molar ratio of the CAM equivalent to LNMO $LiNi_{0.5}Mn_{1.5}O_4$ shown in section 1.2.

5.2 Leaching Kinetic Studies

All leaching solutions at different reaction times were analysed with UV-Vis. The leaching experiment lasted 1 hour. Six different leaching experiments were performed to study the kinetics of three different initial powder compositions (leaf, prismatic pyrolyzed, and prismatic non-pyrolyzed cells) and two different H_2O_2 concentrations in the leaching media (3.75 and 7.5 vol.%). In Figure 5.2, 11 samples taken and filtered at the times specified in section 4.2.1 are shown for the prismatic pyrolyzed leaching. An increasing intensity of the pink colour in the leachate can be observed along with time, meaning that concentration of metals in solution is increasing (specifically $CoSO_4$ is the responsible of the pink colour [40]).

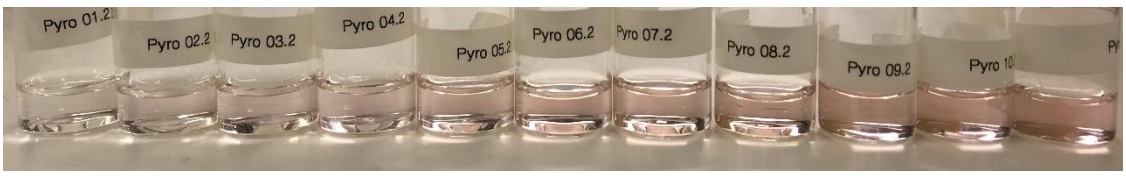

Figure 5.2: Filtered leachate samples at 1.5, 2.5, 5, 7.5, 10, 15, 20, 30, 50, and 60 minutes of reaction time from kinetic experiment.

The different absorbance values at different reaction times for the three wavelengths corresponding to Ni (392 nm), Co (512 nm), and Cu (755 nm) for all six experiments are shown in Figure 5.3.

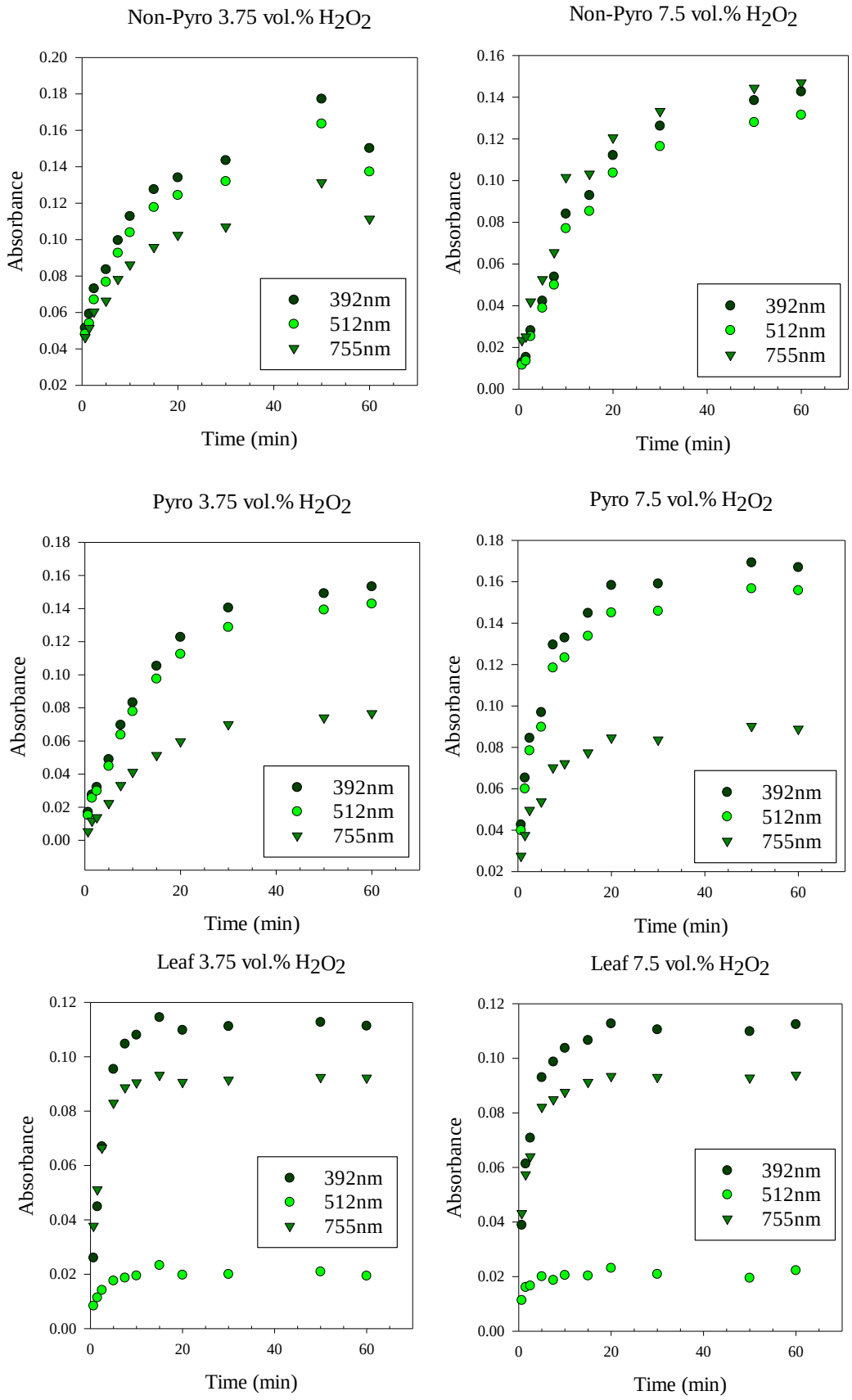

Figure 5.3: UV-Vis absorbances as a function of reaction time for the wavelengths 392 nm (Ni), 512 nm (Co), and 755 nm (Cu) for all six leaching experiments with prismatic pyrolyzed (Pyro), non-pyrolyzed (Non-Pyro), and leaf cells.

From Figure 5.3 a significant difference is observed between the leaf cell and the prismatic cells from the absorbance values corresponding to Co (512 nm). Leaf cell powder reached maximum absorbance values faster than the prismatic cell powder during leaching.

From these absorbance values, conversion was calculated following the Eq. (17) and fitted into the reaction and diffusion controlled shrinking core model (Eq. (2) and (3)). Commonly, the reaction time to fit the leaching conversion values into the kinetic model is selected by a fixed conversion value (such as 50%, and then the time is specified as "$t_{0.5}$" [55]). In this case, the conversion values selected to fit in both models were from 0 to 90% because it was aimed to include in the model high leaching efficiency values. The 90% conversion for the three metals studied was reached after 15 minutes for the prismatic non-pyro at 3.75 vol.% H_2O_2 and pyro at 7.5 vol.% H_2O_2, after 30 minutes for non-pyro 7.5 vol.% H_2O_2 and pyro 3.75 vol.% H_2O_2, after 7.5 minutes for leaf 7.5 vol.% H_2O_2, and 5 minutes for leaf 3.75 vol.% H_2O_2. According to Eq. (2) and (3), from the linear equation $y = mx$, the slope "m" corresponds to the kinetic constant k_r or k_d for the reaction and diffusion controlled models, respectively. The metal conversion values fitted into the two models of reaction and diffusion controlled kinetics for three leaching experiments are shown in Figure 5.4. The remaining three fittings are shown in the Appendix. The link to the OneDrive containing the excel sheet with the raw data of the whole spectra of UV-Vis absorbance values is also attached in the Appendix.

Reaction Controlled Non Pyrolyzed 3.75 vol% H_2O_2

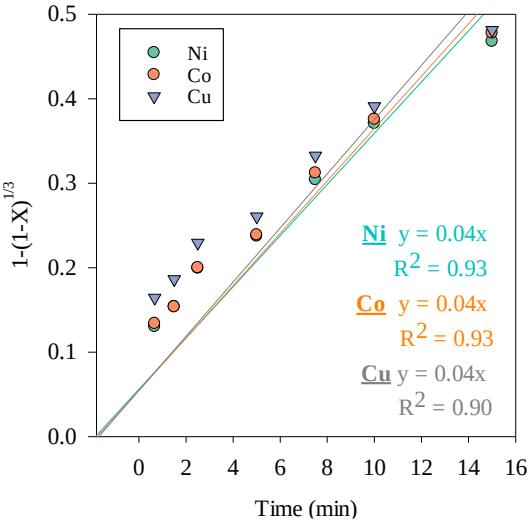

Diffusion Controlled Non Pyrolyzed 3.75 vol% H_2O_2

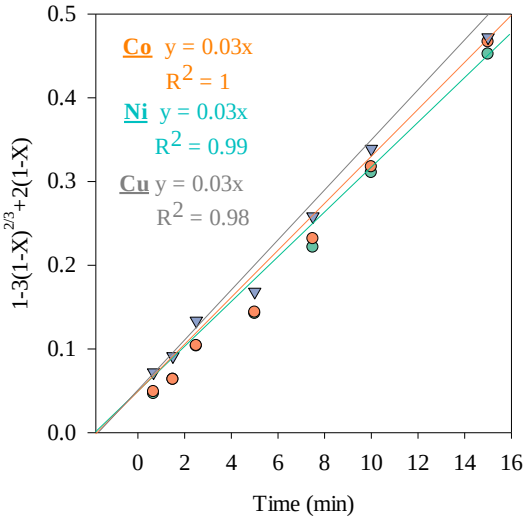

Reaction Controlled Pyrolyzed 7.5 vol% H_2O_2

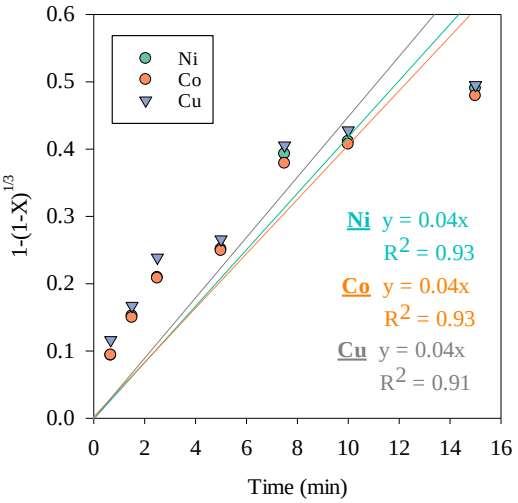

Diffusion Controlled Pyrolyzed 7.5 vol% H_2O_2

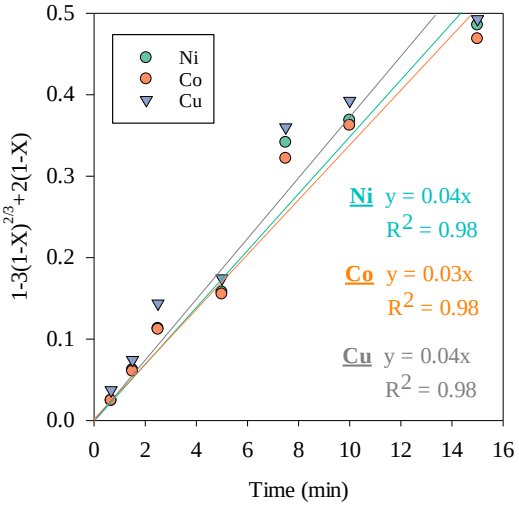

Reaction Controlled Leaf 7.5 vol% H_2O_2

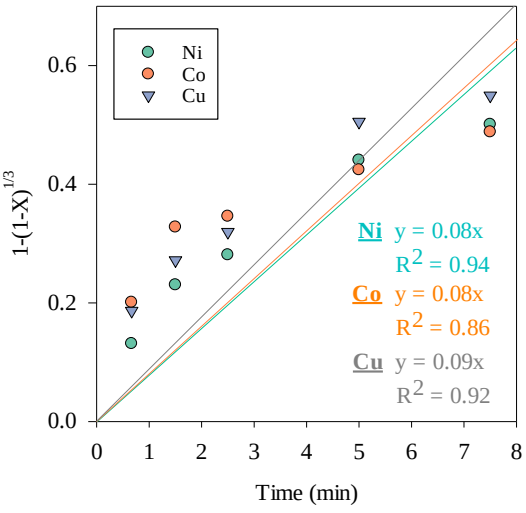

Diffusion Controlled Leaf 7.5 vol% H_2O_2

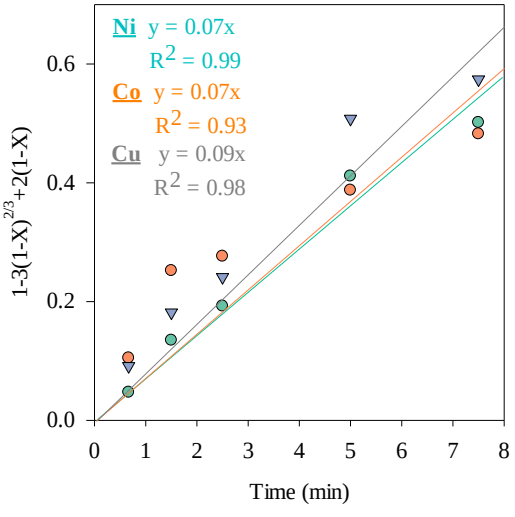

Figure 5.4: Plot of $1-(1-X)^{1/3}$ and $1-3(1-X)^{2/3}+2(1-X)$ versus time at 80ºC for Ni, Co, and Cu.

From the plots in Figure 5.4 and the ones shown in the Appendix, the kinetic constants and the regression coefficient for the three metals at all leaching experiments are shown in Table 5.1.

Table 5.1: Kinetic parameters during the leaching process calculated using the chemical reaction controlled model.

	Ni		**Co**		**Cu**	
	$k_r \times 10^3$ (min^{-1})	R^2	$k_r \times 10^3$ (min^{-1})	R^2	$k_r \times 10^3$ (min^{-1})	R^2
Non-pyro 3.75 vol.% H_2O_2	40	0.93	40	0.93	40	0.90
Pyro 3.75 vol.% H_2O_2	20	0.99	20	0.99	20	0.99
Non-pyro 7.5 vol.% H_2O_2	20	0.98	20	0.99	20	0.96
Pyro 7.5 vol.% H_2O_2	40	0.93	40	0.93	40	0.91
Leaf 3.75 vol.% H_2O_2	90	1	90	0.94	120	0.97
Leaf 7.5 vol.% H_2O_2	80	0.94	80	0.86	90	0.92

Table 5.2: Kinetic parameters during the leaching process calculated using the diffusion controlled model.

	Ni		**Co**		**Cu**	
	$k_r \times 10^3$ (min^{-1})	R^2	$k_r \times 10^3$ (min^{-1})	R^2	$k_r \times 10^3$ (min^{-1})	R^2
Non-pyro 3.75 vol.% H_2O_2	30	0.99	30	1	30	0.99
Pyro 3.75 vol.% H_2O_2	20	0.98	20	0.98	20	0.97
Non-pyro 7.5 vol.% H_2O_2	20	0.98	20	0.98	20	0.98
Pyro 7.5 vol.% H_2O_2	40	0.98	30	0.98	40	0.98
Leaf 3.75 vol.% H_2O_2	80	0.97	70	1	100	1
Leaf 7.5 vol.% H_2O_2	70	0.99	70	0.93	90	0.98

According to the R^2 values from the two models plotted, the leaching kinetics of non-pyro 3.75 vol.% H_2O_2, pyro 7.5 vol.% H_2O_2 and leaf 7.5 vol.% H_2O_2 fitted better the diffusion controlled model for all three metals, as well as Cu with the non-pyro 7.5 vol.% H_2O_2, Co and Cu with non-pyro 7.5 vol.% H_2O_2. On the contrary, the three metals in the leaching with pyro 3.75 vol.% H_2O_2, Ni and Co in the non-pyro 7.5 vol.% H_2O_2, and Ni in the leaf 3.75 vol.% H_2O_2 fitted better the reaction controlled model. Despite these metals fitted better the reaction controlled leaching model, their R^2 coefficients were close to their diffusion controlled R^2 values. The highest difference in the R^2 coefficient for the kinetics that fitted better the reaction controlled model, was observed for the Ni in the leaf leaching at 3.75 vol.% H_2O_2, where a value of 1 was attained for the reaction controlled model in comparison to a value of 0.97 for the diffusion controlled model. Summarizing, 2/3 of all the metal leaching experiments fitted better the diffusion controlled model, and the other 1/3 had R^2 values very close between both models. The better fitting of the diffusion controlled model in most of the leaching experiments, agrees with the insignificant effect of temperature on the leaching process when the temperature is in

the range from 60 to 80ºC [37], like in the leaching experiments performed in this project (80ºC). This correlates well with the leaching kinetics performed in literature explained in section 3.1.1 and with the temperature independent region shown in Figure 3.2. According to this previous study on leaching kinetics of LIBs electrode material, it was found that two distinctive stages exist for the leaching rate against temperature in the range of 30 to 80ºC. From 60 to 80ºC, the values for k_r (reaction rate constant) are nearly identical regardless of the increase of temperature. Leaching at temperatures higher than 60ºC is not temperature sensitive. Consequently, the chemical reaction does not control the kinetics of the leaching. In the diffusion controlled model, kinetics depends on the concentration gradient between bulk and particle surface, stirring rate and geometry of the particles [38].

After the study of the leaching kinetics, the selection of the pH for the selective co-precipitation of Ni over Co and Mn was performed with a synthetic solution that simulated the battery leachate metal concentrations. This study was already performed in previous work to this master thesis though [48]. Therefore, the results about this precipitation experiments are presented in the Appendix. According to the previous work and this synthetic solution precipitation, the optimal pH needed to precipitate 100% Ni and approximately 65% of Mn and Co, was 7.7. In these precipitation experiments, the precipitates were analysed with XRF. As explained in Section 4.1.3, XRF as a quantitative characterization technique for the precipitates and supernatant of battery solutions represents some disadvantages. Consequently, for the quantitative analysis of the supernatant and precipitates of the multi-step precipitation, the MP-AES was used for this project.

5.3 MP-AES Validation Method

In Table 5.3 the concentration values for Ni, Co, Mn, and Cu measured from MP-AES and the concentrations prepared from the respective synthetic solutions are shown. As mentioned in section 4.2.2 the Mn and Cu concentrations were kept constant for all 9 synthetic solutions. Thus, in Table 5.3, the average values for all the 9 MP-AES measured values of Mn and Cu, the standard deviation (SD), as well as the relative standard deviation (RSD (%)) are shown. RSD is computed as the SD divided by the average. In chemical analysis, when dealing with ppm (mg/L) or higher concentrations, an RSD (%) value of 5% or lower is acceptable [56].

Table 5.3: Ni, Co, Cu, and Mn concentrations measured with MP-AES and actual concentrations in 9 prepared synthetic solutions.

N.º	Ni MP-AES (mg/L)	Ni Synt. Sol. (mg/L)	Co MP-AES (mg/L)	Co Synt. Sol. (mg/L)	Cu MP-AES (mg/L)	Cu Synt. Sol. (mg/L)	Mn MP-AES (mg/L)	Mn Synt. Sol. (mg/L)
1	51.66	49.9	49.5	49.6	190.78	199.1	299.46	298.8
2	104.23	99.8	50.34	49.6	194.15	199.1	303.08	298.8
3	51.60	49.9	99.53	99.3	192.42	199.1	302.37	298.8
4	104.71	99.8	99.83	99.3	193.33	199.1	303.55	298.8
5	210.04	199.5	102.15	99.3	193.98	199.1	308.62	298.8
6	209.02	199.5	203.02	198.5	192.45	199.1	308.25	298.8
7	105.51	99.8	205.35	198.5	194.16	199.1	310.81	298.8
8	51.02	49.9	203.58	198.5	193.74	199.1	304.46	298.8
9	215.87	199.5	52.28	49.6	200.66	199.1	317.2	298.8
SD					2.74		5.38	
Avg.					193.96		306.42	
RSD (%)					1.41		1.76	

In Table 5.4 the Ni and Co concentration average and standard deviation measured from MP-AES are shown for a same concentration level (50, 100, and 200 mg/L). In this way, it can be analysed if Co, at different concentrations, is significantly affecting the measurement of Ni at a same concentration, and vice versa. This was done due to the possible interference between the Ni and Co atom lines analysed with the MP-AES (352.454 and 340.512 respectively) as explained in section 4.2.2.

Table 5.4: Ni and Co concentrations measured with MP-AES and from prepared synthetic solutions.

N.º	Ni MP-AES (mg/L)	Ni Synt. Sol. (mg/L)	N.º	Co MP-AES (mg/L)	Co Synt. Sol. (mg/L)
1	51.66	49.875	**1**	49.5	49.625
3	51.6	49.875	**2**	50.34	49.625
8	51.02	49.875	**9**	52.28	49.625
SD	0.35			1.43	
Avg.	51.43			50.71	
RSD (%)	0.68			2.82	
2	104.23	99.75	**3**	99.53	99.25
4	104.71	99.75	**4**	99.83	99.25
7	105.51	99.75	**5**	102.15	99.25
SD	0.65			1.43	
Avg.	104.82			100.50	
RSD (%)	0.62			1.42	
5	210.04	199.5	**6**	203.02	198.5
6	209.02	199.5	**7**	205.35	198.5
9	215.87	199.5	**8**	203.58	198.5
SD	3.70			1.22	
Avg.	211.64			203.98	
RSD (%)	1.75			0.60	

For all three metal concentrations (50, 100, and 200 mg/L) the RSD (%) values are lower than 5%, meaning that the Ni concentration measured from MP-AES does not deviate when Co concentration varies, and vice versa. This low deviation between the measurements also reflects that the measurement is reproducible and precise. The concentration measured with MP-AES versus true metal concentration (conventional true value, the best estimate of the true value because we can never determine the true value) in the synthetic solution of the two metals is plotted in Figure 5.5 with errors bars corresponding to the ± SD to evaluate the accuracy of the measurement.

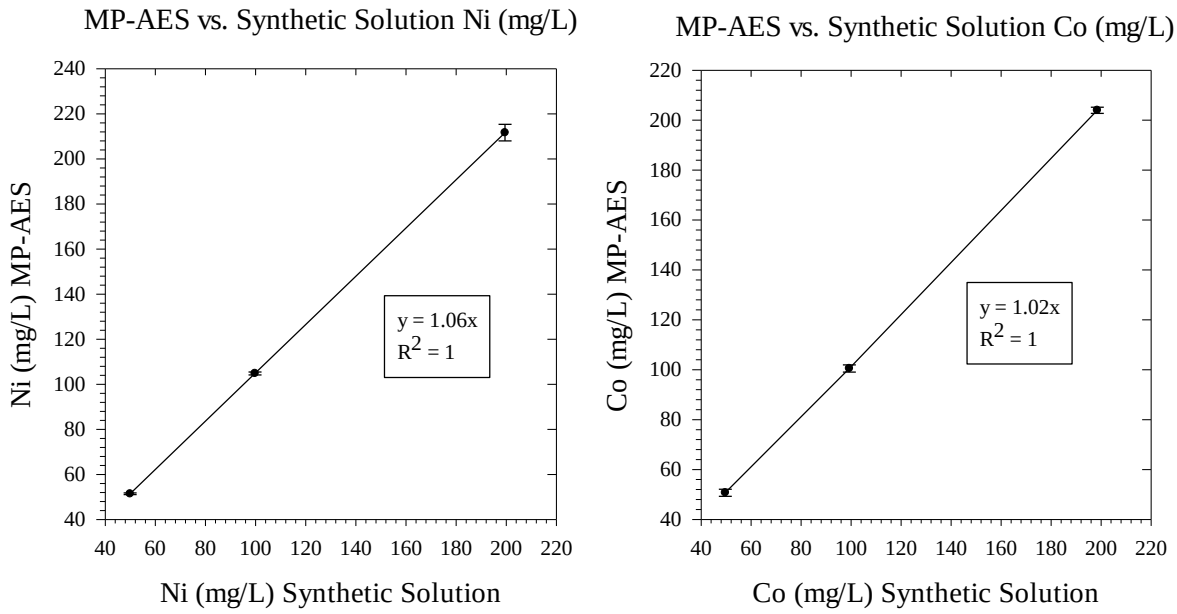

Figure 5.5: Ni and Co measured concentrations with MP-AES vs. actual concentration in the synthetic solution.

The correlation factor between Ni measured with MP-AES and actual concentration in solution is 1.06 and 1.02 for Co. This means that Ni value measured with MP-AES is 6% higher than the actual value, while for Co it is 2% higher. These values are within the acceptable range of accuracy when the analyte level is in the order of 10 ppm as it is in the current study (5, 10, and 20 mg/L since the solutions were 10 times diluted as explained in section 4.2.2). This acceptable recovery range is 80 - 110 % for analytical method validation [57]. Moreover, both Ni and Co correlations between MP-AES measured and true concentration in solution, perfectly fit a linear equation with a R^2 equals to 1. In the case of Cu and Mn, since their concentrations were constant for all synthetic solutions, the correlation factor was calculated as the average for the 9 synthetic solutions measurements divided by the actual value. Mn correlation factor is 1.03, or 3% higher, and Cu is 0.97, or 3% lower.

From this validation method of the MP-AES, it can be concluded that neither Ni nor Co measurement is affected by the presence of the other analyte in the sample. Furthermore, the parameters used to analyse the precision (RSD (%)) and accuracy of the measurements (correlation factor between measured and true value) for Ni, Co, Mn, and Cu are lower than 5 and 10% respectively, and are between the acceptable limits for the method validation.

5.4 Selective Multi-Step Precipitation of Leachates

In this chapter the percentage of recovery of the target metals Ni, Co, Mn, and Li, as well as the removal of Cu and Al from the initial leachates are presented. The multi-step precipitation route is shown in Figure 4.13:. Besides the quantitative analysis of the process streams from MP-AES, qualitative analysis such as XRD identification of the different compounds present in the precipitates is shown.

Four different leachates were used as starting material, 2 from prismatic pyrolyzed electrode powder, and 2 from prismatic non-pyrolyzed. The initial composition of the four leachates is shown in Table 5.5. For the sake of readability, the different leachates are named as NP1, NP2, P1, and P2, referring NP to non-pyrolyzed and P to pyrolyzed.

Table 5.5: Initial composition of the leachate solutions analysed with MP-AES.

	Li (mg/L)	Al (mg/L)	Mn (mg/L)	Co (mg/L)	Ni (mg/L)	Cu (mg/L)
NP1	765.47	43.96	1770.46	2223.18	2247.30	549.10
NP2	489.97	22.39	1169.54	1423.70	1436.39	309.17
P1	1040.30	122.05	2353.82	3013.51	3069.18	326.45
P2	960.71	114.78	2196.45	2830.44	2857.20	314.75

The main difference between the compositions of the 4 leachates is the Al concentration, which is significantly lower for the NP than the P. Furthermore, the leachate NP2 has significantly lower concentrations of Li, Ni, Co, Mn than the other three (approximately half than P1 and P2, and 1.5 lower than NP1). This is because the leaching of NP2 was performed with a S/L ratio of 70g/L of electrode powder while the other three were performed at 120 g/L. Therefore, the amount of active metal oxide $LiNi_XMn_YCo_{(1-X-Y)}O_2$ that could be leached in NP2 was 1.7 times

lower than for NP1. In the following sections, the PFD shown in Figure 4.13 is divided step by step with the precipitation (%) for each of the metal targeted to precipitate.

5.4.1 Al and Cu Removal

- **Precipitation 1**

1st precipitation step is the Al removal from the leachate with increasing the pH from 1 to pH of 5.

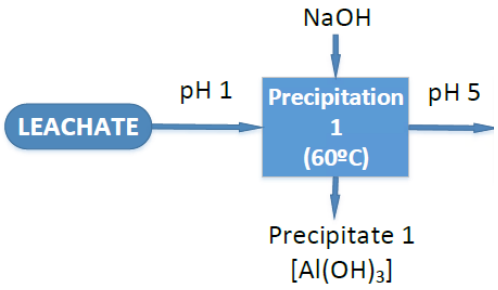

Figure 5.6: Al removal (Precipitation 1).

From this precipitation, the Al precipitation (%), as well as the rest of the metals, were calculated with Eq. (12) and they are shown below.

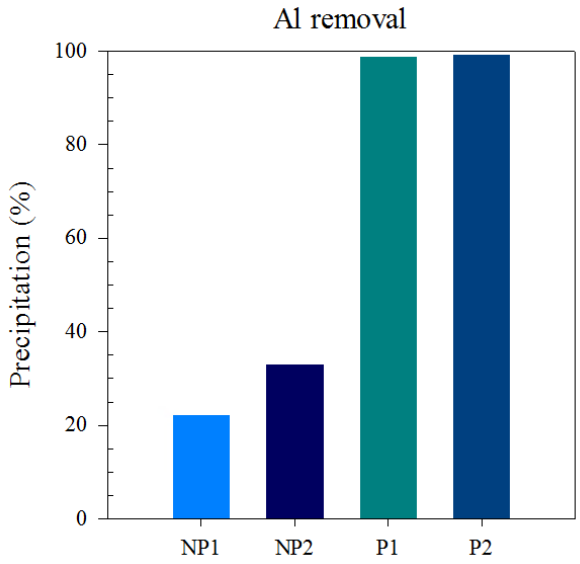

Figure 5.7: Al precipitation (%) for NP1, NP2, P1, and P2 in 1st step precipitation.

From the graph bar shown above the difference in Al % precipitated during the 1st precipitation step is appreciable. 22 and 33% of Al precipitated from NP1 and NP2 respectively while for P1

and P2 it was 99% in both cases. The low precipitation (%) of Al for the NP leachates when increasing the pH to 5 (5.13, 5.11, 4.87, and 5.03 for NP1, NP2, P1, and P2 respectively) may be due to the low Al concentration in the initial leachate (~ 30 mg/L) compared to the P leachates (~ 120 mg/L). This low initial Al concentration corresponds to a lower initial supersaturation in the system with respect to $Al(OH)_3$. The solubility product (K_{sp}) of $Al(OH)_3$ defines the amount of Al that will be present in the solution after the precipitation regardless initial composition, once the supersaturation exceeds 1. Then, it is obvious that the amount (%) precipitated of Al will be higher when initial concentrations are higher, since the end point is the same, as long as the solution is supersaturated ($S \geq 1$). Despite this, the end point of Al concentration was not the same for the leachates with higher initial concentration of Al than the ones with lower, although the final pH values were very similar (~ 5). Al concentration in the supernatant after precipitation was 28, 11, 1, and 1 mg/L for NP1, NP2, P1, and P2, respectively. As explained in Eq. (6), the supersaturation of a species is the responsible for the precipitation when it is higher than 1. In particular, the IAP is the driving force that affects the supersaturation. Therefore, if the IAP of $Al(OH)_3$ ($IAP = (C_{Al3+})(C_{OH-})^3$) is not equal or higher than the K_{sp}, precipitation does not occur spontaneously. Nonetheless, as shown in section 2.2.1, there can be spontaneous precipitation in the metastable zone, where supersaturation is within the supersolubility and solubility limits, meaning that supersaturation is equal or slightly higher than 1. To prove this lower Al precipitation driving force of the NP solutions compared to the P solutions, the P1 was diluted 4 times in order to have a similar Al concentration to the NP. Then, Al precipitation decreased from 99% to 12% when initial concentration was diluted to 24 mg/L and pH increased to 5.5. Following, it is shown the rest of the metal's precipitation (%) in this 1st step.

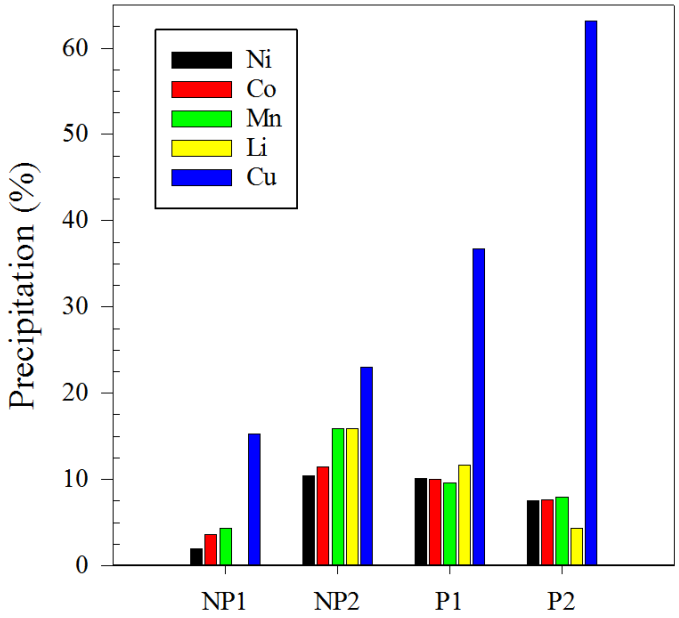

Figure 5.8: Cu, Ni, Co, Mn, and Li precipitation (%) for NP1, NP2, P1, and P2 in the 1st step precipitation.

It is considerable that Cu precipitation (%) has higher values than the rest of the metals at pH of 5 [40], especially in P2. Cu precipitated for NP1, NP2, P1, and P2 was 15, 23, 37, and 63% respectively. On the other hand, 8 ± 4% of Ni precipitated as average between the 4 leachates. In the case of Co and Mn, the average % lost during this step was 8 ± 3% and 9 ± 5%, respectively. Each metal has a large precipitation (%) SD between the 4 solutions. This large deviation could be due to the small number of samples or replicates (4) and initial compositions slightly different between them. The supernatant from this step was transferred to the 2nd step which is Cu removal with Na_2S.

- **Precipitation 2**

The Cu precipitated (%) is shown below for the four different leachates after the 1st step. 50 mL of 0.03M Na_2S were used in all 4 precipitations.

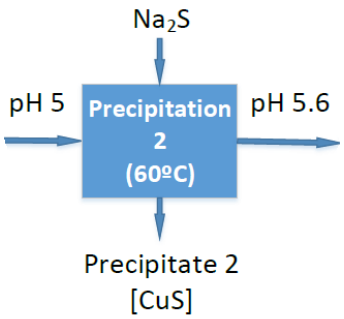

Figure 5.9: Cu removal (precipitation 2).

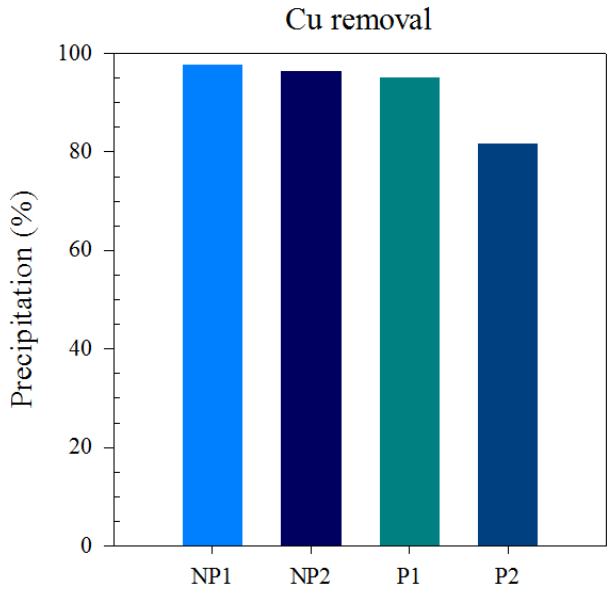

Figure 5.10: Cu precipitation (%) for NP1, NP2, P1, and P2 in 2nd step precipitation.

Cu was selectively removed using Na_2S as precipitant. 98, 96, 95, and 82% of Cu precipitated from supernatant of 1st precipitation for NP1, NP2, P1 and P2, respectively. This corresponds with the reported information in literature [58]. Although in that previous research the concentration of other metals (Co, Li, Ni, and Mn) remained constant. Nevertheless, in the data reported, precipitation was at pH 1, without previous addition of NaOH. In this project, the 1st precipitation step was carried out with NaOH because, as explained in section 4.2.3, Cu removal was significantly increased at pH 5 over pH 1 (78% Cu was removed when 1st precipitation step was with Na_2S at pH 1 for NP1, instead of 98% when it was the 2nd step at pH 5). Overall Cu precipitated after these two initial steps was 98, 97, 97, and 94%. After the addition of Na_2S, the pH increased to 5.64, 7.05, 5.43, and 6.78 for NP1, NP2, P1, and P2, respectively. The reason for the higher pH-increase for the NP2 compared to the other leachates, is due to its lower concentration of metals (Table 5.5*:*), although the amount of Na2S was kept the same (50 mL of Na_2S 0.03 M). Consequently, an excess of Na_2S was added. which contributed to the increase in pH instead of reacting with Cu^{2+}. This increase of the pH to a value of 7 represented a higher amount of Ni and Co lost in the precipitate as shown in Figure 5.11.

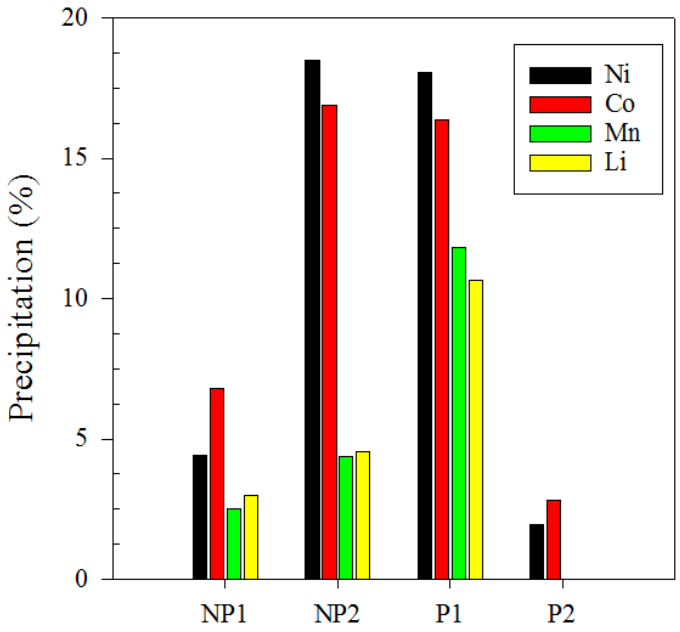

Figure 5.11: Ni, Co, Mn, and Li precipitation (%) for NP1, NP2, P1, and P2 in 2nd step precipitation.

There is a big variation between the Ni, Co, Mn, and Li loss in the 4 leachates during the 2nd step. The biggest difference is between the P2 and the other three solutions. In the case of the P2, there was no precipitation for Mn and Li, while for P1 they precipitated 12 and 11%, respectively. The average amount of Ni and Co lost during this 2nd step was 11 ± 9% and 11 ± 7%, respectively. In the case of Mn and Li, SD of the precipitation (%) between samples was even higher than the average. Thus, separate values for NP1, NP2, P1, and P2 were 3, 4, 12, and 0%, respectively for Mn, and 3, 5, 11, and 0%, respectively for Li. This significantly different precipitation values may be due to the small sample of experiments (4 samples, but 2 of each type of battery powder), the different final pH value due to different initial concentration of metals. Furthermore, ungoverned parameters such as reaction time (time that it takes for the solution to reach the target pH) and cooling time after the target pH was reached, could have affected the metal precipitation (%) of the four samples. An initial high temperature solution and limited cooling time induced some evaporation as the supernatant was transferred from the reactor to the filtration unit. Individual differences in cooling time among the samples are regarded as likely. This could affect the metal concentration in the supernatant and provoke further precipitation [36]. Total Ni lost after these 2 initial precipitation steps was 11, 31, 30%, and 14% for NP1, NP2, P1, and P2, respectively.

5.4.2 Precipitation of Hydroxides with High Ni Content

- **Precipitation 3**

After the Al and Cu removal, the supernatant was transferred to the 3rd precipitation step where a precipitate with high Ni content over Co and Mn was targeted. Precipitant used was NaOH and the final pH was 7.7.

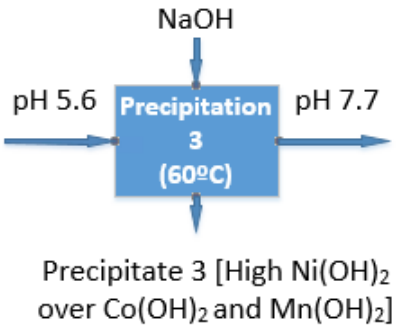

Figure 5.12: High Ni precipitation (Precipitation 3).

The Ni, Co, Li, and Mn precipitated (%) during this step was calculated both from the supernatant and from the digested precipitates with MP-AES. First, the metal precipitation (%) values calculated from supernatant (pH 7.7) are shown and compared between the 4 different leachates. Following, the metal precipitated (%) calculated from precipitate 3 is shown and compared to the previous in order to validate the calculations from the two different outputs of the process.

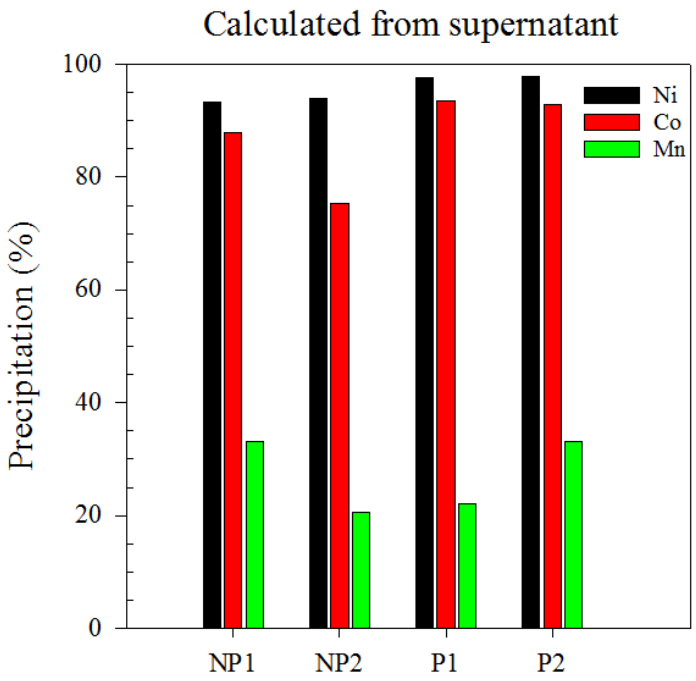

Figure 5.13: Ni, Co, and Mn precipitation (%) in 3rd step precipitation calculated from supernatant composition.

From the Ni, Co, and Mn precipitation (%) shown above for all solutions used, average of 96 ± 2% of Ni precipitated during this 3rd step. On the other hand, 87 ± 8% of Co, and 27 ± 7% of Mn precipitated as well. This metal amount precipitated, added up to the other 2 previous steps made up a total precipitation of 98 ± 1% of Ni, 91 ± 5% of Co, and 43 ± 1% of Mn from the initial leachates. These numbers validated the selective precipitation of Ni over Co and specially Mn at pH values of 7.7 - 7.8 [40] due to the lower solubility product of $Ni(OH)_2$ salt ($K_S = 10^{-15.22}$ at 25ºC) compared to $Co(OH)_2$ ($K_S = 10^{-14.89}$ at 25ºC) and $Mn(OH)_2$ ($K_S = 10^{-12.7}$ at 25ºC) [59]. SD for the 3rd step precipitation of Ni, Co, and Mn between the 4 samples is quite lower than the previous 2 steps. It is ≤ 10% different for Ni and Co with respect to their average (2 and 10% respectively), while it is 25% for Mn. Despite the amount of Li precipitated during this step, the values were quite different for the four solutions, which were 16, 0, 1, and 16% for NP1, NP2, P1, and P2, respectively.

Following, the three metals of interest % precipitation values are shown, which have been calculated from the precipitate in order to validate the values previously discussed from the other output stream of the process.

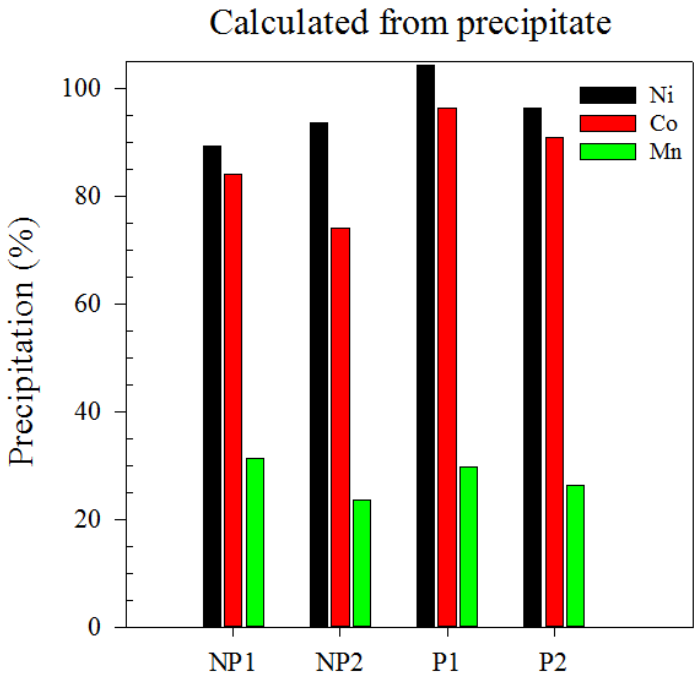

Figure 5.14: Ni, Co, and Mn precipitation (%) in 3rd step precipitation calculated from precipitate composition.

96 ± 6% of Ni, 86 ± 10% of Co, and 28 ± 4% of Mn precipitated in the 3rd step according to precipitates and inlet solution composition at pH ~ 5.6 (5.6, 7.05, 5.43, and 6.78 for NP1, NP2, P1, and P2, respectively). These values corresponded to a relative difference between the precipitation (%) calculated from supernatant of 0, 1, and 2% for Ni, Co, and Mn, respectively. Relative difference between both calculations is ≤ 2% which proved the accuracy of the precipitation values measured for Ni, Co, and Mn, as well as the reliability of calculating them from both precipitates and supernatant. The relative difference was calculated for each metal as shown in Eq. (25).

$$\left| Rel.difference(\%) = \frac{Avg\%\,precipitation\_Supernatant - Avg\%\,precipitation\_Precipitate}{Avg\%\,precipitation\_Supernatant}\% \right| \quad (25)$$

Despite Ni precipitation for P1 was 104%, this is within the acceptable error limit (%) of 80 - 110 for an analyte level within the concentration range of 10^{-1} to 10 ppm [57]. Samples analysed were diluted by a factor of 1000, so the Ni level was between 10^{-1} and 10 ppm, specifically $3 \cdot 10^{-1}$ ppm in the precipitate digested and $1 \cdot 10^{-1}$ ppm in the inlet solution of pH 5.43 for the P1 precipitation 3.

The compositions of the precipitates from this 3rd step are shown below as mass% of the total mass precipitated.

Table 5.6: Metal composition (mass%) of precipitate 3 from NP1, NP2, P1, and P2 leachates.

	Li (mass%)	Al (mass%)	Mn (mass%)	Co (mass%)	Ni (mass%)	Cu (mass%)
NP1	0.4	0.0	3.0	9.8	11.0	0.0
NP2	0.2	0.0	3.8	13.2	16.7	0.2
P1	0.3	0.0	3.9	15.1	16.3	0.2
P2	0.4	0.1	3.3	13.9	15.0	0.1

The Ni compositions shown above for the precipitate 3, corresponded to a 75, 62, 70, and 79% of the initial Ni composition in the leachates of NP1, NP2, P1, and P2, respectively. Despite the losses during the previous 2 steps, the total Ni recovery average was still high, which was 72 ± 7%. The total amount of precipitate 3 for NP1, NP2, P1, and P2 were 2.3156, 0.8024, 1.9802, and 2.2622 g, respectively. The precipitate 3 from NP1 was characterized for phase identification of the metal hydroxides by XRD using the database ICDD-PDF. The XRD analysis shows the presence of Na_2SO_4 and $LiNaSO_4$ in the precipitate. Besides, $Ni(OH)_2$ and NiS are also present among the most crystalline phases and characteristic peaks. $Ni(OH)_2$ matches its three major peaks with Na_2SO_4 at 19º, 38.5º, and 59.5º values of 2θ. The XRD pattern is shown below.

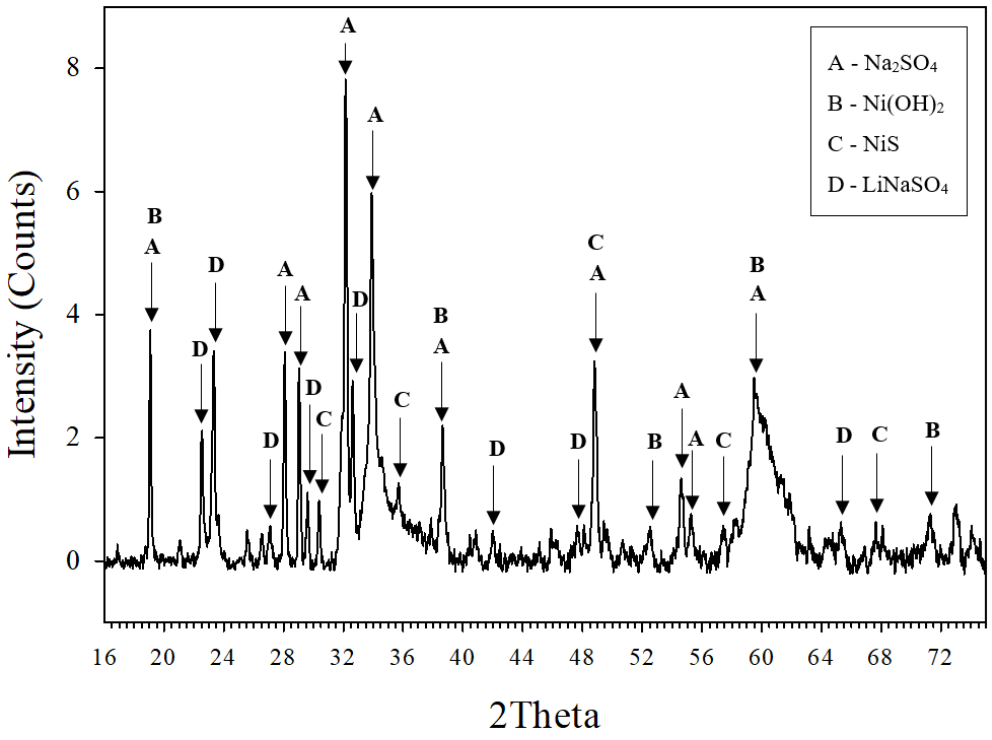

Figure 5.15: XRD pattern of the NP1 precipitate 3 along with the identified phases.

As highlighted before, from the XRD pattern, Na_2SO_4 and $LiNaSO_4$ were identified present in the precipitate 3. The $LiNaSO_4$ in the precipitate justifies the loss of Li during the initial 2 steps in the presence of Na^+ and SO_4^{2-} in the solution, as shown in section 5.4.1. The digested precipitate sample was analysed again with MP-AES, but now including Na in the matrix sample to quantify it. Concentration of Na in the precipitate represented a 9.6 mass%. This corresponded with 222 mg of Na in the precipitate. According to this, Na composition was very close to Co and Ni in the precipitate (9.8 and 11.0 mass%, respectively), which is very high. As explained in section 4.2.1, the leaching was performed in 2 M H_2SO_4, although the leachates were 5 times diluted. Therefore, the SO_4^{2-} concentration in the initial leachates was 0.4 M. From precipitation 1 and 3, a total of 63 mL of 1.3 M NaOH were added, which corresponded to 0.08 moles of Na. Na_2SO_4 exhibits retrograde solubility (same as Li_2CO_3), which means that solubility decreases with temperature. However, it still has a very high solubility at 60ºC, 309 mg/L. [25]. Such a high concentration of Na_2SO_4 was not reached at any precipitation step. The highest concentration that could have been reached after the addition of 63 mL of NaOH and 50 mL of Na_2S was 29.02 g/L. This is assuming that all Na was in the sulphate form, and it is still 10 times lower than Na_2SO_4 solubility at 60ºC. One of the possible factors affecting the presence of the impurity Na in the precipitate is the crystal or precipitate growth rate. All

precipitates contain impurities to some extent with elements coming from the precipitation solution. The contamination can be in the form of surface adsorption, lattice entrapment of foreign ions or molecules, inclusion (physical entrapment) of solvent, etc. As reported in [60], the precipitation of $NiSO_4 \cdot 6H_2O$ from its aqueous solution by cooling crystallization in the presence of Na^+, Cl^- and Mg^{2+}, showed that Na^+ and Cl^- ions were adsorbed in the crystal surface. Furthermore, the concentration of impurities increased significantly for most of the ions when the growth rate was faster (5 - 7 mm/day in contrast to 1 - 5 mm/day of crystal growth), except for the halogens Cl and F. During the 3rd step precipitation (and all precipitation steps carried out), the process occurred at a very rapid rate. It lasted approximately 20 minutes since the NaOH was added until the precipitates in solution were filtered. This was because the precipitant agent was added relatively fast. In order to prove if the Na was adsorbed in the precipitate surface, the precipitate 3 from NP1 was thoroughly washed with 100 mL of MΩ water, filtered, digested and analysed with MP-AES. As shown below, the content of Na was satisfactorily decreased. Consequently, Ni, Co, and Mn mass% increased.

Table 5.7: Precipitate 3 composition (mass%) for NP1 before and after washing step with MΩ water.

	Li (mass%)	Mn (mass%)	Co (mass%)	Ni (mass%)	Na (mass%)
NP1 before washing	0.4	3.0	9.8	11.0	9.6
NP1 after washing	0.1	4.5	17.5	19.8	1.6

Apart from Na, Li mass% was also reduced. It decreased from 0.4 to 0.1% in the precipitate 3 after the washing step. This is due to the reason that most of the Li precipitated in the form of $LiNaSO_4$ as depicted in the XRD pattern in Figure 5.16. Mn, Co, and Ni mass% increased after washing due to the decrease of total precipitate mass from the Na_2SO_4 and $LiNaSO_4$ removal. The washing step was only performed for the leachate NP1. Overall, the Na mass% in the precipitate 3 of NP2, P1, and P2 was 5.9, 5.0, and 6.9%, respectively.

5.4.3 Precipitation of Lithium Carbonate

- **Precipitation 4 and 5**

After the precipitation of high Ni content over Co and Mn in the form of hydroxides, two more precipitation steps were performed to recover Li as Li_2CO_3 from the supernatant. This

precipitation was only performed for the P1 leachate because the precipitation recovery of Li (%) was not high enough due to the high solubility of Li_2CO_3 and low concentration of Li in the solution before these precipitation steps.

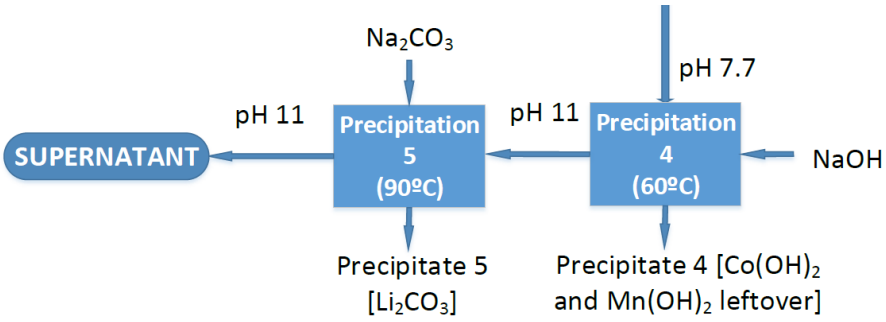

Figure 5.16: Li_2CO_3 precipitation (Precipitation 4 and 5).

As previously mentioned, solubility of Li_2CO_3 decreases with increasing temperature. This is the contrary than for most of the salts which solubility increases with increasing temperature. At 90ºC Li_2CO_3 has a solubility of 0.78 mass% [25], or 7.8 g/L. This solubility of 7.8 g/L of Li_2CO_3 corresponds to 1.48 g/L of Li needed in the solution to get supersaturated and trigger the precipitation. The leaching solution required to be concentrated with respect to Li before, because the concentration of Li was approximately 3 times lower than the expected to meet the solubility limit (0.486 g/L of Li in the supernatant after precipitation 4). Therefore, the precipitation was carried out at 90ºC to evaporate the solution until the final volume was 1/3 of the initial, and thus concentrate the Li from 0.486 g/L to 1.458 g/L (value closer to supersaturation of 1.48 g/L of Li). Nonetheless, the initial solutions were 5 times diluted from the real leachates as it has been reported previously in the report. Hence, with the real leachate, Li concentration after the 3rd precipitation step should be in the order of 5 times higher, meeting the concentration required to be supersaturated with respect to the Li_2CO_3.

During precipitation 4, the pH was increased up to ~ 11.5. The supernatant after this step was analysed with MP-AES. Concentrations of Ni, Co, and Mn were 0 g/L for all of them, while 486 mg/L of Li. Then Na_2CO_3 was added and the supernatant was heated up to 90ºC for 2 hours until the volume decreased from 210 mL to 70 mL (1/3 of the initial volume). The amount of Na_2CO_3 added was accordingly to a molar ratio of Na_2CO_3: Li^+ of 1.2: 1 [52]. Li composition of both supernatant at pH 11.5 after precipitation 5, and in the digested precipitate 5 were analysed to be compared. Precipitation (%) of Li is shown below calculated from Eq. (19) for the supernatant and Eq. (22) for the precipitate. The mass of Li present in the precipitate is also

shown calculated from both output streams of the process. Total mass of precipitate was 1.1012 g.

Table 5.8: Li precipitation (%) and mass (mg) in the P1 precipitate 5 calculated from supernatant and digested precipitate.

	Calculated from supernatant	Calculated from precipitate
Li precipitation (%)	41	27
Li precipitated (mg)	47	30

Although the values shown above are significantly different depending on whether they were calculated from the supernatant or the precipitate 5 (Relative difference of 36%), the Li precipitated (%) was relatively low. This Li recovery (%) was a bit lower compared with the 60% recovered in literature [40]. The reason of this difference could be due to the lower concentration of Li in the initial leachates used (5 times diluted from real leachates) compared to the ones used in literature which were not diluted before the precipitation steps. For example, in the study [61], a pre-treated Li_2SO_4 solution with a Li concentration of 20 g/L was used, while the Li concentration before performing the Li_2CO_3 precipitation in this project was 0.486 g/L. The large deviation between the amount of Li precipitated depending on whether calculated from supernatant or precipitate could be due to the low first ionization energy for Li explained in section 4.2.2. At 5,000 K, Li can be ionized and not be detected by its atom line. Additionally, Na and Li have close ionization energies which could lead to misinterpretation of both concentration analyses [51], and Na was present in the solution in high concentrations while the precipitation happened (~ 8 g/L of Na). Another reason for this big deviation between both calculations could be due to the low amount of the analyte which in this case would be the Li present in the sample. Li concentration in the precipitate and supernatant samples analysed with MP-AES were lower than 1 mg/L. Therefore, the standard deviation between the measures increases for the calibration curve used of 1 – 10 mg/L. Due to these disadvantages the precipitation of Li from the supernatant after precipitation 3 was only performed for one solution out of the four from which the multi-step precipitation route was carried out. In future work, the Li recovery may be studied more deeply, from real leachates without dilution. Also other parameters which can improve the Li recovery yield should be studied, such as application

of ultrasounds [61]. To supress ionization of Li and Na from the sample analysed with MP-AES, addition of caesium to the sample is commonly used as $CsNO_3$ to control the matrix by absorbing excess energy in the plasma and improve quantification [51].

5.4.4 Overall Precipitation Recycling Route

The P1 leachate multi-step precipitation route is shown here as an example of the whole precipitation route, with the composition of all streams. The precipitation (%) for the metals of interest are also plotted against the pH of the different precipitation steps. All the supernatants compositions normalized and metal mass (mg) in the precipitates are calculated from the supernatant concentrations and volumes from Eq. (26) and (27).

$$\%Me(normalized) = \frac{C_{Me}}{\sum_{k=Li,Mn,Ni,Co,Al,Cu} C_{Me,k}}\% \tag{26}$$

$$m(precipitate)_{Me,i} = C_{Me,i-1} \cdot V_{i-1} - C_{Me,i} \cdot V_i \tag{27}$$

Being $C_{Me,i-1}$ the concentration of the metal in the supernatant before the precipitation state *i*, V_{i-1} the volume of the supernatant corresponding to precipitate step *i-1*, $C_{Me,\mathrm{i}}$ and V_i the concentration of the metal and the volume of the supernatant the precipitation step *i*. For the precipitation 3, the metal masses in the precipitate were also calculated from the digested precipitates with Eq. (24).

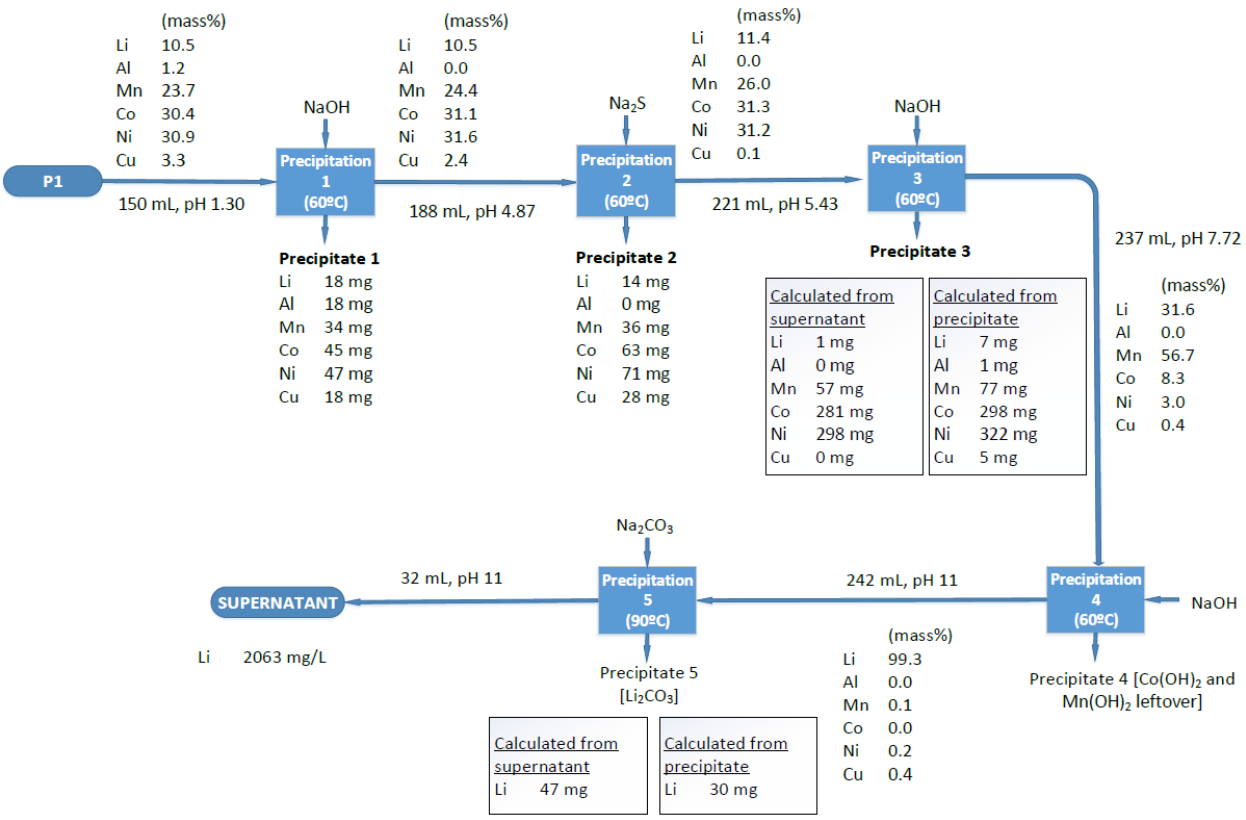

Figure 5.17: Multi-step precipitation route for P1 leachate.

At the precipitation 1, the Al mass% in solution was reduced from 1.2 to 0.0%, corresponding to a 100% precipitation. Nevertheless, roughly 10% of Ni, Co, and Mn, respectively, were lost. After precipitation 1 and 2, Cu mass% was reduced from 3.3 to 0.1% in solution, which corresponds to a 97% removal. Although in this 2nd precipitation an additional 18, 16, and 11% of Ni, Co, and Mn, respectively, were lost. Metal mass calculated from supernatant and from precipitate has a relative difference of 26% in the case of Mn, while 6 and 7% for Co and Ni, respectively. Nonetheless, the normalized mass% for Ni, Co, and Mn in the precipitate calculated from supernatant were 46.2, 43.3, and 10.5%, respectively, and 46.2, 42.8, and 11.0%, respectively if calculated from the precipitate. These normalized values represent a relative difference between the two calculations much lower, 0.0, 1.2, and 4.8% for Ni, Co, and Mn, respectively. After the 3rd precipitation step Ni decreased from 31.2 to 3.0% in the solution. The composition in the precipitate 3 calculated from the precipitate corresponds to a Ni: Co: Mn molar ratio of 0.5: 0.4: 0.1 or also named NCM 541. This NCM molar ratio is not among the different CAM types shown in Table 1.1, although it is close to the NCM 532 and 442.

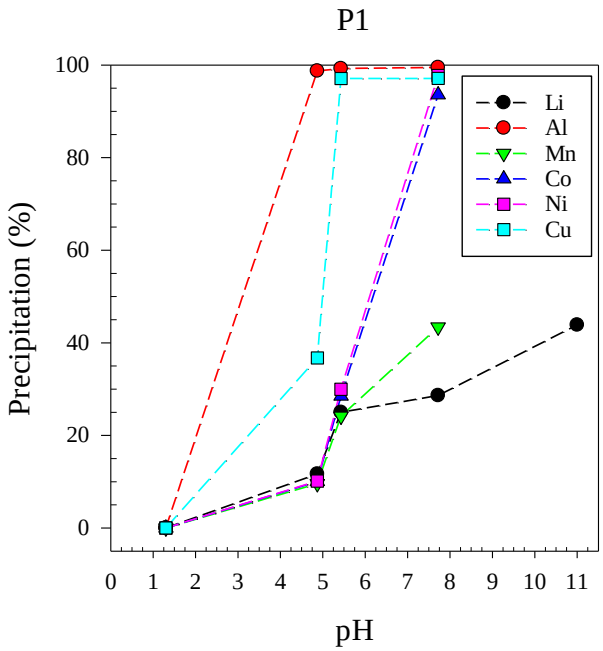

Figure 5.18: Precipitation (%) of Li, Al, Mn, Co, Ni, and Cu versus pH for the multi-step precipitation route of P1.

The metal precipitation (%) values shown above were calculated with Eq. (18) from the composition of the supernatant at each step compared to the initial leachate composition. Furthermore, precipitate 3 from the 4 different leachates were calcined to decompose the hydroxides and lithium carbonate and generate the $LiNi_XCo_YMn_{(1-X-Y)}O_2$.

5.5 Calcination of Metal Precipitates

The four precipitates from the 3rd step were calcined at the conditions explained in section 4.2.5. The different metals' mass% were compared to the values before the calcination. Pictures of the metal hydroxides before and the metal oxides after the calcination process are shown below.

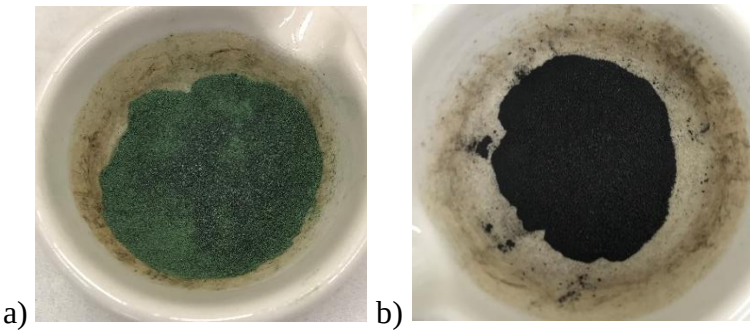

Figure 5.19: Precipitate 3 a) before calcination (metal hydroxide), and b) after calcination (metal oxide).

The composition in mass% of the precipitates calcined are shown in Table 5.9 including the Na. Na content was still high in the calcined samples because the washing step of the precipitate was not performed before the calcination.

Table 5.9: Calcined precipitates 3 composition analysed after digestion with MP-AES.

	Li (mass%)	Al (mass%)	Mn (mass%)	Co (mass%)	Ni (mass%)	Cu (mass%)	Na (mass%)
NP1	4.9	0.1	3.5	11.9	13.4	0.0	10.1
NP2	3.1	0.1	6.0	19.9	24.9	0.0	4.9
P1	3.7	0.2	4.8	18.8	20.1	0.0	6.7
P2	4.1	0.00	3.6	15.8	17.0	0.1	7.1

The normalized Ni: Co: Mn mass ratios before and after calcination are shown below as the average of the four samples.

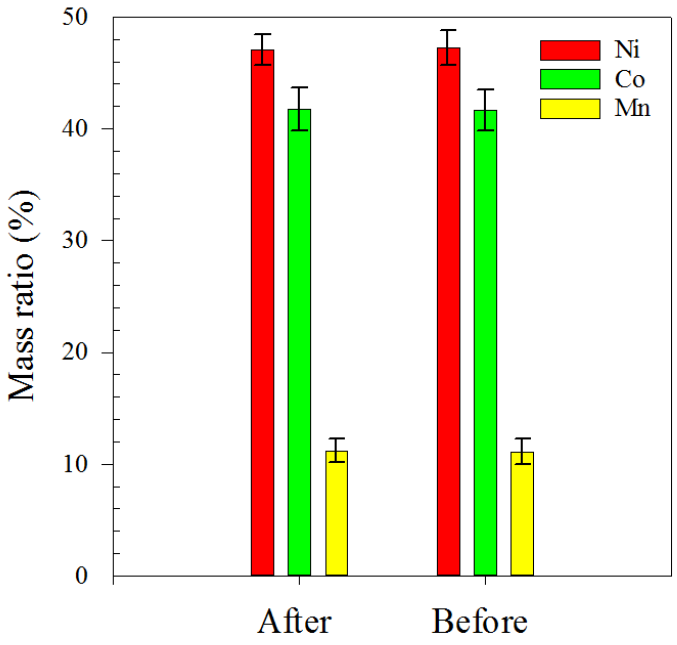

Figure 5.20: Ni, Co, and Mn mass ratios (%) of the precipitate 3 before and after calcination.

The average values shown above are consistently close enough to state that the Ni: Co: Mn mass ratio did not vary throughout the calcination process. The values before and after calcination were respectively 47 ± 2% and 47 ± 1% for Ni, 42 ± 2% and 42 ± 2% for Co, 11 ± 1% and 11 ± 1% for Mn. The total mass of precipitate before and after calcination was measured for P2. The mass before calcination was 1.1765 g while after calcination it decreased to 0.9860 g. However, the mass of Ni, Co and Mn did not decrease significantly. From 176 to 168 mg for Ni, 163 to 155 mg for Co, and 39 to 35 mg of Mn. These differences are < 5% for Ni and Co and 10% for Mn, which are very low. They could be due to the balance variation of the measure.

The calcined samples for P1 and NP1 were characterized using XRD for phase analysis. The XRD patterns are shown below.

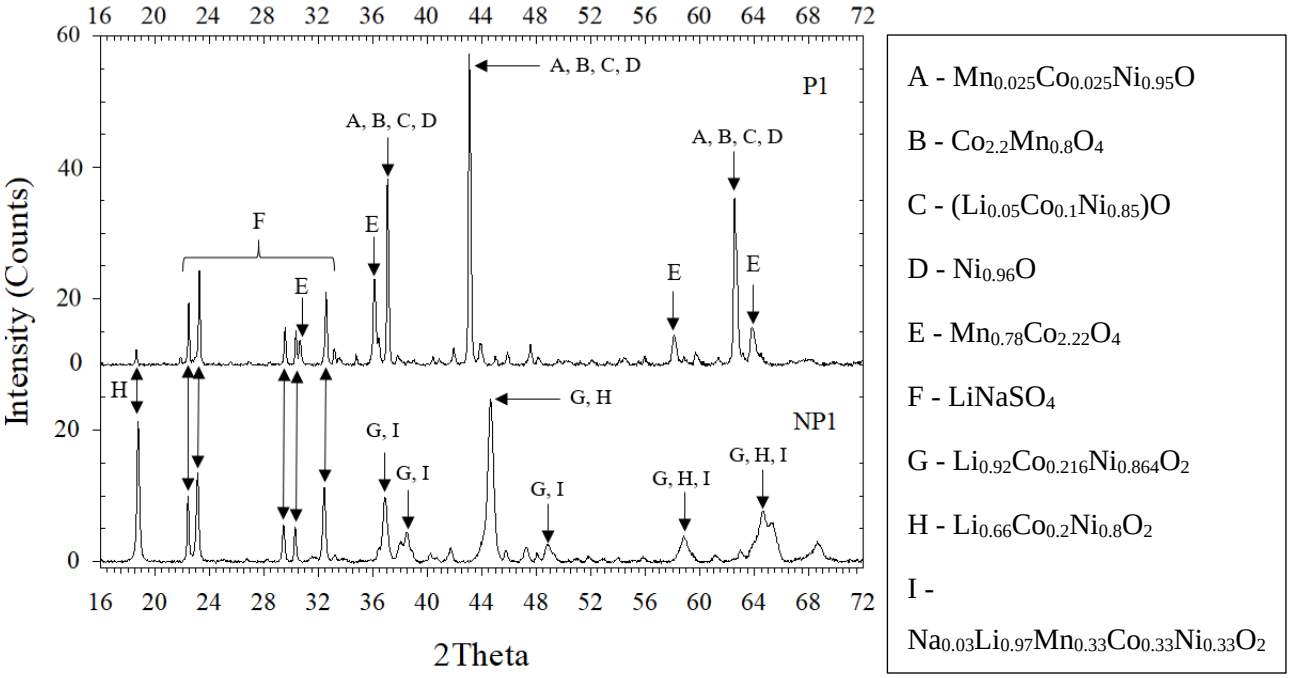

Figure 5.21: XRD pattern for NP1 and P1 precipitate 3 after calcination.

Since the precipitates were not washed before the calcination, some Na was incorporated in the mixture of metal oxides as $Na_{0.03}Li_{0.97}Mn_{0.33}Co_{0.33}Ni_{0.33}O_2$ in the NP1. It is also evident the common peaks corresponding to $LiNaSO_4$ in both calcined samples. It was still present in the calcined powder because the washing step was not performed in the precipitate hydroxide. $LiNaSO_4$ peaks correspond with the ones shown in Figure 5.16 at the 2θ values of 22.5, 23.5, 29.5, 31.0, and 32.5º. Apart from this, it is also distinctive that the peaks in P1 are thinner than in NP1, meaning that crystallinity of the calcined sample P1 was higher than in NP1. For the

NP1 pattern, the main peaks match with the mixture of metal oxides $Li_{0.92}Co_{0.216}Ni_{0.864}O_2$, $Li_{0.66}Co_{0.2}Ni_{0.8}O_2$, and $Na_{0.03}Li_{0.97}Mn_{0.33}Co_{0.33}Ni_{0.33}O_2$. On the other hand, the peaks from P1 sample match better with $Mn_{0.025}Co_{0.025}Ni_{0.95}O$, $Co_{2.2}Mn_{0.8}O_4$ (with a mixture of Co^{2+} and Co^{3+}), $(Li_{0.05}Co_{0.1}Ni_{0.85})O$, $Ni_{0.96}O$, and $Mn_{0.78}Co_{2.22}O_4$. The main difference between the metal oxides from NP1 and P1 is the ratio of Li against Ni, Co, and Mn. It is very low for the oxides in the P1 compared with NP1. The reason for this difference is that the amount of Li_2CO_3 added to the precipitates NP1 and P1 before the calcination was swapped between each other by mistake. Therefore, instead of having a Li: Me (being Me the sum of Ni, Co, and Mn) molar ratio of 1.05, the molar ratios for NP1 and P1 were 1.75 and 0.63. For the other two metal oxides from NP2 and P2 the Li: Me molar ratios were 0.91 and 0.95, respectively. This Li: Me molar ratio was calculated for the calcined samples as well and they were 1.43 and 0.72 for NP1 and P1, respectively. The Ni: Co: Mn molar ratios (%) for the four metal oxide samples are shown below.

Table 5.10: Ni, Co, Mn molar ratio (%) for NP1, NP2, P1, and P2 metal oxides.

	Ni (%)	Co (%)	Mn (%)
NP1	46.5	41.1	12.4
NP2	49.0	39.1	11.9
P1	45.9	43.0	11.1
P2	46.8	43.2	10.0

These molar ratios correspond to an average of 47.1 ± 1.4% of Ni, 41.6 ± 1.9% of Co, and 11.3 ± 1.0% of Mn in the four metal oxides. Therefore, it has been possible to resynthesize the CAM with the chemical formula of $LiNi_{0.47}Mn_{0.11}Co_{0.42}O_2$ with the multi-step precipitation recycling route proposed.

6 Conclusions

In this project, different LIB electrodes from EVs have been leached to study the kinetic mechanism and rate of recovery of the valuable metals. With the conditions selected, it was proved that the majority of the metal leaching experiments were controlled by the product layer diffusion model. The few metals that fitted better the reaction controlled mechanism shown a regression coefficient (R^2) very close to the diffusion controlled, making not a big difference. The fact that the leaching experiments followed the diffusion controlled model was because the temperature selected was 80ºC, and as reported in literature, at this temperature the reaction kinetics does not depend on the temperature. Additionally, all metals had reached the maximum leaching efficiency after 1 hour.

After the leaching of the valuable metals present in the battery electrodes, a multi-step precipitation was performed for 4 leachates with different metal concentrations. In the two first precipitation steps Al and Cu coming from the electrode foil collectors were separated. It was proved that Al concentration was too low in 2 out of the 4 leachates to be efficiently removed, since the driving force was not high enough to precipitate the Al selectively. Cu was satisfactorily removed using a Na_2S as precipitant. Nevertheless, the amount of Ni, Co, and Mn precipitated after these two first steps was significantly high in the 4 leachates, varying from 12% for NP1 to 30% for NP2 and P1 of Ni lost. The deviation between the 4 leachates in these two first steps was very high due to the difference in the final pH values. After the 3rd precipitation step, a 96% of Ni, 86% of Co, and 27% of Mn were precipitated as average between the 4 leachates. In this 3rd step the deviation between the 4 samples was much lower. Furthermore, these metal recoveries were calculated from both the supernatant solution after precipitation, as well as from the solid precipitates. Both calculations of the metal precipitated (%) had very low relative difference between them (< 2.5%). Therefore, it was achieved the goal of recovering a high Ni content over Co and Mn precursor to resynthesize the CAM.

After the precipitation, a calcination step was performed to convert the metal hydroxide into cathode active metal oxide of the formula $LiNi_{0.47}Mn_{0.11}Co_{0.42}O_2$. Despite, high content of Na was present in the resynthesized metal oxide since the washing step after precipitation was not performed. Notwithstanding, it was proved that Na was adsorbed in the precipitate surface and could easily be removed with a washing step.

Apart from the resynthesis of the CAM with high Ni content, a validation method for the MP-AES as a characterization technique for solutions containing Ni, Co, Mn, and Cu was

performed. The goal was proving that the possible interference between Ni and Co atom lines analysed in the equipment was not affecting the results and that the measurements were accurate and precise. The validation method was satisfactorily carried out with very low deviation between the measures, reflecting that the measurement is reproducible and precise, as well as with acceptable range of accuracy between measurements and actual values of Ni, Co, Mn, and Cu in the sample within a range from 5 to 20 mg/L.

7 Future Work

To improve the metal recovery yield performed, accuracy and reliability of the results, some future work could be further performed in this recycling route:

- As explained, Cu and Al in the leachate come from the current collector foils of the electrodes, these foils are supposed to be completely separated during the pre-treatment step of crushing and sorting, which was out of the scope of this project. Improving the separation efficiency in this pre-treatment step would reduce the following precipitation steps to remove them from the leaching solution, and therefore decrease the Ni, Co, and Mn loss during these steps.
- In order to increase selectivity to Al precipitation in the 1st precipitation step, the 1st precipitate containing mostly Al, could be redissolved and recirculated into the inlet stream to this 1st step. This would increase the concentration of Al and thus, the driving force responsible of its precipitation. The flow diagram would look like:

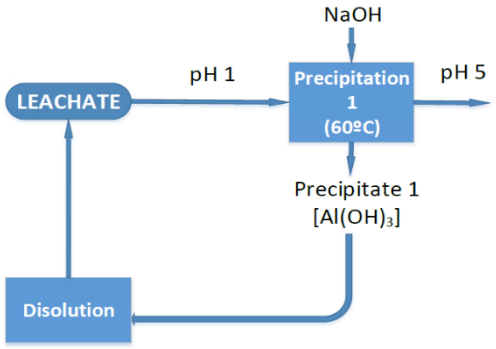

Figure 7.1: Recirculation of 1st precipitate.

- Include a washing step after the 3rd precipitation step to remove the Na present in the precipitate.
- Study the leaching kinetics of the other metals not studied here (Mn, Li, and Al) with MP-AES. The leaching kinetics studied here were performed just for Ni, Co, and Cu because they showed a peak in UV-Vis, but since the MP-AES was validated and established as a new, easy, and fast characterization technique, it could be used to study the kinetics of all the metals present in the CAM.
- Study the possible ionization of Li in the sample during the MP-AES analysis explained in section 4.2.2 that could lead to misinterpretations of the Li measurements by addition of caesium to the sample as $CsNO_3$ to control the matrix by absorbing excess energy in the plasma and improve quantification [51].

8 Bibliography

[1] P. Liu, L. Xiao, Y. Tang, Y. Zhu, H. Chen, and Y. Chen, "Resynthesis and electrochemical performance of LiNi0.5Co0.2Mn0.3O2 from spent cathode material of lithium-ion batteries," *Vacuum*, vol. 156, no. August, pp. 317–324, 2018, doi: 10.1016/j.vacuum.2018.08.002.

[2] Z. Shahan, "CleanTechnica," *69% of Autos Sold in Norway in 2020 Have a Plug*, 2020. https://cleantechnica.com/2020/07/09/69-of-autos-sold-in-norway-in-2020-have-a-plug/#:~:text=Norway continues to be a,auto sales%2C another global record.

[3] T. Watari, B. C. McLellan, S. Ogata, and T. Tezuka, "Analysis of potential for critical metal resource constraints in the international energy agency's long-term low-carbon energy scenarios," *Minerals*, vol. 8, no. 4, 2018, doi: 10.3390/min8040156.

[4] "Metal prices." https://www.metalary.com/.

[5] David Merriman, "Roskill. Raw materials for new mobility: Outlook, trends, scenarios," 2019, p. 19.

[6] X. Zhang *et al.*, "Toward sustainable and systematic recycling of spent rechargeable batteries," *Chem. Soc. Rev.*, vol. 47, no. 19, pp. 7239–7302, 2018, doi: 10.1039/c8cs00297e.

[7] C. Herrmann and S. Kara, *Recycling of Lithium-Ion Batteries*. 2018.

[8] I. Mancini, M. (University of Camerino, Camerino, "Improved Anodic Materials for Lithium-ion Batteries: Surface Modification by Metal Deposition and Electrochemical Characterization of Oxidized Graphite and Titanium Dioxide Electrodes," University of Camerino, Camerino, 2008.

[9] V. Marano, S. Onori, Y. Guezennec, G. Rizzoni, and N. Madella, "Lithium-ion batteries life estimation for plug-in hybrid electric vehicles," *5th IEEE Veh. Power Propuls. Conf. VPPC '09*, pp. 536–543, 2009, doi: 10.1109/VPPC.2009.5289803.

[10] G. S. Hauke Engel, Patrick Hertzke, "Second-life EV batteries: The newest value pool in energy storage," 2019, [Online]. Available: https://www.mckinsey.com/industries/automotive-and-assembly/our-insights/second-life-ev-batteries-the-newest-value-pool-in-energy-storage.

[11] T. Georgi-Maschler, B. Friedrich, R. Weyhe, H. Heegn, and M. Rutz, "Development of a recycling process for Li-ion batteries," *J. Power Sources*, vol. 207, pp. 173–182, 2012,

doi: 10.1016/j.jpowsour.2012.01.152.

[12] J. Diekmann *et al.*, "Ecological Recycling of Lithium-Ion Batteries from Electric Vehicles with Focus on Mechanical Processes," *J. Electrochem. Soc.*, vol. 164, no. 1, pp. A6184–A6191, 2017, doi: 10.1149/2.0271701jes.

[13] "REGULATION OF THE EUROPEAN PARLIAMENT AND OF THE COUNCIL concerning batteries and waste batteries, repealing Directive 2006/66/EC and amending Regulation (EU) No 2019/1020," Brussels, 2020.

[14] M. Wentker, M. Greenwood, and J. Leker, "A bottom-up approach to lithium-ion battery cost modeling with a focus on cathode active materials," *Energies*, vol. 12, no. 3, pp. 1–18, 2019, doi: 10.3390/en12030504.

[15] F. Meng, Q. Liu, R. Kim, J. Wang, G. Liu, and A. Ghahreman, "Selective recovery of valuable metals from industrial waste lithium-ion batteries using citric acid under reductive conditions: Leaching optimization and kinetic analysis," *Hydrometallurgy*, vol. 191, no. October 2019, p. 105160, 2020, doi: 10.1016/j.hydromet.2019.105160.

[16] P. Q. H.A. van der Sleet, L. Heasman, *Harmonization of Leaching/Extraction tests*, 70th ed. Elsevier, 1997.

[17] T. Havlík, *Hydrometallurgy. Principles and application*, CRC Press. Cambridge International Science Publishing Limited in assotiation with Woodhead Publishing Limited.

[18] L. An and P. Methods, *Recycling of Spent Lithium-Ion Batteries*. 2019.

[19] T. R. M. P. Meshram, B.D. Pandey, "Recovery of valuable metals from cathodic active material of spent lithium ion batteries: leaching and kinetic aspects.," *Waste Manag.*, pp. 306–313, 2015.

[20] J. W. H. S.G. Zhu, W.Z. He, G.M. Li, X. Zhou, X.J. Zhang, "Recovery of Co and Li from spent lithium-ion batteires by combinationmethod of acid leaching and chemical precipitation.," *Trans. Nonferrous Met. Soc. China 22*, pp. 2274–2281, 2012.

[21] G. C.J., *Transport Processes and Separation Process Principles (Include Unit Operations)*, 4th ed. Univeristy of Minnesota, 2003.

[22] L. An, *Recycling of Spent Lithium-Ion Batteries*. 2019.

[23] N. Othusitse and E. Muzenda, "Predictive Models of Leaching Processes: A Critical Review," pp. 136–141, 2015, doi: 10.15242/iie.e1115039.

[24] A. S. . Myerson, *Handbook of Industrial Crystallization, Elsevier Science & Technology, 2001*. 2001.

[25] H. W. (Ed.), *CRC Handbook of Chemistry and Physics*, 91th ed. 2010.

[26] R. Lewis, W. Evans, R. Lewis, and W. Evans, "Solutions and Solubility," *Chemistry (Easton).*, pp. 173–193, 2018, doi: 10.1057/978-1-137-61037-9_11.

[27] P. H. Karpinski and J. S. Wey, *Handbook of industrial crystallization - Chapter 6 Precipitation processes*, no. 2001. 2019.

[28] H. Zou, E. Gratz, D. Apelian, and Y. Wang, "A novel method to recycle mixed cathode materials for lithium ion batteries," *Green Chem.*, vol. 15, no. 5, pp. 1183–1191, 2013, doi: 10.1039/c3gc40182k.

[29] J. F. Blais, Z. Djedidi, R. B. Cheikh, R. D. Tyagi, and G. Mercier, "Metals precipitation from effluents: Review," *Pract. Period. Hazardous, Toxic, Radioact. Waste Manag.*, vol. 12, no. 3, pp. 135–149, 2008, doi: 10.1061/(ASCE)1090-025X(2008)12:3(135).

[30] Y. Yang, S. Xu, and Y. He, "Lithium recycling and cathode material regeneration from acid leach liquor of spent lithium-ion battery via facile co-extraction and co-precipitation processes," *Waste Manag.*, vol. 64, pp. 219–227, 2017, doi: 10.1016/j.wasman.2017.03.018.

[31] H. Kitao, T. Fujihara, K. Takeda, N. Nakanishi, and T. Nohma, "High-temperature storage performance of Li-ion batteries using a mixture of Li-Mn spinel and Li-Ni-Co-Mn oxide as a positive electrode material," *Electrochem. Solid-State Lett.*, vol. 8, no. 2, pp. 86–90, 2005, doi: 10.1149/1.1843792.

[32] P. Baláž *et al.*, "Hallmarks of mechanochemistry: From nanoparticles to technology," *Chem. Soc. Rev.*, vol. 42, no. 18, pp. 7571–7637, 2013, doi: 10.1039/c3cs35468g.

[33] Q. Zhang, J. Lu, F. Saito, C. Nagata, and Y. Ito, "Room temperature acid extraction of Co from LiCo0.2Ni0.8O2 scrap by a mechanochemical treatment," *Adv. Powder Technol.*, vol. 11, no. 3, pp. 353–359, 2000, doi: 10.1163/156855200750172222.

[34] D. C. R. Espinosa, A. M. Bernardes, and J. A. S. Tenório, "An overview on the current processes for the recycling of batteries," *J. Power Sources*, vol. 135, no. 1–2, pp. 311–319, 2004, doi: 10.1016/j.jpowsour.2004.03.083.

[35] J. S. Swain, B., Jeong, J., Lee, J. C., Lee, G. H., & Sohn, "Hydrometallurgical process for recovery of cobalt from waste cathodic active material generated during

manufacturing of lithium ion batteries.," *Power Sources, 167(2), 536-544.*, 2007.

[36] P. Meshram, B. D. Pandey, and T. R. Mankhand, "Hydrometallurgical processing of spent lithium ion batteries (LIBs) in the presence of a reducing agent with emphasis on kinetics of leaching," *Chem. Eng. J.*, vol. 281, pp. 418–427, 2015, doi: 10.1016/j.cej.2015.06.071.

[37] W. Gao *et al.*, "Lithium Carbonate Recovery from Cathode Scrap of Spent Lithium-Ion Battery: A Closed-Loop Process," *Environ. Sci. Technol.*, vol. 51, no. 3, pp. 1662–1669, 2017, doi: 10.1021/acs.est.6b03320.

[38] NTNU, "Kinetics of Reactions in Hydrometallurgy." 2019.

[39] Y. Yao, M. Zhu, Z. Zhao, B. Tong, Y. Fan, and Z. Hua, "Hydrometallurgical Processes for Recycling Spent Lithium-Ion Batteries: A Critical Review," *ACS Sustain. Chem. Eng.*, vol. 6, pp. 13611–13627, 2018, doi: 10.1021/acssuschemeng.8b03545.

[40] H. Wang and B. Friedrich, "Development of a Highly Efficient Hydrometallurgical Recycling Process for Automotive Li–Ion Batteries," *J. Sustain. Metall.*, vol. 1, no. 2, pp. 168–178, 2015, doi: 10.1007/s40831-015-0016-6.

[41] Y. Yang, G. Huang, M. Xie, S. Xu, and Y. He, "Synthesis and performance of spherical LiNi x Co y Mn 1-x-y O 2 regenerated from nickel and cobalt scraps," *Hydrometallurgy*, vol. 165, pp. 358–369, 2016, doi: 10.1016/j.hydromet.2015.11.015.

[42] V. Kothekar, "Basic UV-Vis Theory, Concepts and Applications Basic UV-Vis Theory, Concepts and Applications," *Protocol*, pp. 1–28, 2012.

[43] "Supermini200 overview." https://www.rigaku.com/en/products/xrf/supermini/overview.

[44] P. Brouwer, *Theory of XRF*. 2010.

[45] J. P. Peris S., "Selective Co-precipitation of Ni , Mn and Co from Spent Lithium-ion Batteries from Electric Vehicles (EVs)," no. December, 2019.

[46] Agilent Technologies, "Microwave Plasma Atomic Emission Spectroscopy (MP-AES) Application eHandbook," *eHandbook*, p. 166, 2016, [Online]. Available: https://www.agilent.com/en/products/mp-aes.

[47] A. Stoffel, "NTNU LIBRES Internship," 2019.

[48] J. Paulino and P. Sastre, "Leaching experiments of pre-treated Lithium-ion Battery Electrodes from Spent Electric Vehicles," 2020.

[49] J. Paulino and P. Sastre, “Lithium-Ion Batteries Recycling from EV ’ s (LIBRES),” 2019.

[50] Z. Ali, “Separation processes for recycling of metals from lithium-ion batteries (LIBs) of electric cars,” 2020.

[51] I. Berg, “Validation of MP-AES at the Quantification of Trace Metals in Heavy Matrices with Comparison of Performance to ICP-MS,” pp. 1–31, 2015, [Online]. Available: http://www.diva-portal.org/smash/get/diva2:853851/FULLTEXT01.pdf.

[52] R. Sattar, S. Ilyas, H. N. Bhatti, and A. Ghaffar, “Resource recovery of critically-rare metals by hydrometallurgical recycling of spent lithium ion batteries,” *Sep. Purif. Technol.*, vol. 209, no. September 2018, pp. 725–733, 2019, doi: 10.1016/j.seppur.2018.09.019.

[53] “Application Note XT5 Microwave Digestion of Molybdenum Oxide.”

[54] W. Lv, Z. Wang, H. Cao, Y. Sun, Y. Zhang, and Z. Sun, “A Critical Review and Analysis on the Recycling of Spent Lithium-Ion Batteries,” *ACS Sustain. Chem. Eng.*, vol. 6, no. 2, pp. 1504–1521, 2018, doi: 10.1021/acssuschemeng.7b03811.

[55] M. A. H. Shuva and A. S. W. Kurny, “Dissolution Kinetics of Cathode of Spent Lithium Ion Battery in Hydrochloric Acid Solutions,” *J. Inst. Eng. Ser. D*, vol. 94, no. 1, pp. 13–16, 2013, doi: 10.1007/s40033-013-0018-0.

[56] D. Coleman and V. Lynn, “Statistics in Analytical Chemistry: Part 48—Relative Standard Deviations (RSDs),” 2012. https://www.americanlaboratory.com/913-Technical-Articles/114240-Part-48-Relative-Standard-Deviations-RSDs/.

[57] A. Gustavo González and M. Ángeles Herrador, “A practical guide to analytical method validation, including measurement uncertainty and accuracy profiles,” *TrAC - Trends Anal. Chem.*, vol. 26, no. 3, pp. 227–238, 2007, doi: 10.1016/j.trac.2007.01.009.

[58] J. Kang, J. Sohn, H. Chang, G. Senanayake, and S. M. Shin, “Preparation of cobalt oxide from concentrated cathode material of spent lithium ion batteries by hydrometallurgical method,” *Adv. Powder Technol.*, vol. 21, no. 2, pp. 175–179, 2010, doi: 10.1016/j.apt.2009.10.015.

[59] A. Van Bomme and J. R. Dahn, “Analysis of the growth mechanism of coprecipitated spherical and dense nickel, manganese, and cobalt-containing hydroxides in the presence of aqueous ammonia,” *Chem. Mater.*, vol. 21, no. 8, pp. 1500–1503, 2009, doi: 10.1021/cm803144d.

[60] V. L. Manomenova, E. B. Rudneva, A. É. Voloshin, L. V. Soboleva, A. B. Vasil’ev, and B. V. McHedlishvili, “Growth of α-NiSO4 · 6H2O crystals at high rates,” *Crystallogr. Reports*, vol. 50, no. 5, pp. 877–882, 2005, doi: 10.1134/1.2049412.

[61] B. Han, R. Anwar, U. I. Haq, and M. Louhi-kultanen, “Hydrometallurgy Lithium carbonate precipitation by homogeneous and heterogeneous reactive crystallization,” *Hydrometallurgy*, vol. 195, no. October 2019, p. 105386, 2020, doi: 10.1016/j.hydromet.2020.105386.

Appendix

- Calculations for the mass needed to take from the $NiSO_4 \cdot 6H_2O$, $CoSO_4 \cdot 7H_2O$, and $MnSO_4 \cdot H_2O$ stock bottles to prepare synthetic solution of preliminary precipitation experiments.

$$m(NiSO_4) = 262.85\frac{g}{mol} \cdot 0.04\frac{mol}{L} \cdot 0.5L \cdot \frac{1}{0.98} = 5.3643g$$

$$m(CoSO_4) = 281.1\frac{g}{mol} \cdot 0.02\frac{mol}{L} \cdot 0.5L \cdot \frac{1}{0.99} = 2.8394g$$

$$m(MnSO_4) = 169.02\frac{g}{mol} \cdot 0.03\frac{mol}{L} \cdot 0.5L \cdot \frac{1}{0.99} = 2.5609g$$

- Calculation of the NaOH solution concentration that reacts with the metal sulphates and increases the pH to 12 adding 100 mL to 100 mL of synthetic solution (total final volume of 200 mL.

$$NaOH\left(\frac{mol}{L}\right) = 0.18\frac{mol}{L} + 0.01\frac{mol}{L} \cdot \frac{0.1L}{0.2L} = 0.185\frac{mol}{L}$$

- MP-AES external calibration curves.

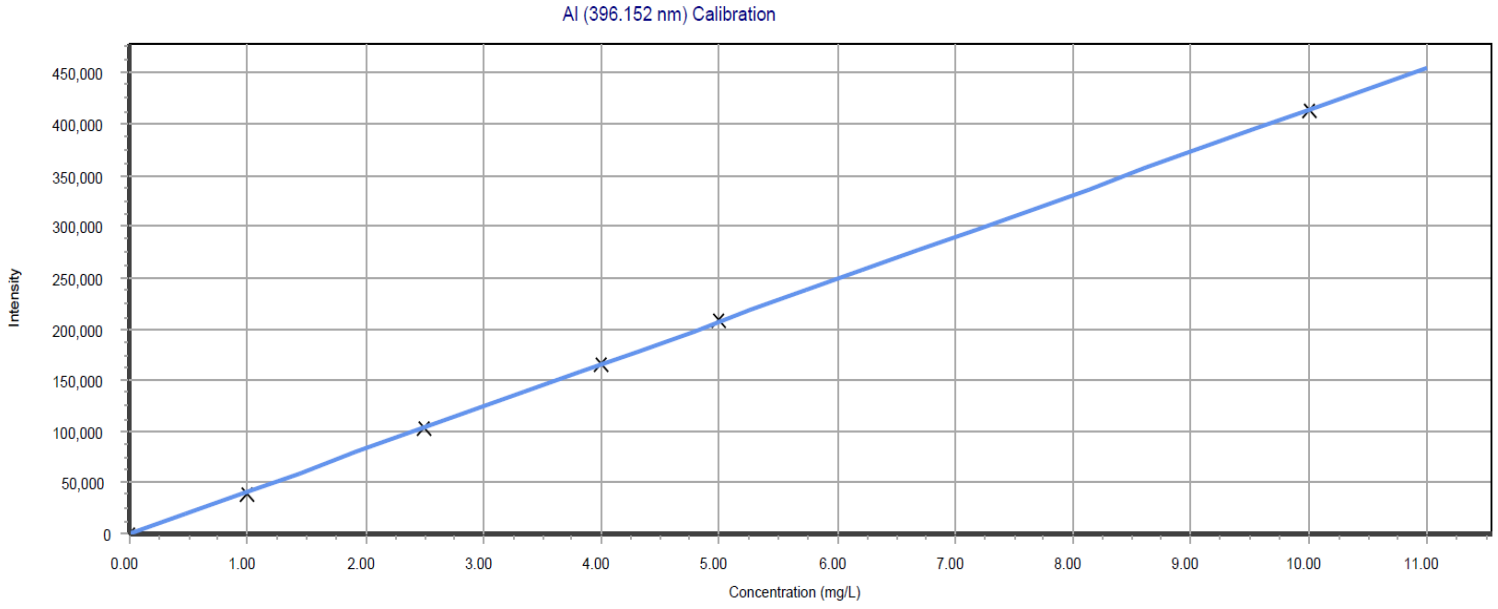

Intensity = 41401.62282795 * Concentration - 0.05177979

Correlation coefficient: 0.99996

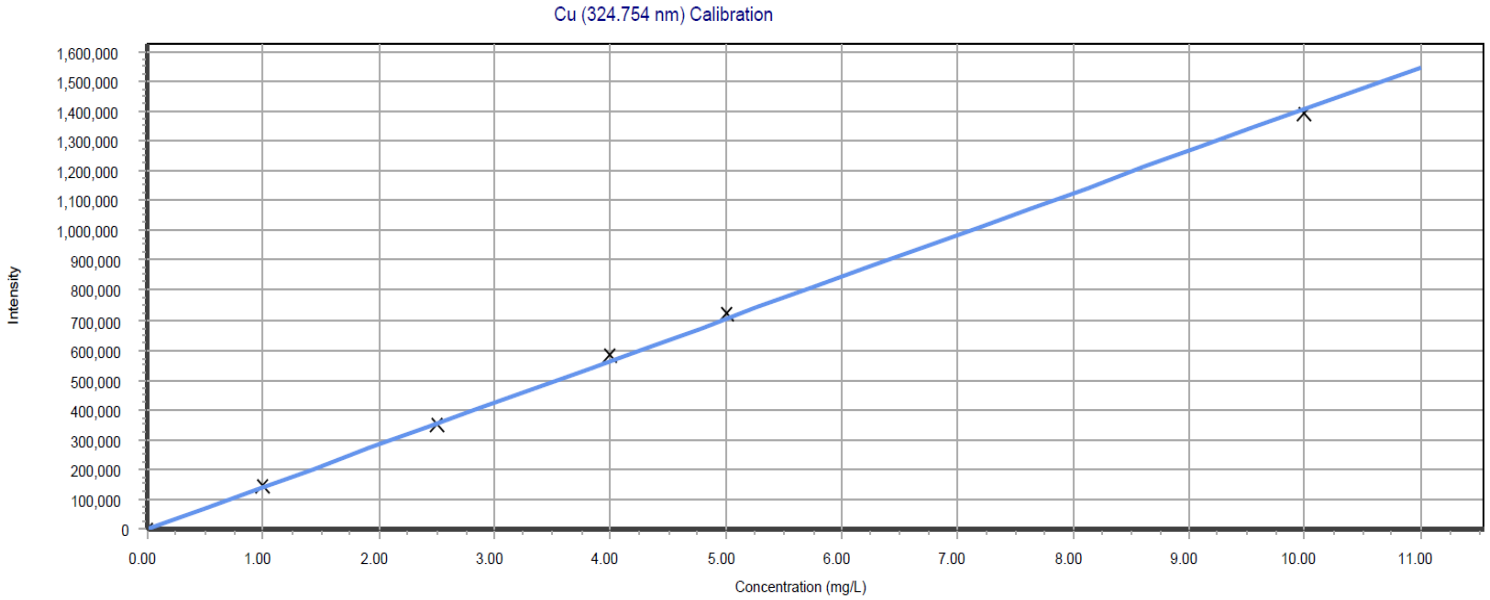

Intensity = 140778.87335860 * Concentration + 32.86501847

Correlation coefficient: 0.99965

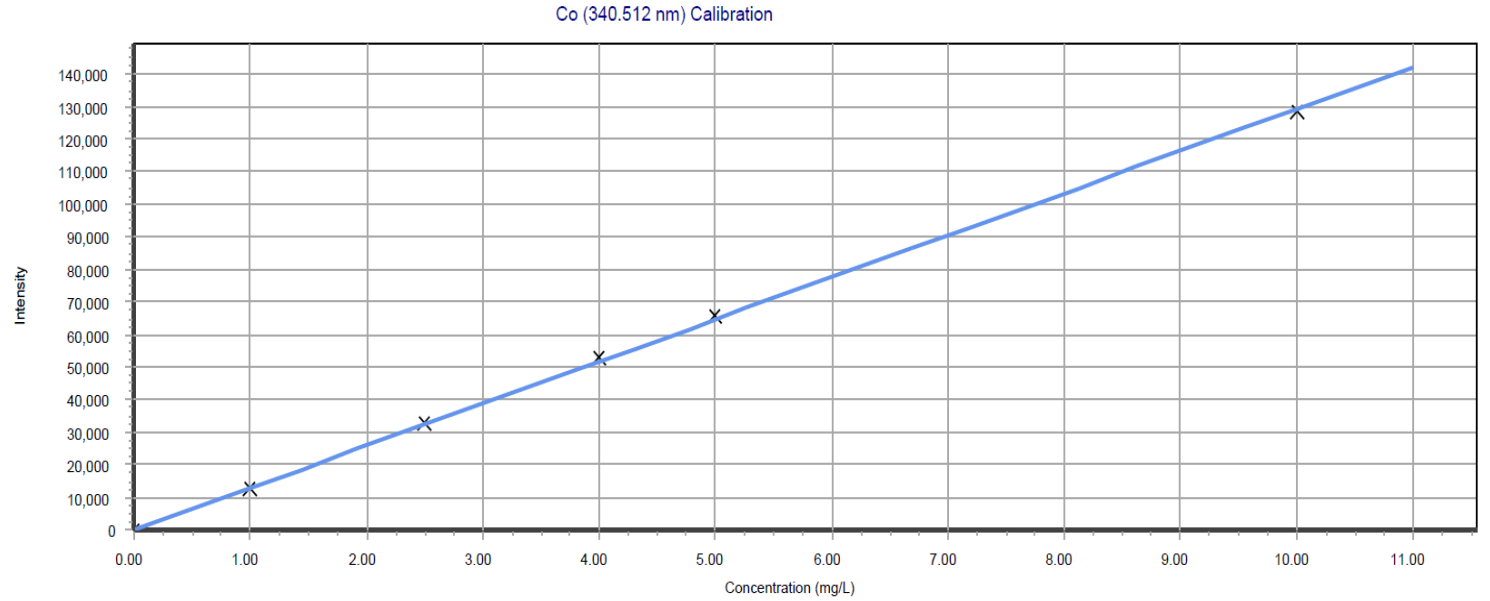

Intensity = 12926.95413700 * Concentration - 0.80707021

Correlation coefficient: 0.99985

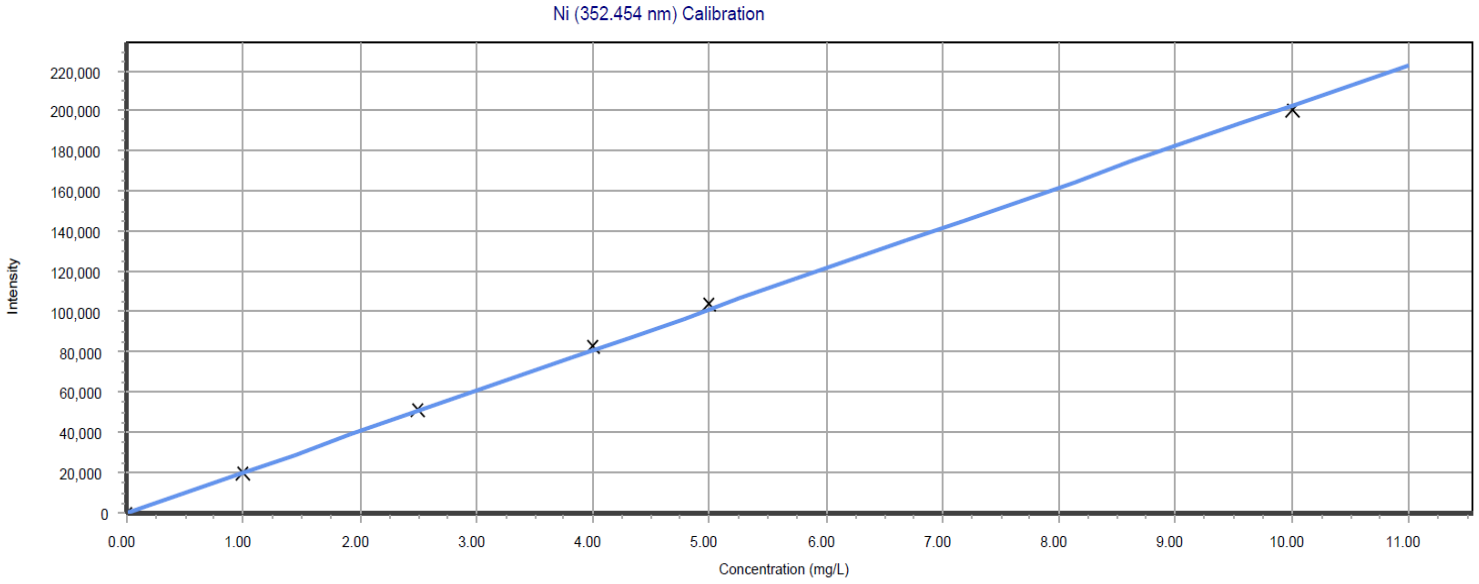

Intensity = 20247.18949933 * Concentration + 0.52028446

Correlation coefficient: 0.99971

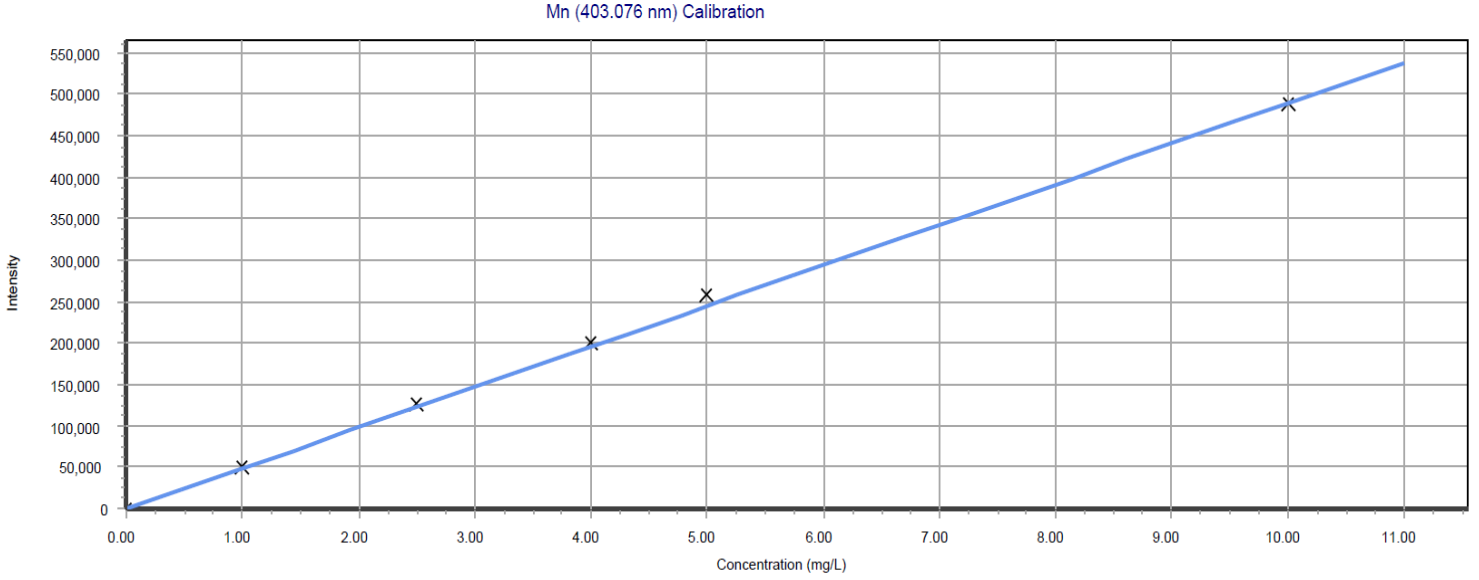

Intensity = 48959.31232977 * Concentration + 0.59361960

Correlation coefficient: 0.99959

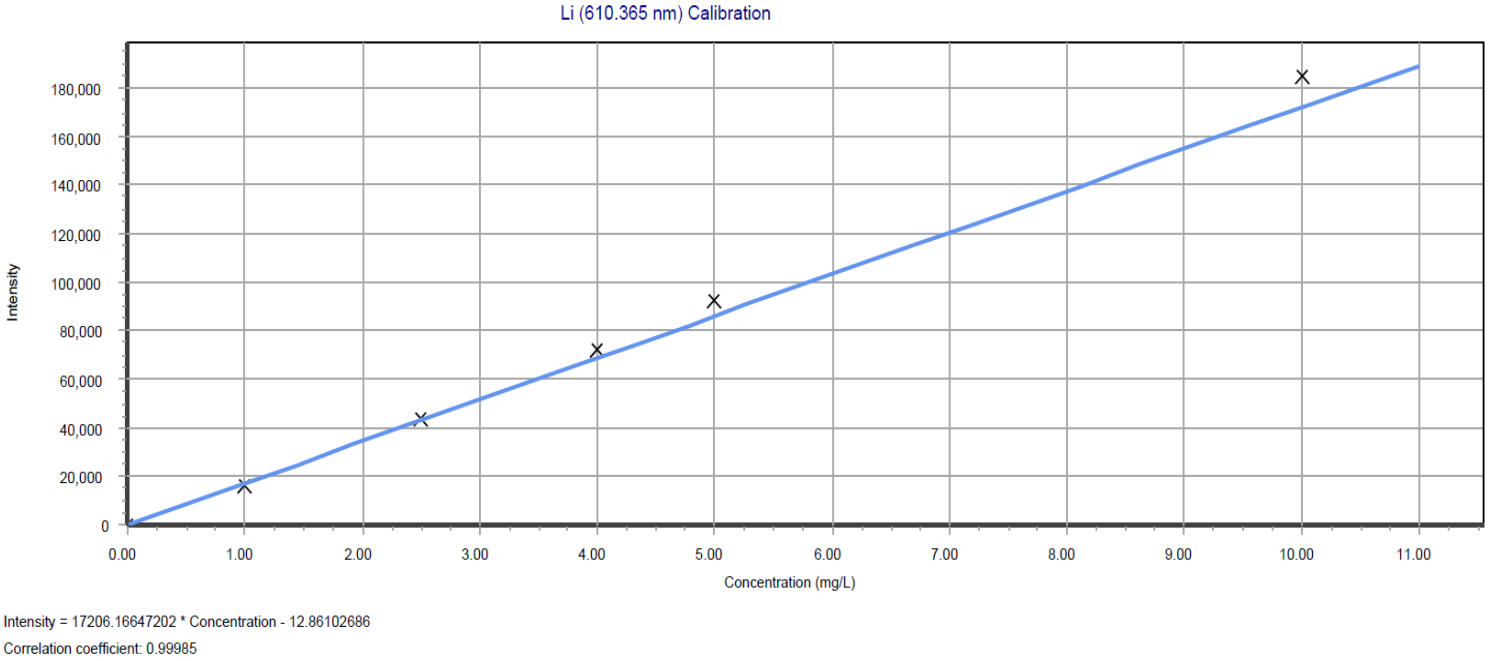

- Li concentration needed in the solution to start precipitating as Li_2CO_3.

$$7.8\frac{g(Li_2CO_3)}{L}\cdot\frac{1mole(Li_2CO_3)}{73.891g(Li_2CO_3)}\cdot\frac{2moles(Li)}{mole(Li_2CO_3)}\cdot\frac{6.941g(Li)}{1mole(Li)}=1.465\frac{g(Li)}{L}$$

- Reaction controlled fitted models for the leaching kinetics.

Reaction Controlled Pyrolyzed 3.75 vol% H_2O_2

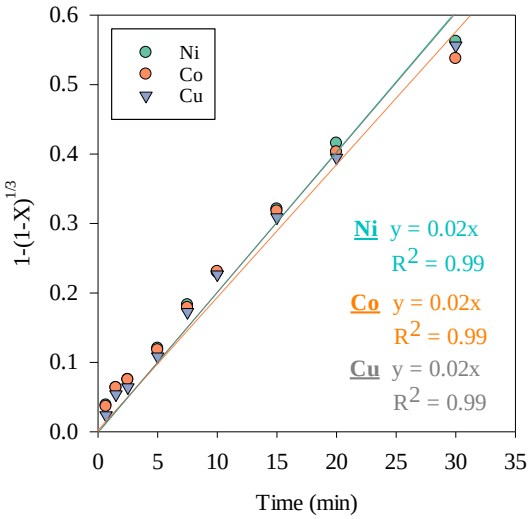

Reaction Controlled Non Pyrolyzed 7.5 vol% H_2O_2

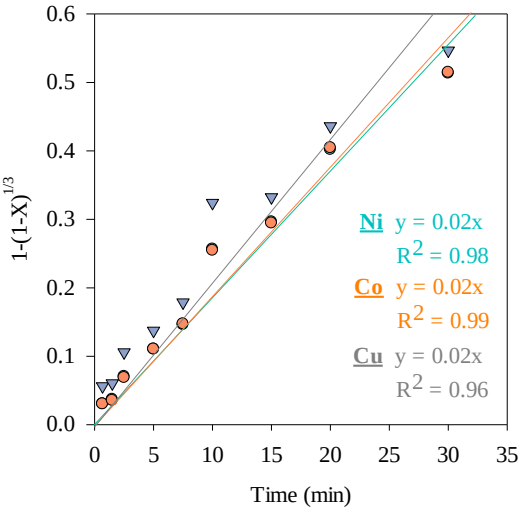

Reaction Controlled Leaf 3.75 vol% H_2O_2

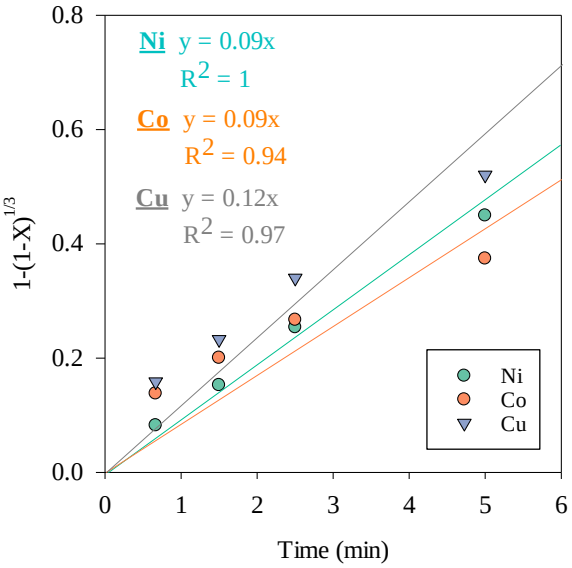

- Diffusion controlled fitted models for the leaching kinetics.

Diffusion Controlled Pyrolyzed 3.75 vol% H_2O_2

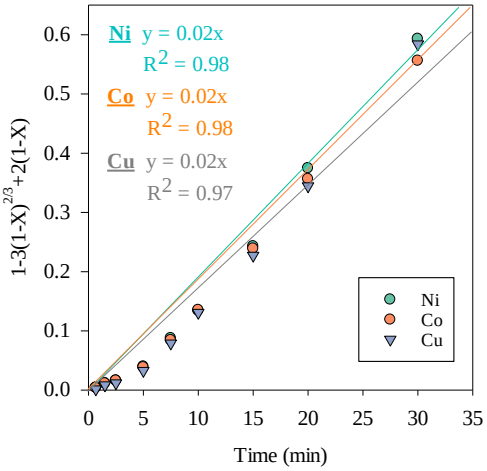

Diffusion Controlled Non Pyrolyzed 7.5 vol% H_2O_2

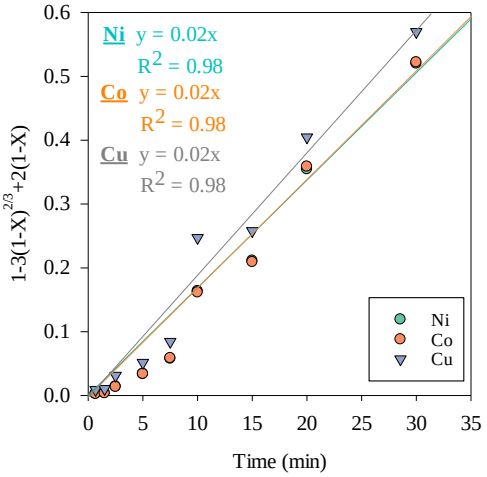

Diffusion Controlled Leaf 3.75 vol% H_2O_2

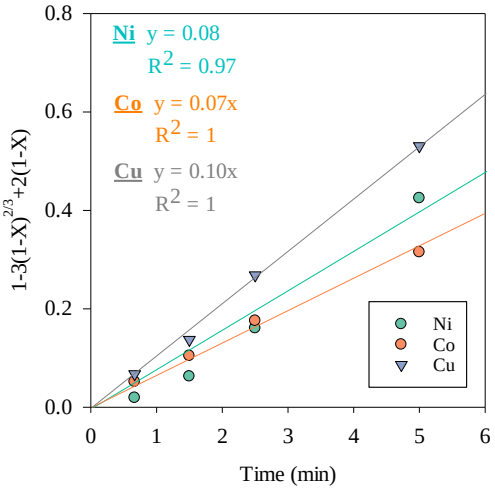

- Preliminary Synthetic Solution Precipitation.

The synthetic solution prepared had a concentration of 2.35 g Ni/L, 1.179 g Co/L, and 1.65 g Mn/L. The Ni: Co: Mn mass ratio was 0.45: 0.23: 0.32. The synthetic solution pH versus volume of NaOH (0.185 M) added is shown below. From the pH evolution against the volume of precipitant added it is possible to identify the different metal precipitation stages.

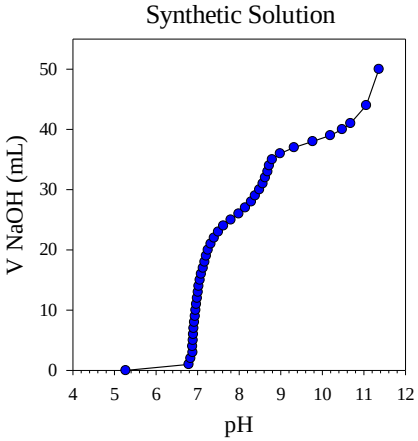

The parts where pH does not vary with increasing NaOH volume represent the reaction between the metal sulphates and the NaOH. Thus, the horizontal parts of the curve represent the precipitation of the metal hydroxide products as they get supersaturated with increasing pH values. Two precipitation stages are easily differentiated. The first one from pH 7 to pH ~ 8 which is the precipitation corresponding to $Ni(OH)_2$ and $Co(OH)_2$. Agreeing with [40], at pH 8, more than 90% of Co and Ni are precipitated while 59% of Mn is still in solution in a leaching solution of battery CAM scrap. The second precipitation stage corresponds to the Mn precipitation from pH 8 to pH ~ 9. On the other hand, the real leachates have another precipitation stage from pH 1 to 7 representing the precipitation of the impurities Al and Cu.

First, the pH of the solution was increased to 11.5 by adding NaOH, at this pH all metals may have precipitated in the form of hydroxides [40]. Composition from XRF is shown below. Precipitation was performed 3 times from 100 mL solutions so that results are shown as Average ± SD. Hence, standard deviations shown below come from the three different precipitates with different total mass, and mass%.

	Mass %	**Mass (g)**	**Normalized mass %**	**Normalized mass % initial solution**

Na	12.5 ± 5.7			
Al	0.1 ± 0.2			
Si	1.9 ± 0.5			
S	1.9 ± 0.1			
K	0.6 ± 0.5			
Mn	26.3 ± 1.9	0.5 ± 0.0	31.7 ± 0.0	31.9
Co	17.9 ± 0.5	0.4 ± 0.0	21.5 ± 0.0	22.8
Ni	38.8 ± 3.0	0.8 ± 0.0	46.8 ± 0.0	45.4

The metal mass was calculated from the total mass of the precipitate, which for the three precipitations performed at pH of 11.5 were 2.1084 g, 1.8874 g, and 1.9748 g. The normalized mass% in precipitates and initial solution refers to the ratios between the three metals of interest. The Ni, Co and Mn masses shown above were higher than the actual metal masses present in the initial solution of 100 mL (0.2348 g of Ni, 0.1179 g of Co, and 0.1648 g of Mn). This is due to the fact explained in section 4.2.2 that is not possible to measure elements with lower atomic number than oxygen, including oxygen, with XRF. Unless the elements measured in XRF are in form of oxides and they are measured and calculated in this way, oxygen it is not analysed. Therefore, the precipitates shown in the table above, are the metal composition normalized values. The total mass% adds up to 100% although it does not account for oxygen and hydrogen, and the precipitates are in form of hydroxides. This means that the mass% values for the metals are higher than the real value. Nevertheless, the relative values or ratios between the elements is reliable. This was proved comparing the normalized mass% of Ni, Co, and Mn in the precipitates at pH 11.5 where all three metals have precipitated in the initial solution. The values are very close to each other, with a difference of 1.4% for Ni, 1.2% for Co, and 0.2% for Mn. Consequently, if these Ni, Co, and Mn masses in the precipitates at pH of 11.5 were initially present in a 100 mL solution, the % of metal precipitated can be calculated comparing the mass in the precipitate at different pH values with these at pH 11.5.

In order to reach the goal of selectively precipitate more Ni over Co and Mn, the pH value of 7.7 was chosen to analyse the precipitates [40]. The composition from XRF and metal (%) precipitated are shown below.

	Mass %	Mass (g)	Normalized mass %	% Precipitated
Na	2.0 ± 0.1			
Al	0.1 ± 0.0			
Si	0.2 ± 0.1			
S	7.6 ± 0.1			
K	0.1 ± 0.0			
Mn	22.4 ± 0.2	0.3 ± 0.0	24.9 ± 0.0	65.3 ± 0.0
Co	14.3 ± 0.1	0.2 ± 0.0	15.9 ± 0.0	61.3 ± 0.0
Ni	53.2 ± 0.1	0.8 ± 0.0	59.2 ± 0.0	104.8 ± 0.0

The total precipitate mass at pH of 7.7 was 1.5344 g, 1.4847 g, and 1.5444 g for the three precipitations carried out. From the table, it can be seen that % Ni precipitated is slightly higher than 100%, but this could be due to experimental errors in weighting the total precipitate mass, precipitates not completely homogeneously mixed when taking the sample to analyse, etc. In conclusion, it was proved that at pH 7.7 all Ni was precipitated while 34.8 and 38.8% of Mn and Co, respectively, were still present in the solution. Hence, pH of 7.7 was chosen for the following precipitation experiments with the real leachates from spent battery CAM.

- Excel sheet with precipitation (%) calculations.

https://studntnu-my.sharepoint.com/:x:/r/personal/josepp_ntnu_no/Documents/Data%20copies%20for%20me/MP-AES%20Calculation.xlsx?d=w754d001cadba41578368a8e2f943ac03&csf=1&web=1&e=PM6lCH